Chapter 5

Raman-Silent Magnesium Fluoride Nanomembrane Use in Raman-Compatible Cell Culture

5.1 Abstract

Raman spectroscopy provides a method to noninvasively assess the chemical composition of materials, quantitatively. Utilizing this method to track cellular processes *in vitro* has gained popularity in recent years. However, current methods in use where cells are grown on non-permeable supports create a key limitation that prevents cells from adopting healthy morphologies. Furthermore, permeable materials that are commonly used in cell culture are not appropriate for Raman spectroscopy because of material compositions that limit the amount of power used for measurement, relatively large membrane volumes that scatter light, and large background signals that decrease the efficiency of measurement. Here, we develop permeable materials that support epithelial cell culture while enabling Ra-

man microspectroscopy. Thin films of magnesium fluoride (MgF_2, 50-200 nm thick) were evaporated onto silicon nitride nanomembrane templates (50-200 nm thick) of varying pore sizes (50-400 nm pore diameters) and then released from the template using a reactive ion etch process, with yields up to 50% for 0.5 mm microporous square windows. The resulting freestanding films have pore sizes similar to the initial templates and support cell culture over a suitably long period (4 weeks). Raman measurements of cells deposited on the nanomembranes are able to localize RNA to the cytoplasm. ARPE-19 cells grown over a period of four weeks on the fabricated substrates express a mosaic of a tight junction protein (ZO-1), indicative of a polarized cell monolayer.

5.2 Introduction

There is a growing interest in Raman spectroscopy as a non-invasive, label-free method to detect different substances in cells. Raman microspectroscopy enables the study of cellular transport and composition by illuminating direct, spatially resolved, quantitative concentrations of biomolecules. Example applications include liposome nanoparticle uptake [124], nutrient flow within a cell [125], discrimination between cardiomyocyte phenotypes [126], and subcellular localization of nucleic acids [127]. Common cell culture work is performed on plastic, glass, or silicon materials due to the ease of manufacture and low cost, but these substrates have a large

Raman signature (Si = 520 cm^{-1}) that can dwarf biomolecular signatures [128]. Therefore, Raman studies involving living cells are typically performed with magnesium fluoride (MgF_2), quartz, or calcium fluoride substrates that have very low background signatures in the biological fingerprint region (BFR) between 600 and 1800 cm^{-1} [127]. Substrate permeability is necessary for some cell phenotypes as epithelial cells are known to polarize on permeable, but not impermeable substrates [129, 130]. Introducing permeability to a Raman compatible substrate would permit the study of barrier tissue models in vitro that are better mimics of in vivo barriers.

An ideal Raman substrate for this situation would be: 1) highly permeable, allowing unhindered exchange of small molecules between cells and a basolateral compartment, 2) Raman transparent over the BFR, and 3) support cell adhesion and viability over extended periods (weeks) needed for epithelial monolayers to mature. Thick (1-10 μm) polyester and polycarbonate track-etched materials that are commonly used for epithelial cell culture are impossible to use for Raman imaging. These carbon-rich materials strongly scatter light, fluoresce, and produce confounding Raman signals that will mask biological fingerprints. More recently developed silicon (pnc-Si, [2]) and silicon nitride nanomembranes (NPN, [22]) have the requisite permeability (50 nm thick, >15% porosity) and biocompatibility [4]. Unfortunately, silicon has a strong first-order Raman signal at 520 cm^{-1}, as does annealed silicon nitride between 750 and 1100 cm^{-1} [131], which

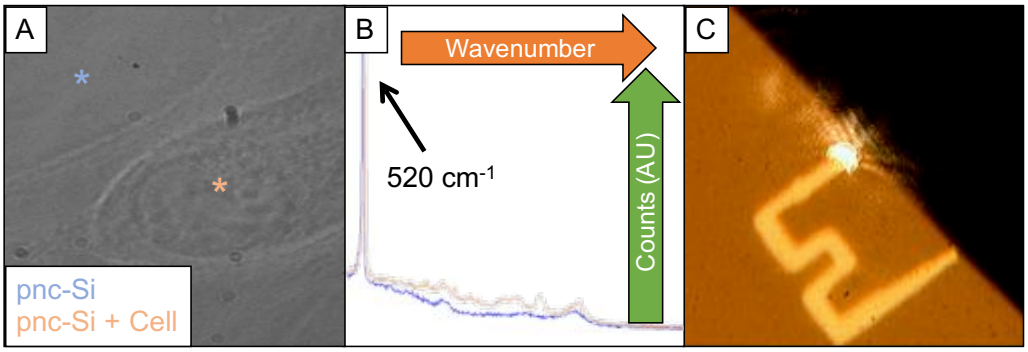

Figure 5.1: pnc-Si Unsuitable for Raman Measurements. (A) Cell deposited on pnc-Si nanomembrane. (B) The silicon signal from the pnc-Si substrate (blue, 520 cm^{-1}) overwhelms the Raman signature of a cell on the nanomembrane (orange). (C) 30 mW of laser power is sufficient to melt the pnc-Si nanomembrane.

overlaps with several peaks associated with proteins, DNA, nucleic acids, and lipids [132]. Figure 5.1 demonstrates an example of this behavior on a pnc-Si nanomembrane. The large background peak of silicon is evident, especially in comparison to the minimal Raman signatures produced by a cell grown on the nanomembrane. Even small amounts of laser power can also melt the pure silicon nanomembrane *in situ*, fundamentally limiting the measurement rate. By contrast, the Raman background signature of MgF_2 is negligible in the BFR [133], accounting for the use of MgF_2 coverslips in Raman-compatible cell culture. Thus, the goal of our effort was to create a MgF_2 membrane with an ultrathin, porous structure and then to demonstrate the application of this novel material to Raman imaging of cultured epithelial cells.

5.3 Fabrication

Given that the only unfavorable characteristics of silicon nanomembranes as a cell substrate is that the materials are not Raman compatible and readily absorb laser power (Figure 5.1), we developed a template strategy that allowed us to substitute MgF_2 for silicon-rich silicon nitride, NPN. We began by evaporating 50 nm of MgF_2 (200 $^\circ$C, 0.1-0.3 $\frac{nm}{sec}$, platen rotation on) on the front side of NPN chips (SiMPore Inc., West Henrietta, NY) (Figure 5.2a). The deposition partially infills the NPN template without occluding the pores as a result of the line-of-sight evaporation process (Figure 5.2b, 5.2f). The hybrid membrane was then thermally annealed at 600 $^\circ$C for 2 hours, to stabilize and strengthen the thin film. Finally, the NPN template is removed by applying a reactive ion etch (90% CHF_3, 10% Oxygen, 75 mTorr, 100 W, $\sim$1 $\frac{nm}{sec}$ etch rate) for 55 seconds (Figure 5.2c) to the backside of the annealed chips, creating nanoporous MgF_2 (npMgF_2). This etch recipe was chosen from observations of etch selectivity between evaporated MgF_2 films and silicon nitride. By iterating power, pressure, and gas ratios of the etch recipe, we found that faster etch rates resulted in lower yielding lots, and that a high (>5%) oxygen flow was necessary to minimize fluorocarbon formation [134]. SEM inspection of membrane cross-sections confirm that MgF_2 nanomembranes are $\sim$50 nm thick (Figure 1d) while STEM images clearly show open pores (Figure 5.2e). A custom pore analysis software was used to determine pore histograms [10]

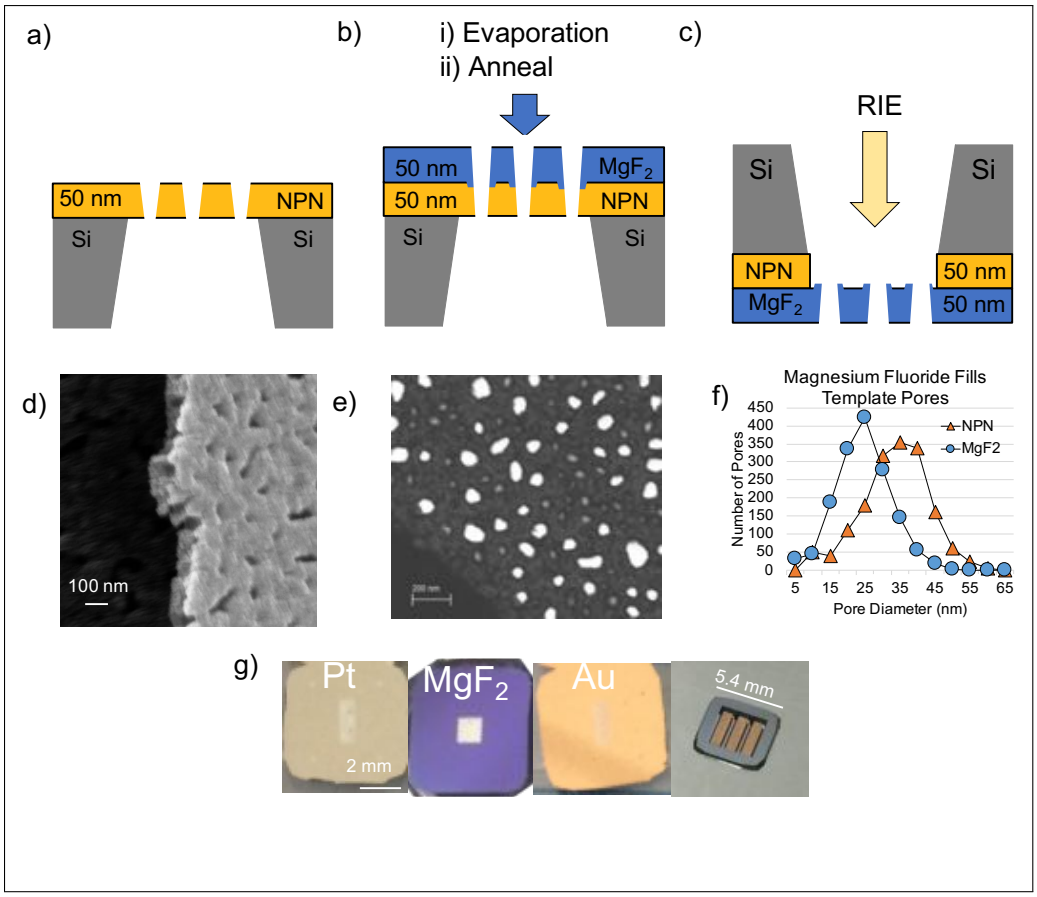

Figure 5.2: Annealed npMgF$_2$ Nanomembrane Fabrication. npMgF$_2$ nanomembrane material properties. (a)-(c) npMgF$_2$ relief pattern transfer, with cartoon cross-sections of nanoporous films (not to scale). Beginning with a freestanding film of NPN (a), MgF$_2$ is evaporated onto the substrate (50 nm, 0.1-0.3 $\frac{nm}{sec}$, 25 °C, Platen Rotation), coating the porous substrate, resulting in a hybrid material (b). After an annealing process (600 °C, 2 hrs, Ar ambient), the substrate is then inverted and purified using RIE (90% CHF_3, 10% O_2, 75 mTorr, 100 W), (c) releasing a freestanding nanoporous film of MgF$_2$. (d) SEM cross-section of a fabricated MgF$_2$ nanomembrane (50 nm thick, coated with Au). (e) STEM image displaying open nanopores (white) in a MgF$_2$ nanomembrane. (f) Pore histogram generated from representative SEM images, displaying that a MgF$_2$ nanomembrane will have reduced pore sizes compared to the template. (g) Example 5.4 mm square chips fabricated using this strategy with freestanding 50 nm thick Pt (sputtered, no anneal), Au (sputtered, no anneal), and npMgF$_2$ nanomembranes. At right is an inverted Au chip post RIE, with three 3 x 0.7 mm, 50 nm thick freestanding gold nanomembranes exposed

Table 5.1: $npMgF_2$ Process Yield. Free-standing 50 nm $npMgF_2$ membranes were manufactured as described in Figure 5.2. The 200 μm window size was produced under a different evaporation temperature (250 °C) and was not annealed

Window Size (μm)	Starting Number of Chips	Remaining after Evaporation	Remaining after Anneal	Remaining after Etch	Overall Process Yield (%)
100	65	62	62	60	92 %
200	10	10	N/A	2	20 %
300	65	62	57	22	34 %
500	65	41	26	1	2 %
700	65	58	49	0	0 %
900	65	38	29	15	23 %
1100	65	27	23	3	5 %

from STEM images which were then compared to the original NPN template. The histograms indicate a reduction in pore diameters by about 10 nm (Figure 5.2f). A slight narrowing of the distribution and a slight reduction in the porosity likely follows from the loss of the smallest pores (< 10 nm) in the NPN template due to total occlusion during the MgF_2 deposition. The relief process demonstrated here can be also extended to other deposited thin films (Figure 5.2g), such as gold and platinum, limited by the mechanical strength of the deposited film, thin film stresses, and a modest selectivity to the reactive ion etch. Utilizing other direct deposition techniques, such as sputtering, may change the process by requiring different environmental factors to get a stable thin film. Extending the process to other materials may require different RIE chemistries depending on their reaction to CHF_3/ O_2.

Overall yield was strongly dependent on the membrane window size

(Table 5.1) with 100 μm square windows resulting in yields > 95% while larger area membranes have yields < 20%. The greatest losses occur during the etch process (Table 5.1), suggesting that scaffolding [18, 135] should be explored to improve process yield over larger windows. Another way to improve yield would be to make the MgF_2 nanomembranes thicker, however thicker films would require larger diameter pore templates, to prevent total pore occlusion during MgF_2 deposition. While small active areas (0.01-0.05 mm^2) can be sufficient for many applications, cell culture may require larger areas for inspection to visualize hundreds of cells, as well as providing enough area for sufficient basolateral nutrition.

To that end, we used a similar process to create thicker MgF_2 nanomembranes in an effort to make the fabricated nanomembranes stronger and improve the yield of the process. In these studies, we evaporated 200 nm of MgF_2 (200°C, 0.3-0.5 $\frac{nm}{sec}$, platen rotation, Figure 5.3) onto the flat-side of microporous silicon nitride membranes (500 nm pores, SiN, 120 nm thick, SiMPore Inc., West Henrietta, NY). The microporous SiN membranes had 2 variants: high porosity (1:1 pore spacing) and low porosity (1:3 pore spacing). These hybrid membranes were then released using a RIE with same etch chemistry (90% CHF_3, 10% Oxygen, 75 mTorr, 100 W, $\sim$1 $\frac{nm}{sec}$ etch rate), for a longer time (140 seconds) to compensate for the thicker template. SEM inspection of the fabricated membrane cross-sections confirm that microporous MgF_2 (μpMgF_2) nanomembranes are $\sim$200 nm thick (Figure 5.3d), while TEM confirms that the micropores are

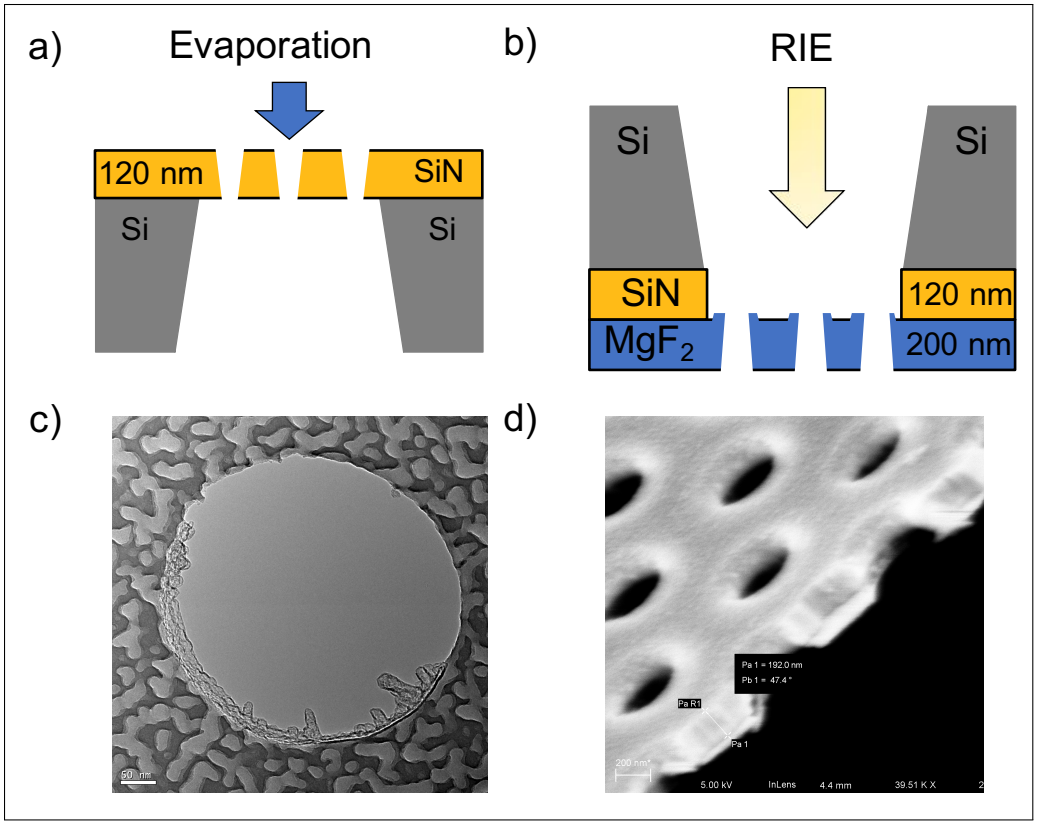

Figure 5.3: μpMgF$_2$ Nanomembrane Fabrication. (a) 200 nm thick MgF$_2$ coating is evaporated onto a SiN substrate containing 400 nm wide micropores. (b) The composite film stack is inverted, and then the SiN template is removed using a reactive ion etch process. (c) TEM image of the free-standing μpMgF$_2$ nanomembrane shows that the pore size largely is preserved, with a few "fingers" of MgF$_2$ infilling the edge of pore. The heat of the electron beam fuses MgF$_2$ grains together, leading to a textured pattern. (d) SEM cross-sectional image of a thinned substrate, 192 nm MgF$_2$ on top of 20 nm SiN.

open (Figure 5.3c. The thicker MgF_2 microporous membranes also experience pore narrowing from infilling, where residual ”fingers” remain due to the high selectivity of MgF_2 to the etch chemistry. The yields of the thicker microporous membranes were significantly improved compared to the thinner nanoporous membranes, doubling the number of chips that survived the process (Table 5.2). The higher porosity μpMgF_2 did show larger yield than the npMgF_2, but had lower yields than the low porosity MgF_2 chips (Figure 5.4). This could be due to the larger number of pores around the windows of the nanomembrane, which could provide mechanical defect sites for the membrane to rupture.

5.3.1 Material Characterization

We used Auger electron spectroscopy (AES), energy dispersive x-ray spectroscopy (EDX), and x-ray photoelectron spectroscopy (XPS) measurements to examine the elemental composition of membranes and confirm the effectiveness of the etch process. EDX (EDAX on Zeiss Auriga, University of Rochester) and XPS (Kratos Axis Ultra, University of Rochester) of npMgF_2 thin films were performed, and EDX of μpMgF_2 thin films were carried out using a Phi 710 scanning Auger nanoprobe under ultrahigh vacuum conditions in the Imaging and Chemical Analysis Lab at Montana State University. Acquisitions were performed with a 10 keV primary electron beam and a current of 0.2 nA for an 8 nm spot size. Spectra were averaged

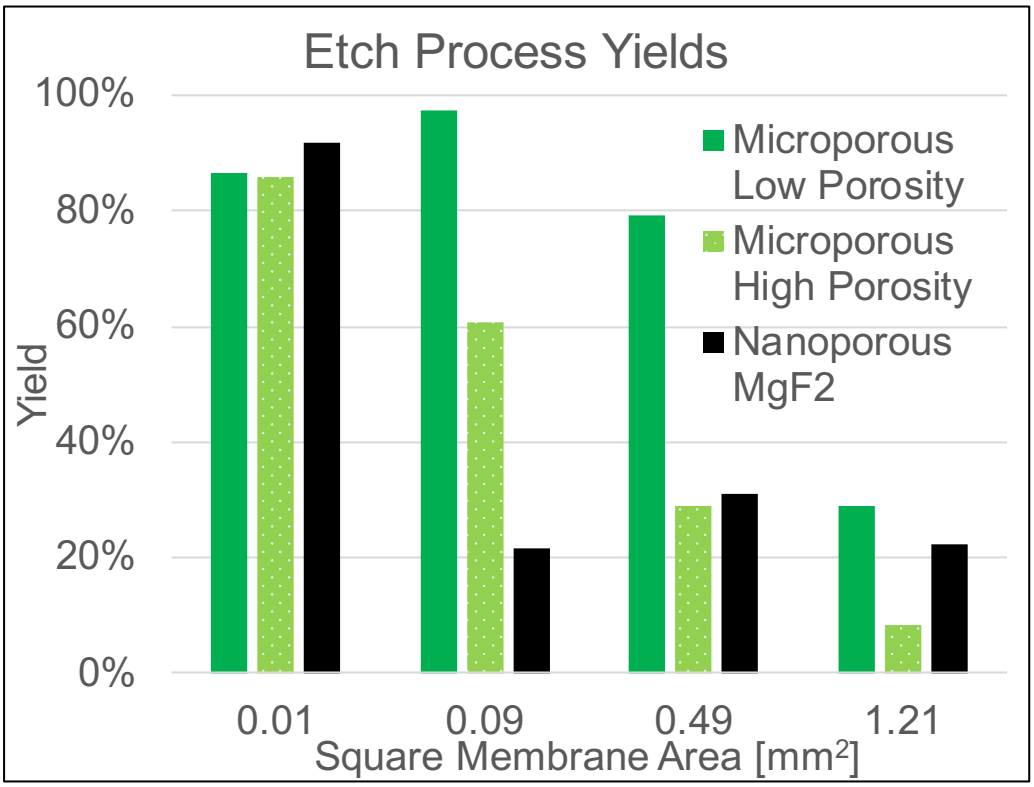

Figure 5.4: μpMgF_2 Yield Comparison. The patterned membranes with higher porosity (1:1 pore spacing) had worse yield than the membranes with lower porosity (1:3 pore spacing) at larger window sizes.

Table 5.2: μpMgF_2 Yield Statistics

Window [mm]	**Low Porosity Chips Start [#]**	**Low Porosity Chips after Evap. [#]**	**Low Porosity Chips after Etch [#]**	**Low Porosity Yield After Evaporation**	**Low Porosity Yield After Etch**	**Low Porosity Etch Process Yield**
0.1	30	30	26	100%	87%	87%
0.3	39	39	38	100%	97%	97%
0.5	30	29	24	97%	80%	83%
0.7	32	29	23	91%	72%	79%
0.9	31	9	3	29%	10%	33%
1.1	36	31	9	86%	25%	29%
Overall	198	167	123	84%	62%	74%
Window [mm]	**High Porosity Chips Start [#]**	**High Porosity Chips after Evap. [#]**	**High Porosity Chips after Etch [#]**	**High Porosity Yield After Evaporation**	**High Porosity Yield After Etch**	**High Porosity Etch Process Yield**
0.1	35	35	30	100%	86%	86%
0.3	28	28	17	100%	61%	61%
0.5	36	35	17	97%	47%	49%
0.7	34	31	9	91%	26%	29%
0.9	34	31	2	91%	6%	6%
1.1	28	24	2	86%	7%	8%
Overall	195	184	77	94%	39%	42%
	Total Chips	**Chips Left after Evap.**	**Chips Left after Etch**	**Yield after Evaporation**	**Yield after Etch**	**Etch Process Yield**
Total Sum	393	351	200	89%	51%	57%

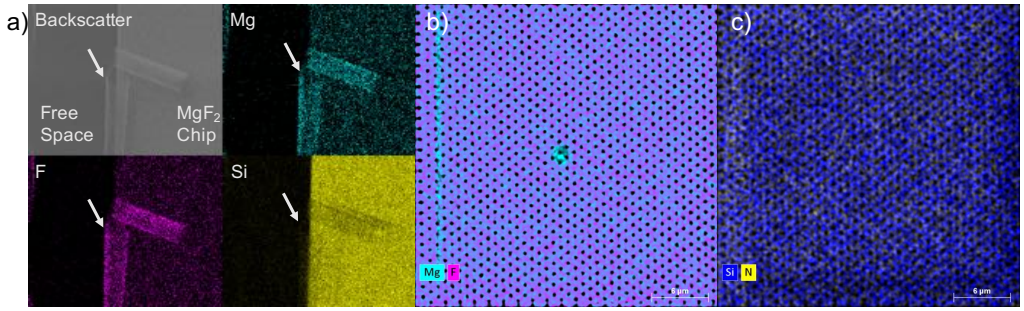

Figure 5.5: MgF$_2$ Nanomembrane Material Properties. (a) EDX map of a broken, curled npMgF$_2$ membrane is rich in magnesium and fluorine but not silicon. White arrows indicate the region over free space, away from the substrate chip. The entire membrane stack is over 85% pure. (b) EDX map of a μpMgF$_2$ membrane. The evaporated layer of MgF$_2$ is very pure, however, a thin SiN skin (c) remains underneath the material. (b, c) The author acknowledges the Imaging and Chemical Analysis lab at Montana State University for the use of their Auger nanoprobe tool.

over 30 cycles for an energy range of 0-2000 eV with a 0.1 eV step size. Maps were merged using the included Multipak software. When we found the ultrathin free-standing npMgF$_2$ membranes produced low EDX signals due to the tiny amount of material volume, we created folded remnants of the membrane by intentionally fracturing the substrate to produce a more robust signal. The presence of Mg and F elemental signatures, along with the absence of Si in one remnant, are apparent from the EDX images of MgF$_2$ curls shown in Figure 5.5a. Analysis of the small segment of remnant that protrudes into free space reveals that that composition of the free material is 85% MgF$_2$, however, XPS measurements that analyze only a thin section on the surface of the evaporated film show that the evaporated film lacks silicon nitride (Figure 5.6), indicating that some residual silicon nitride of the template remains. Similarly, μpMgF$_2$ membranes showed strong Mg

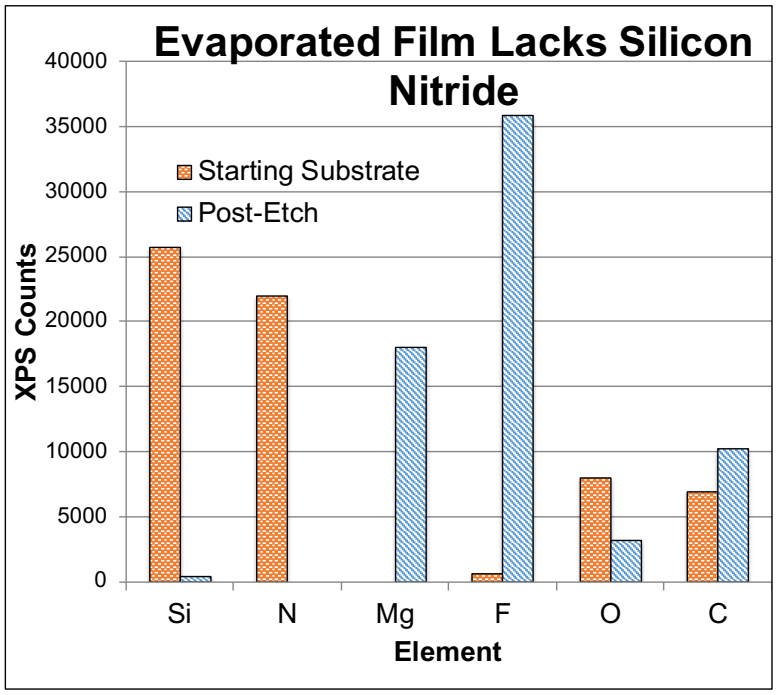

Figure 5.6: $npMgF_2$ XPS Composition. The starting substrate (NPN) is composed of a silicon-rich silicon nitride, and the evaporated film (after post-etch release) is composed of mainly magnesium and fluorine.

and F elemental maps (Figure 5.5b), however there was a thin SiN layer underneath the membrane (Figure 5.5c). Previous imaging bounds the thickness of this layer at less than 5 nm. For a 200 nm thick freestanding $npMgF_2$ membrane, this would comprise a 2.5% SiN impurity.

To better understand the structural component of these fabricated thin films, the microporous and nanoporous MgF_2 were imaged under TEM (Chapter 4). Figure 5.8 shows some structural differences between the microporous and nanoporous thin films. As the nanoporous film is only 50 nm thick, it is more transmissive and it is easier to observe finer details of

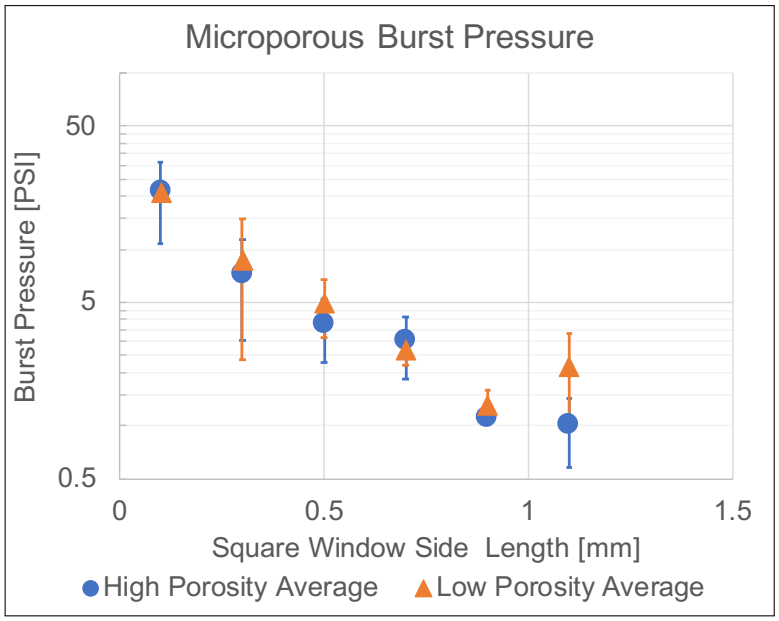

Figure 5.7: Mechanical μpMgF$_2$ Nanomembrane Strength as a Function of Porosity. Strengths are not significantly different from each other. Error bars are 1 standard deviation.

the MgF$_2$ grains that comprise the membrane. The nanoporous template pattern is familiar, but changed slightly as thicker edges of MgF$_2$ surround the nanopore due to MgF$_2$ coating the NPN's inner pore sidewalls during the evaporation process. The μpMgF$_2$ film is much thicker, and many grains align into a banded pattern. Here, infilling appears as "fingers" of MgF$_2$ coating the thicker template sidewalls (120 nm vs 50 nm). These structures aren't completely contiguous, and thus some have broken off during processing. The effects of residual silicon nitride are obvious as the additional thickness causes a loss of transmission in the image, blurring out the details of MgF$_2$ grains. A crack in the residual NPN template also

suggests that the MgF_2 is not strongly bound to the underlying template, as swathes of the membrane are without defect. The flakes of NPN at thin layers thus might fracture and separate from the MgF_2 as the template is etched away, creating a non-uniform free-standing release mechanism.

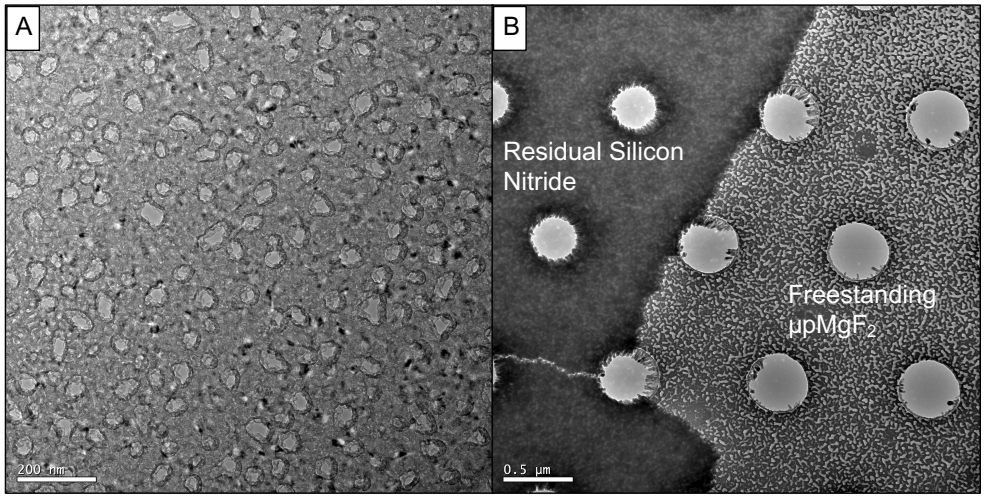

Figure 5.8: Thin-Film MgF_2 TEM Structure. (A) npMgF_2 displays open pores and some infilled structures reducing the effective pore size. (B) μpMgF_2 with some residual SiN template remaining. The central region of the membrane clears first during the RIE. A crack in the underlying template is observed.

Figure 5.9 shows a primary defect mode in μpMgF_2 nanomembrane structure. As many areas of the μpMgF_2 are intact, sometimes cracks form along edges or between pores. This is probably the reason that larger window sizes have lower yields (Table 5.2, as an increased chance to form a critical defect. One hypothesized reason for the cracking is that the MgF_2 film absorbs residual water vapor from it's environment which increases it's film stress [136]. These cracks are very small, only 5-10 nm across, which

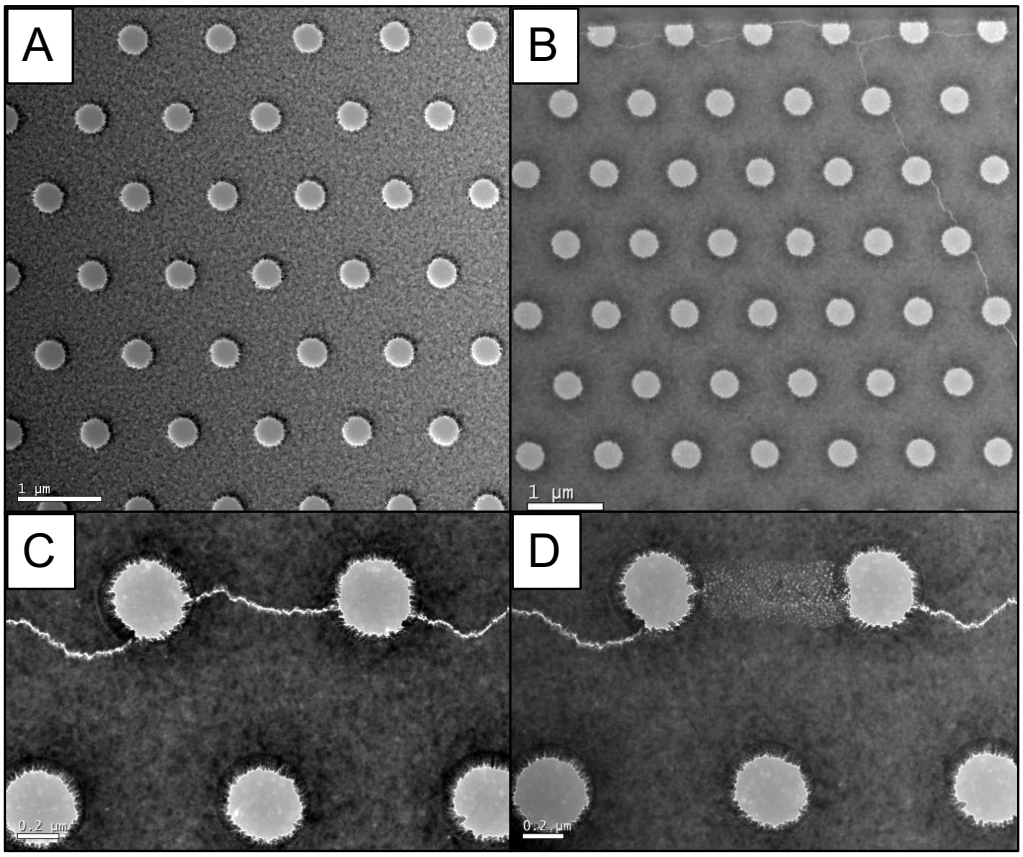

Figure 5.9: Defect in μpMgF$_2$ TEM Structure. (A) Many large pieces of μpMgF$_2$ appear intact over the scale of 10 μm. (B) Cracks are a primary defect mode in μpMgF$_2$, aligned with the membrane edges, as well as traversing from pore to pore, akin to weakness in corrugated paper. (C) Magnified view of a crack between two pores. (D) The heat of the TEM beam is enough to cause the thin film to fuse, eliminating the crack.

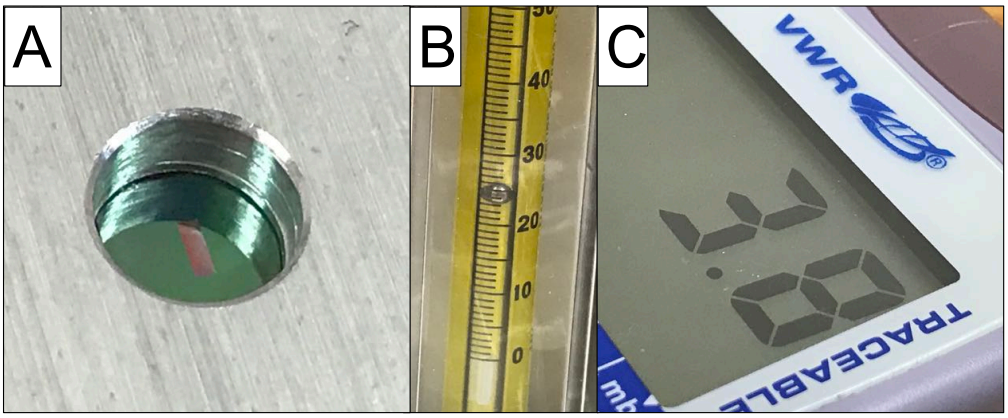

Figure 5.10: Burst Pressure Setup. (A) A chip is sealed into an aluminum jig using a face plate and o-ring. Membranes distend as nitrogen flows are applied to the chip, indicating a good seal. (B) Flow rates are measured using a rotometer and (C) pressures are recorded using a digital manometer.

make them a candidate for a reflow/thermal anneal process. In Figure 5.9d, the intensity of the TEM beam is enough to cause reflow in the MgF_2 layer, which suggests there is opportunity for such a process improvement.

To evaluate the strength of the fabricated nanomembranes, chips were sealed into a custom aluminum jig and then destroyed using increasing flows of nitrogen (Figure 5.10). The maximum pressure before destruction was then recorded [22, 23]. Even with the small residual amount of silicon nitride, burst pressures for MgF_2 nanomembranes are $\sim$2.7x weaker than the NPN template at the same membrane area (Figure 5.11). The power law relationship between burst pressures and window size indicates burst pressures greater than 5 PSI, a value that we have found is predictive of the successful assembly and use of nanomembranes in cell culture devices

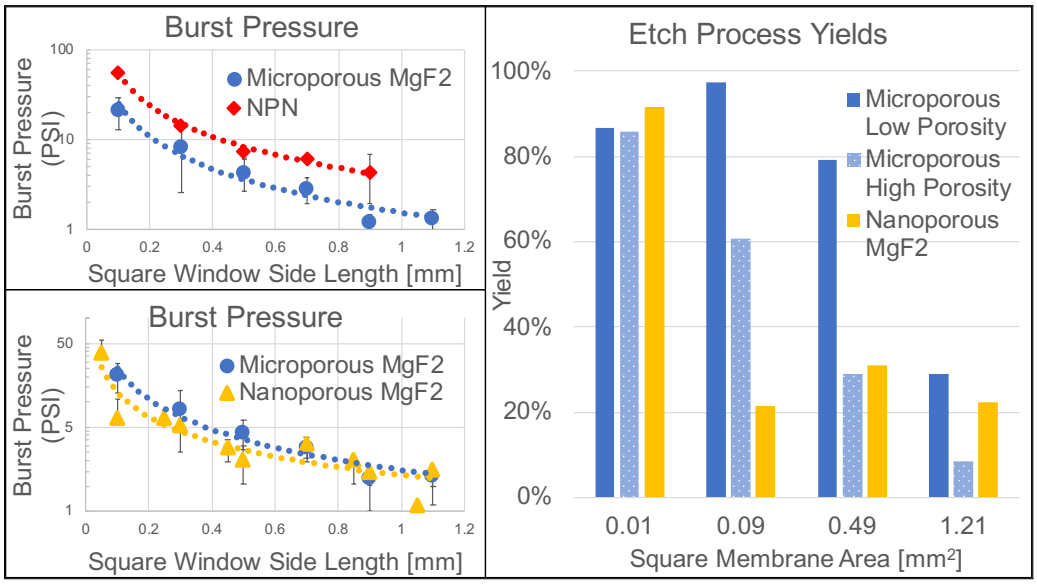

Figure 5.11: Mechanical MgF_2 Nanomembrane Strength. Membranes are burst with flows of nitrogen as an indicator of mechanical strength. (Left) Silicon nitride (NPN) is substantially stronger than both the fabricated npMgF$_2$ and μpMgF$_2$. By making the μpMgF$_2$ material thicker, we have modestly increased the burst pressure compared to the nanoporous variant. Error bars are 1 standard deviation. (Right) Similarly, the yields of each chip differ based on both the membrane area and the underlying template pattern.

[4]. This pressure is achieved for $\sim$0.2 mm square membranes or smaller for the npMgF$_2$ and 0.5 mm square membranes for the μpMgF$_2$. Even though the strength of fabricated microporous templates were not significantly different from one another with regard to porosity (Figure 5.7), there were noticeable impacts on yield through the etching phase (Table 5.2). We speculate that the flexibility of the thinner, higher porosity membranes may be causing the decrease in yield through the etching step, which would be ameliorated by scaffolding that reduces the effective window size.

5.4 Cell Culture

5.4.1 Cytocompatibility

To evaluate whether the evaporated MgF_2 material is cytocompatible, HUVEC cells were seeded onto MgF_2 nanomembranes and stained with a Live/Dead assay (Invitrogen L3224).

Methods

Four nanomembranes were placed flat-side up in a 6 well plate suspended over 1 mm high, 3 mm wide channels, allowing media to make contact to both sides of the nanomembrane. The chips were attached to gaskets isolating the top membrane area from each other (simple stiction). The gasket assembly was sterilized with autoclaving prior to use. The assemblies were placed in wells, then MCDB131 complete media was used to hydrate each channel. P7-P9 HUVECs were seeded on the on the flat surface of each chip (1:20 split of T-25 confluent flask, 20 μL/well). After letting the cells adhere for 1 hr, each well was flooded with 5 mL of media, and placed into the incubator. After 3-7 days, cells were stained with the Live/Dead stain (ThermoFisher Scientific, L3224) according to manufacturer's instructions, and then fixed with 3.7% formaldehyde and washed with PBS. The live stain used here is a Calcein AM stain (2 μM in D-PBS, green) which reacts to the live cell's esterase activity and requires intact cell membranes to re-

tain it, while the dead stain is ethidium homodimer-1 (4 μM in D-PBS, red), which is excluded by cells that have intact cell membranes.

Results

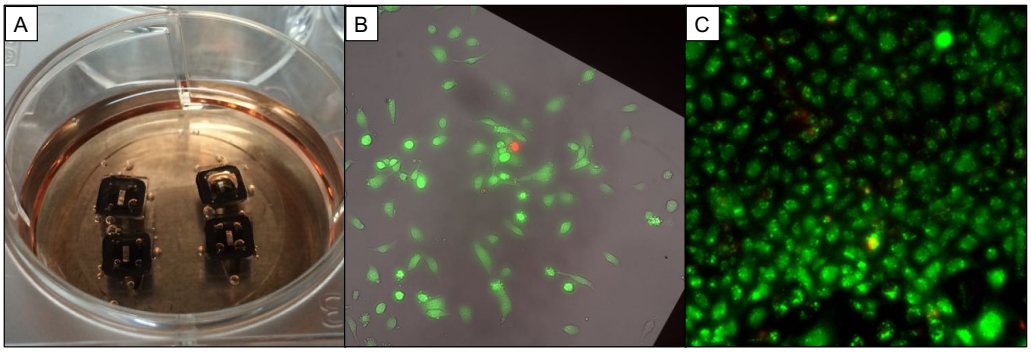

Figure 5.12: Live/Dead Stain on $npMgF_2/\mu pMgF_2$. (A) P7-P9 HUVEC cells were plated on MgF_2 nanomembranes in a 6 well plate on silicone gaskets, then the well was flooded with media. (B) Combined Phase/Fluorescence image of HUVECs on $npMgF_2$ after 3 days (Live = Green, Dead = Red). The black outline is the edge of the freestanding membrane (200 x 200 μm square). (C) Fluorescence image of HUVECs on $\mu pMgF_2$ after 7 days, 78-97% of cells survive.

Figure 5.12 demonstrates the general viability of the fabricated MgF_2 films. As the cells culture for longer times, the layer becomes more confluent. The large proportion of Live cells (78-98%) is to be expected as MgF_2 coverglasses are commonly used in Raman imaging of cells. We expect the material biocompatibility, however, the thin film manufacturing of the MgF_2 nanomembranes differs from the MgF_2 coverglasses in use. Coverglasses are fabricated by polishing down crystalline MgF_2 at a certain crystal axis orientation to thicknesses of $\sim$100 μm. Our evaporated

thin films contain elements of the materials that are found in the crucible, as well as being polycrystalline. Though manufactured in a different way, these images confirm that the evaporated MgF_2 thin film is suitable to grow and attach cells.

5.4.2 Cell Culture

To demonstrate the utility of the permeable Raman substrates, we cultured ARPE-19 cells on the nanomembranes for 3-4 weeks, and evaluated the cultured cells for a permeability-dependent phenotype (ZO-1 expression). It is well known that these cells do not polarize well on TCP, as evidenced by the lack of ZO-1 staining [130]. This cell line is used in models of retinal epithelial fluid transport, and would have value in transport studies of pharmacological agents across the blood-retinal-barrier for drug discovery.

Methods

$npMgF_2$ Cell Culture

ARPE-19 cells were cultured on tissue culture plastic (TCP), Transwell inserts (polyester, 0.4 μm pores, Corning Inc.), and $npMgF_2$ nanomembrane chips. The chips were positioned into a Transwell insert that had the filter removed and then were sealed using PDMS, a biocompatible polymer, creating a two-compartment Transwell with a nanomembrane element. Af-

ter an ethanol sterilization, P27 ARPE-19 cells were seeded in a 12 well plate (100,000 cells/well) on MgF_2 nanomembrane inserts, polyester Transwells, and non-porous tissue culture plastic, having previously incubated the substrates in media (DMEM:F12,penicillin (100 U/mL), streptomycin (0.1 mg/mL), amphotericin (0.25 μg/mL) and Fetal Bovine Serum (FBS, 10% v/v,)) for 3 hours. Cells were grown over 3 weeks in an incubator (37 $^{\circ}$C, 5% CO_2) to confluence on these substrates, exchanging the media every other day.

Confluent cell monolayers were washed with PBS and fixed in 4% paraformaldehyde for approximately 10 min at room temperature. Cells were then washed 3 times with PBS and permeabilised by incubating with Triton X-100 (0.1% v/v in PBS) for approximately 10 min. Cells were then washed with PBS, followed by the application of 1% BSA/PBS for approximately 1 hour. Thereafter, BSA/PBS solution was aspirated and replaced with mouse, anti-human ZO-1 (primary) antibody, diluted in 1% BSA/PBS. Cell samples were incubated with the primary antibody overnight in the fridge. The primary antibody solution was then removed and cells washed with PBS (3 times). FITC-labelled goat, anti-mouse (secondary) antibody, diluted according to manufacturer's instructions in 1% BSA/PBS was then applied to the cells for 1 hour. The secondary antibody solution was then aspirated and cells washed with PBS extensively. The Transwell filter membrane was excised and mounted on glass slides (using DAPI-containing, ProLong Gold antifade/mounting medium) for confocal imaging, which was

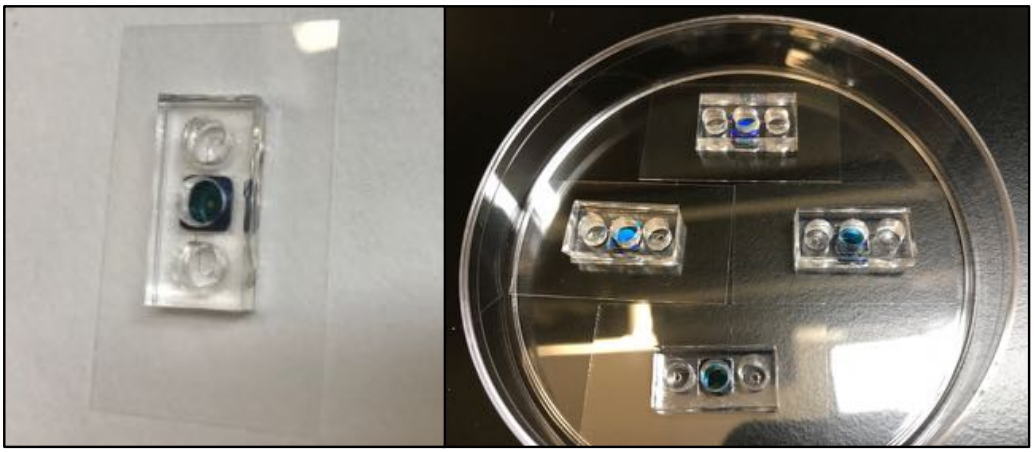

Figure 5.13: μpMgF$_2$ Cell Culture Devices.

performed using a Leica TCS SP2 system mounted on a Leica DMIRE2 inverted microscope (University of Nottingham). Image stacks were reconstructed using ImageJ.

μpMgF$_2$ Cell Culture

Thin 300 μm silicone gaskets (Specialty Silicon Fabricators) were cut using a computer controlled knife cutter (Silhouette CAMEO). These gaskets were manually aligned to create microfluidic channels above and below the MgF$_2$ nanomembrane, with a 5 mm thick PDMS block on top with wells as a media reservoir. These layers were bonded using UV-ozone for 15 minutes at 100 W and cured at 70 °C overnight (Figure 5.13). The active area for cell growth is the top well for the device, 4 mm diameter circle.

Devices were autoclaved, and COSTAR inserts (polycarbonate, Corn-

ing, Cat. No. 3413, 400 nm pores, 10 microns thick) were sterilized by ethanol immersion for 1 hr. ARPE-19 media with 10% FBS was then incubated in all devices and wells for 1 hr. Autoclaved DI water was placed in each plate to provide a local source of humidity. P5-P9 ARPE-19 cells were seeded into devices (2000-4000 cells/well), inserts, and tissue culture plastic wells at 5 x 10^5 cells/cm^2. Growth was imaged on μpMgF$_2$ nanomembranes, tissue culture plastic and COSTAR inserts, with a phase-contrast microscope. Cells were grown in an incubator (37 C, 5% CO_2) and media was replaced 3x a week (MWF) for 28 days.

Cells were fixed using 4% paraformaldehyde in ARPE-19 media for 15 minutes (4 $^\circ$C), then washed 3x with PBS and permeabilized using 0.1% Triton X-100 for 7 minutes. The cells were washed, and then blocked with 1% BSA in PBS for 1 hr to limit aspecific binding at room temperature. Primary rabbit-antihuman ZO-1 antibody (HPA001636, Millipore Sigma, 1:200 dilution) was added to each device and incubated overnight at 4 $^\circ$C. The following day, the cells were washed 3x, and then the secondary goat-produced FITC-antirabbit antibody(F0382, Millipore Sigma, 1:50 dilution, 50 microliters) was added for 1.5 hrs. Devices were washed 3x and counterstained with DAPI (1 μg/mL), and mounted onto coverslides with ProLong antifade solution. Confocal stacks were gathered on Leica (SP8), Olympus (Fluoview FV1000) and Zeiss (LSM 880) microscopes. Pinhole diameters ranged from 51-105 μm, with 560-600 ns pixel dwell times. Images were processed using ImageJ, with max-intensity Z-projections to

merge layers.

Results

Having characterized the basic mechanical, material, and cytocompatible properties of MgF_2 nanomembranes, we then investigated their viability as RPE cell culture substrates. A confluent monolayer of ARPE-19 cells was cultured over 3 weeks on npMgF_2 nanomembranes and polyester Transwells (21 days), as well as non-porous tissue culture plastic controls (23 days) and then stained for the tight junction protein (ZO-1) to evaluate cell morphology (Figure 5.14, 5.15). The fragility of the npMgF_2 was a challenge as only 20% of the nanomembranes survived the full 21 days. Bubbles were a primary cause for concern under the nanomembrane areas, as the region of high surface tension could cause them to rupture. The mosaic appearance of the protein on permeable MgF_2 nanomembranes is a desirable trait of long term epithelial cell culture that only occurs if the substrates are permeable [129, 130]. These junctions appear punctate on the porous part of the nanomembrane and lack a completely continuous boundary as on the polyester transwell, which may mean that the development of the whole mosaic was delayed. Non-porous tissue culture plastic does not form the mosaic at all (Figure 5.14)b. There are observed differences in the ZO-1 signal to background noise ratio in Figure 5.15; the mosaic stains on the nanoporous substrate appear less clear. While different types of objectives (water and oil) were used for imaging, this could

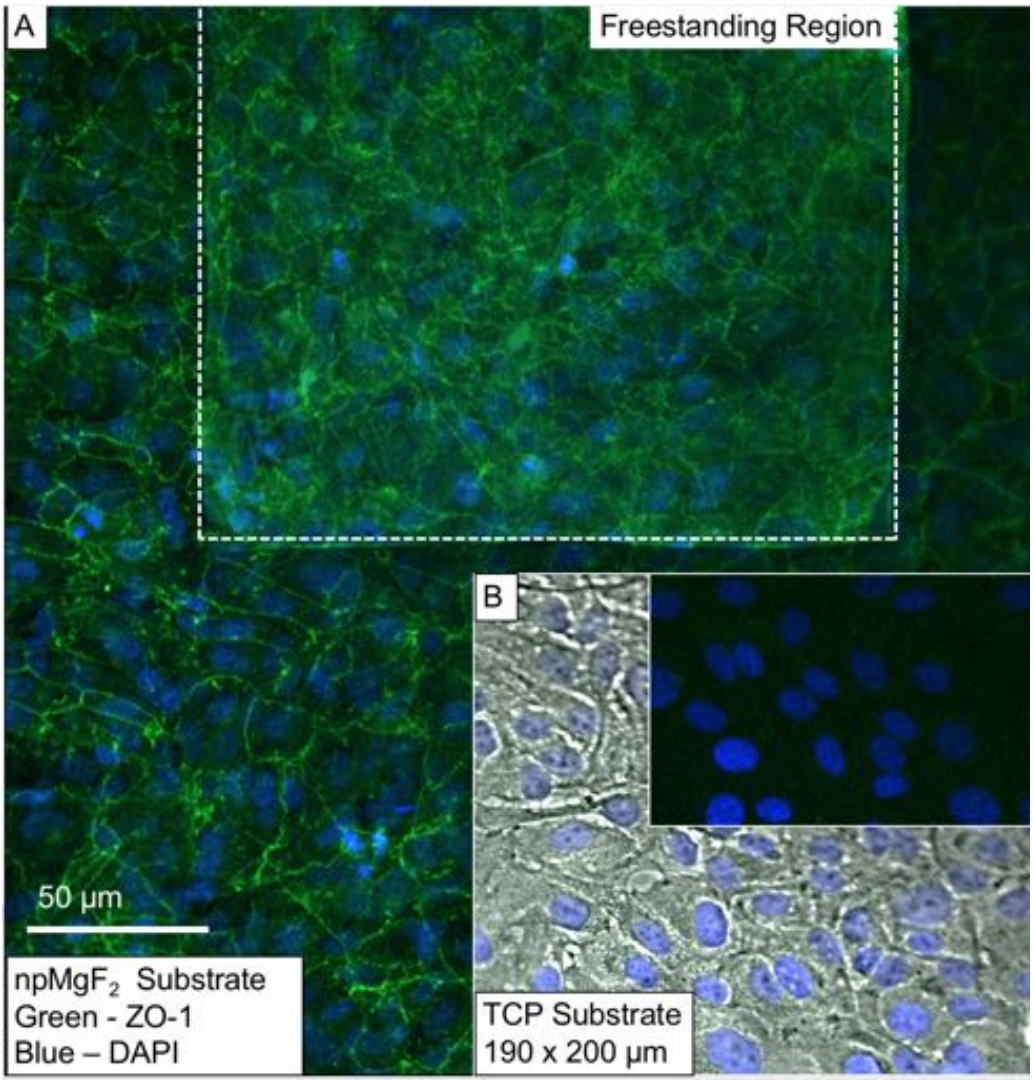

Figure 5.14: ARPE-19 ZO-1 Expression on $npMgF_2$ and TCP. (A) P27 cells grown on freestanding $npMgF_2$ and the surrounding region show a ZO-1 mosaic. (B) Brightfield composite image of cells grown on tissue culture plastic, lacking a ZO-1 mosaic. (inset) DAPI and ZO-1 stains alone.

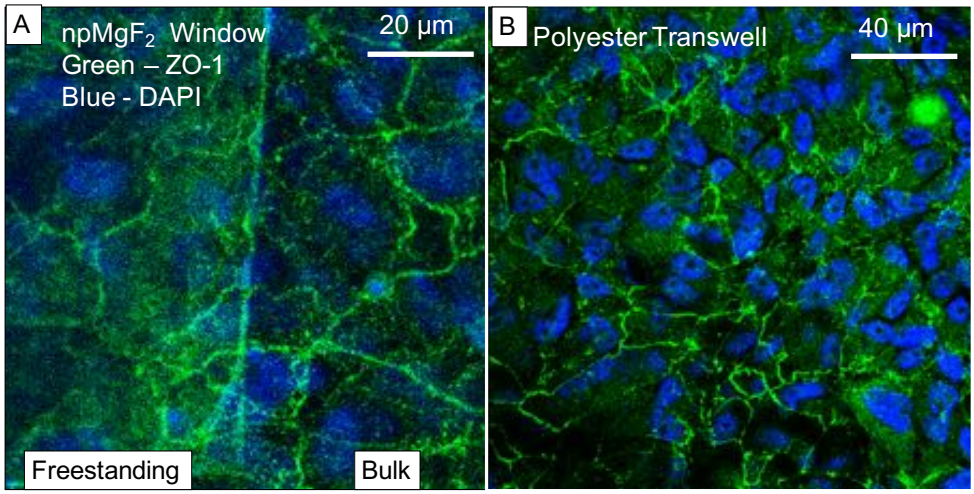

Figure 5.15: ARPE-19 ZO-1 Expression on (A) $npMgF_2$ (40x oil objective) and (B) Polyester Transwell (40x water objective).

be a difference in staining as only a small part of the $npMgF_2$ is permeable and we observe differences between the free-standing and bulk parts of the substrate.

To confirm similar ZO-1 expression on $\mu pMgF_2$, a confluent monolayer of ARPE-19 cells was cultured over 4 weeks on $\mu pMgF_2$ nanomembranes and polycarbonate Transwells, as well as non-permeable tissue culture plastic controls and then stained for the tight junction protein (ZO-1) to evaluate cell morphology. Figure 5.16 displays representative brightfield imaging of the cells throughout the cell culture, showing that the cells on the $\mu pMgF_2$ nanomembranes can be seen as easily on a standard tissue culture plastic substrate, while the polycarbonate Transwell is mostly opaque in this mode. The striation in lighting on the $\mu pMgF_2$ is created from re-

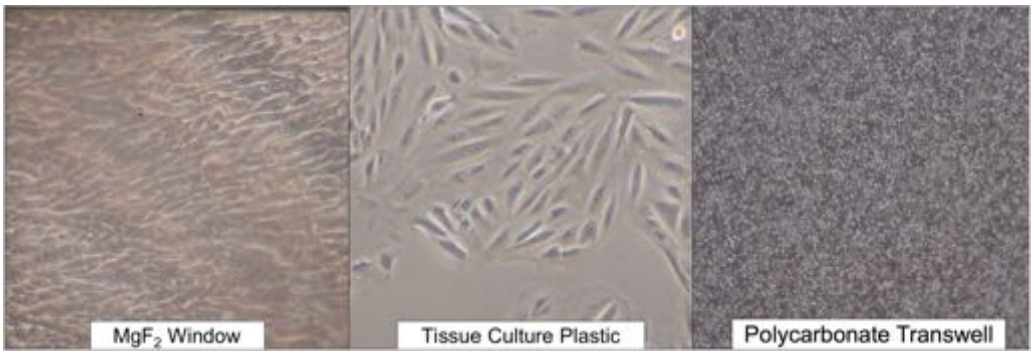

Figure 5.16: P7, D5 ARPE-19 Brightfield Images with Phase Contrast on Experimental Substrates. The cells on the polycarbonate Transwell are not easily visible, but the cells on the μpMgF_2 nanomembranes are as visible as tissue culture plastic. 20x images, air objective.

flections in the device and is not indicative of the clarity of the MgF_2. The cell density is less dense on tissue culture plastic than μpMgF_2, even after 5 days of growth. This could be due to a few different factors, such as a higher density of cells in the devices, or the nanomembrane sagging, creating a lower height on which cells could settle, or cells actively migrating toward the more permeable region in the device. Therefore, confluence occurs in the nanomembrane devices a few days before that of the other substrates, becoming contact inhibited. This may create differences in cell maturity between the experimental substrates, but evaluated over the course of a few weeks, these differences should be small.

Evaluating the ZO-1 stain alone (Figure 5.17), the cells grown on the nanomembrane's windowed region and outside it (Bulk MgF_2) display similar ZO-1 mosaics to that cells grown on polycarbonate Transwells. The clearest imaging is on the non-permeable part of MgF_2 substrate, which

lacks much of the background stain not localized to the ZO-1 mosaic. Compared to the Transwell, cells on the μpMgF$_2$ chip have more orderly mosaics. The expression of ZO-1 on the non-permeable regions of the μpMgF$_2$ chips may indicate a lack of adherence to the substrate, as micropatterned wells or textures could form pockets of a basolateral compartment for nutrition and secretion, thus creating the appearance of a permeable substrate. These pockets could then be accessed through the free-standing window region, allowing media exchange out of these areas.

We also observe a ZO-1 mosaic on the non-porous tissue culture plastic substrates. This is unexpected as these cells do not usually show ZO-1 expression on these substrates [130]. However, there is some existing evidence that confluent monolayers can express ZO-1 after 10 days of culture. Pasovic et al. [137] examines the culture and storage of ARPE-19 cells on glass coverslips and Nunclon $\triangle$ Multidishes at different temperatures. Here, they culture cells over 3 days (control) and then additionally store them for 7 days at varying temperatures. These cells demonstrate ZO-1 mosaics of varying quality (Figure 5.18). Yoshikawa et al. [138] also cultures ARPE-19 cells on poly-L-lysine coated coverglasses and exposes the confluent culture to endoplasmic reticulum stresses. The controls show a level of ZO-1 expression even without this stress.

We have unevenly observed ZO-1 expression on our tissue culture plastic substrates. Evidence from the literature described above suggests not all tissue culture plastic behave equivalently. Different manufacturers

may apply a different coating to their substrates which may influence the phenotype of cultured cells. Even though specialty plates exist that are pre-coated with collagen or poly-l-lysine, they were not used here. This means that we should use other metrics of cell phenotype and polarization, such as molecular transport studies across the cultured cell layer and electrical resistance characterization to verify the response of ARPE-19 cells on MgF_2 nanomembranes. Cell barrier permeability can be assessed through small molecule transport with a known concentration of molecules (ranging in size from 10 kD to 10000 kD) by introducing them to the apical side of the cultured cells, then measuring the concentration of molecules that reach the basolateral compartment. Similarly, the transport of charge carriers across the cell layer can be measured through direct electrical measurements (transepithelial electrical resistance), or the whole system can be modeled to extract relevant capacitive and resistive values (impedance spectroscopy). These experiments remain to be performed in the future.

The composite ZO-1/DAPI stain reveals many more nuclei than can be associated with the mosaic (Figure 5.19. Some of these nuclei bridge the gap across tight junctions, indicating that there are multiple cell layers, which can be normal in confocal imaging of cancer-derived epithelial cells, as the tight junctions are apical to the nucleus. It is possible that these additional cells were a contaminating fungal infection, though the visual indicators of the media remained clear. However, it is possible that more cells continued to crawl and pack over top each other, even beyond contact

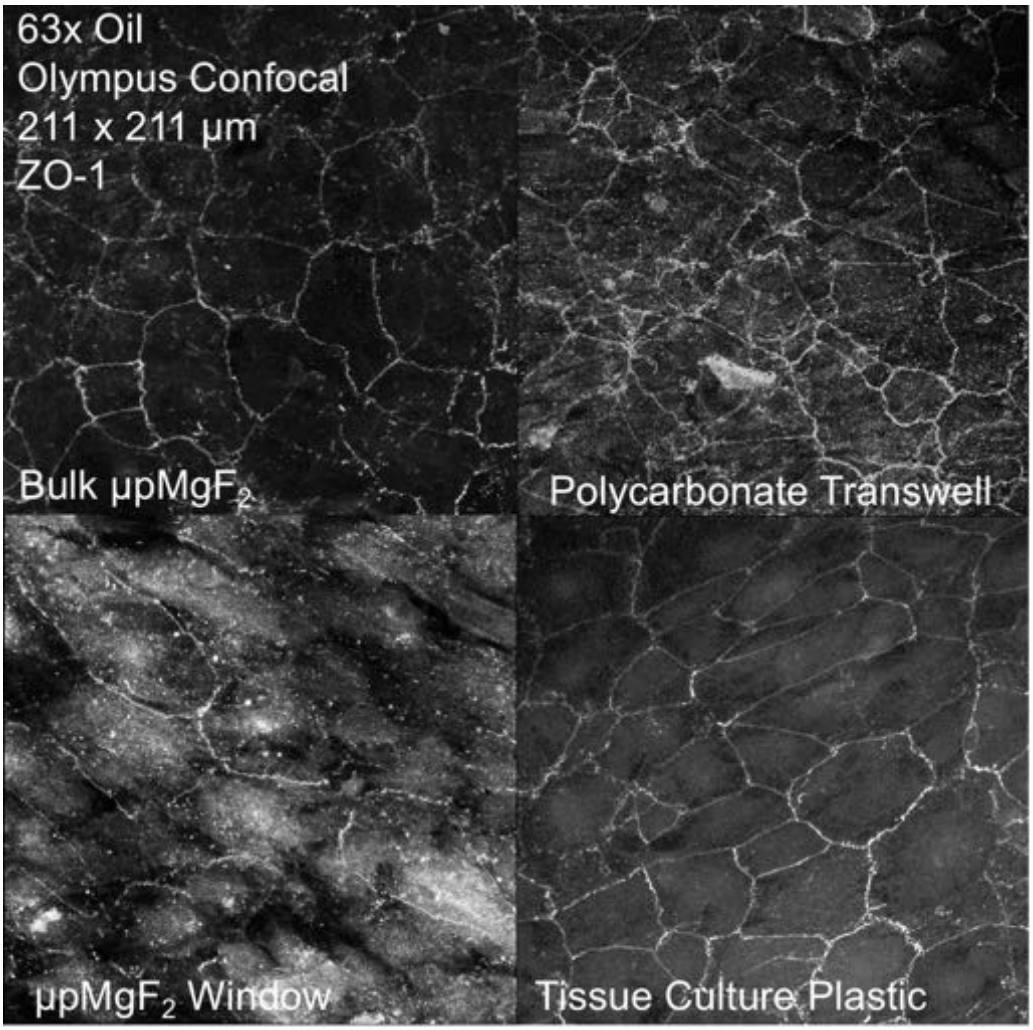

Figure 5.17: P9, D29 ARPE-19 Cells Grown on μpMgF$_2$, TCP, and Transwell Substrates Express ZO-1.

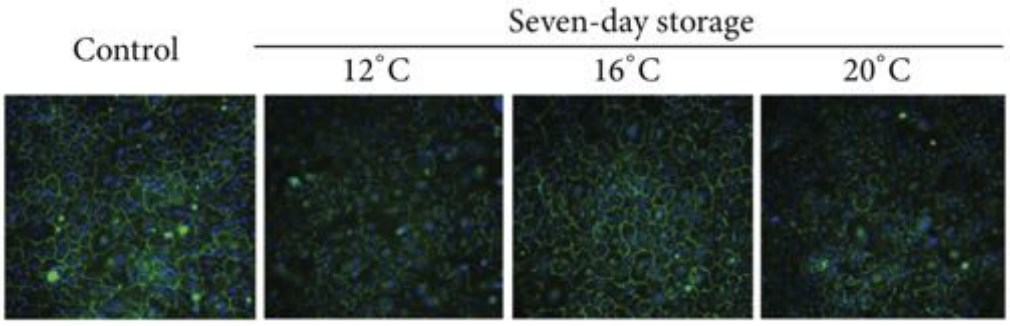

Figure 5.18: ARPE-19 Cells grown on Nuclon Multidishes express ZO-1. Control cells were grown for 3 days before being stained with ZO-1 (green) and DAPI (blue). Temperature variants were stored for an additional 7 days before being stained. Adapted from Pasovic et al. [137], Creative Commons License (CC BY 3.0).

inhibition. A higher density of nuclei is also observed on the tissue culture plastic substrate and the Transwell, which indicate that it is not an effect of the experimental nanomaterial alone. While this experiment shows a few differences between the $npMgF_2$ and $\mu pMgF_2$ substrate, ultimately both fabricated substrates were successful in creating ZO-1 expressing ARPE-19 cells over 3-4 weeks of culture.

5.5 Raman-Mapping

5.5.1 Methods

Calu3 lung epithelial cells were deposited on silicon and $npMgF_2$ nanomembranes and allowed to adhere to the substrate. These cells were chosen for their easier attachment over ARPE-19 cells. Raman measurements were

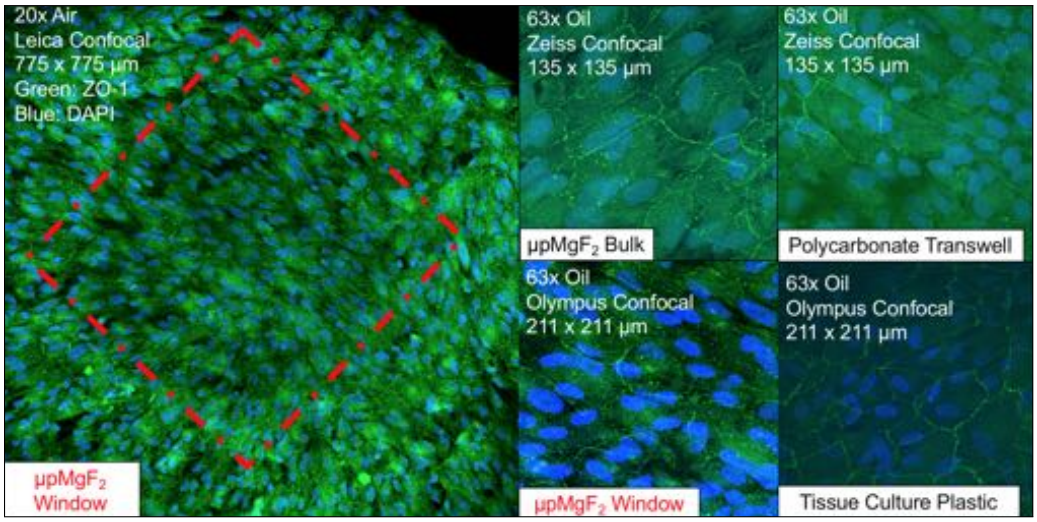

Figure 5.19: Multiple Cell Layers in μpMgF$_2$ Culture Experiment. The presence of many more nuclei than mosaic boundaries indicates that there are more cells than a single confluent monolayer would suggest.

made on cells using a bespoke Raman instrument (University of Nottingham). Raw spectra were processed using principal component analysis (Matlab) to map biomolecules.

5.5.2 Results

An example Raman map of a cell on a pnc-Si membrane shows DNA and RNA signatures localized to the nucleus and cytoplasm respectively. It took over 2.5 hours to make a small map of this cell, using a 5 mW illumination intensity. This is not ideal for making measurements of other molecules that may have different localizations over time. Combatting the silicon's propensity to absorb the illumination light (Figure 5.1) necessitated

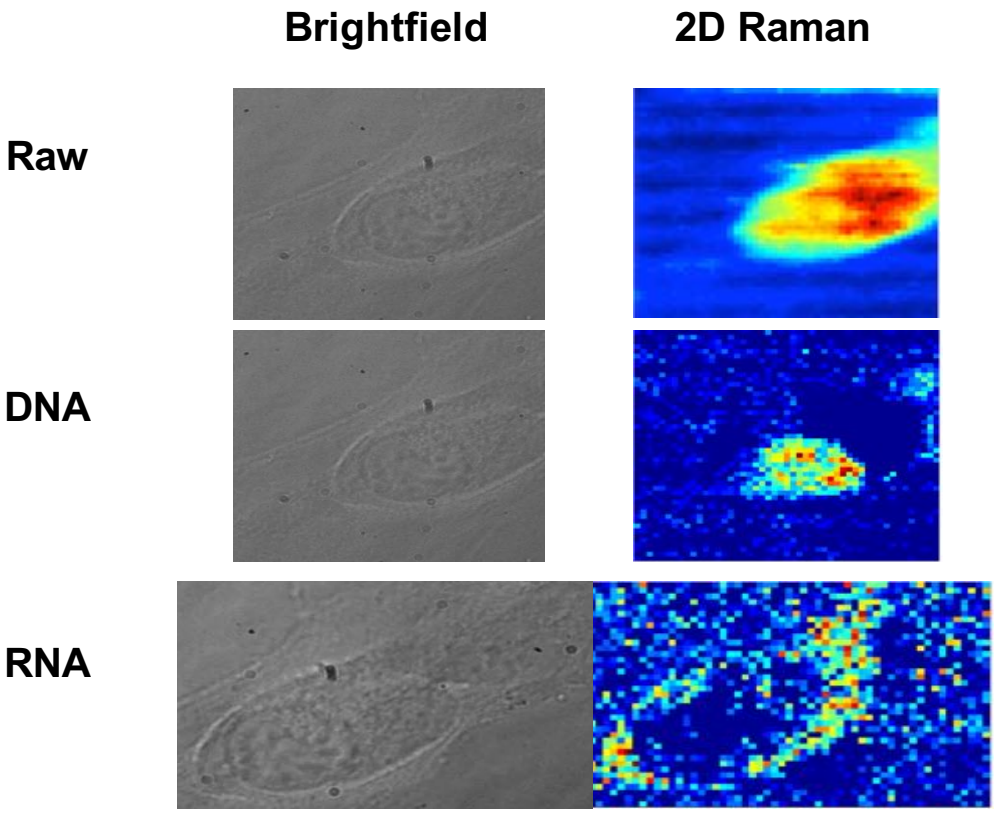

Figure 5.20: Raman Mapping of RNA and DNA on pnc-Si.

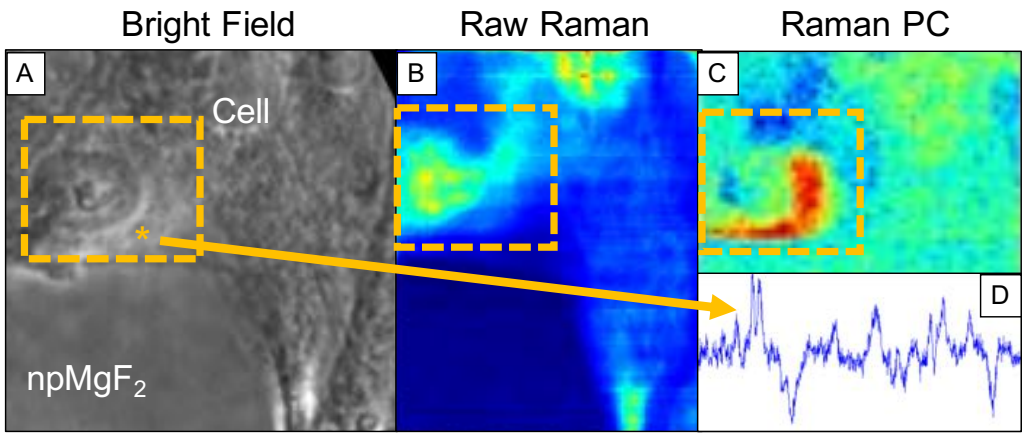

Figure 5.21: Raman Mapping of RNA on $npMgF_2$. (A) Bright field image of cell fixed on $npMgF_2$. (B) Raw Raman map. The orange square indicates the same region by the cell's nucleus (100x70 pixels). (C) Principal component map, associated with RNA. (d) Raman spectrum of point away from cell nucleus. The dual spectral peaks (indicated by orange arrow) align with those established for RNA (783, 811 cm^{-1} [139]).

the move to new Raman-compatible materials (MgF_2), while still maintaining the porosity of the original template.

The Raman compatibility of the evaporated MgF_2 material was established by depositing Calu3 cells on $npMgF_2$ substrates and making point measurements that localized biomolecules to regions within each cell (Figure 5.21). We can see the bright field image of a cell with its nucleus as a point of reference between each image. The raw Raman map is associated with more material in the observation volume and tracks with highlighting the thicker nucleus-containing regions. Utilizing principal component analysis of the raw Raman map, we can observe a Raman signature associated with RNA, localized to areas around or within a cell's nucleus. While the cell culture was infected (reported by collaborators), we can still ob-

serve distinguishable biomolecule signatures and correlate them with microscopic features in the cell. As higher illumination powers are available for measurement, information can be obtained more quickly. The fabricated npMgF_2 scaffolds can tolerate up to 450 mW of laser power without disintegrating, meaning that the primary barrier to quicker measurements would be the amount of laser power the cells can tolerate. The thinness of the nanomembrane (50 nm) contributes to the reduced background signal; the cellular component dominates over significantly less nanomembrane volume (approximately 5% of the cell's volume), without regard to the relative Raman cross-sections of the materials. Furthermore, it would be difficult to measure any particular changes in Raman spectrum based on the substrate's structure as there is little material in the observation volume (compared to a 100 μm-thick MgF_2 coverglass), evinced by the homogeneous background. Developing new μpMgF_2 membranes after the mechanical failures with npMgF_2 led to delays in making Raman maps on this material. Because of some technical difficulties with the microscope in Nottingham and the delivery of the material, it was not possible to perform the same experiments with μpMgF_2. Given the extensive validation of the material properties of μpMgF_2, we believe the initial experiments on npMgF_2 nanomembranes are representative of the results we will obtain on μpMgF_2.

5.6 Challenges and Future Directions

As a Raman measurement will necessarily sample the different materials in it's observation volume, it has been difficult to maintain material purity. Sending manufactured MgF_2 nanomembrane materials to others has not been trivial. The standard silicone-lined gel-boxes that are commonly used to ship chips had the unintended effect of depositing a thin layer of a PDMS substance on the membranes. To combat the outgassing of this material, we developed a 3D printable chip holder model out of ABS plastic, in which we could then insert individual chips (Figure 5.22). While usable, the thermoplastic is not ideal for these purposes, as it is prone to shed particles after extrusion. A milled aluminum holder would offset these issues, but the cost of the holder would exceed the cost of the chips.

The mechanical weakness of npMgF_2 led us to develop thicker, μpMgF_2 variants as a way to increase strength. The difference between the two is modest, but ultimately practical. When shipping fixed cells on membranes, the microporous membranes remain intact (2/3 chips), while no nanoporous membranes survived in the same box (0/7 chips). However, making the MgF_2 membrane thicker led to it's own host of challenges, evinced in the new defect modes of failure. At the sub-micron scale, the stresses of MgF_2 most readily lead to cracking. Placing micropores on the edges of the nanomembane windows may exacerbate these defect modes; patterning micropores on the nanomembrane template away from

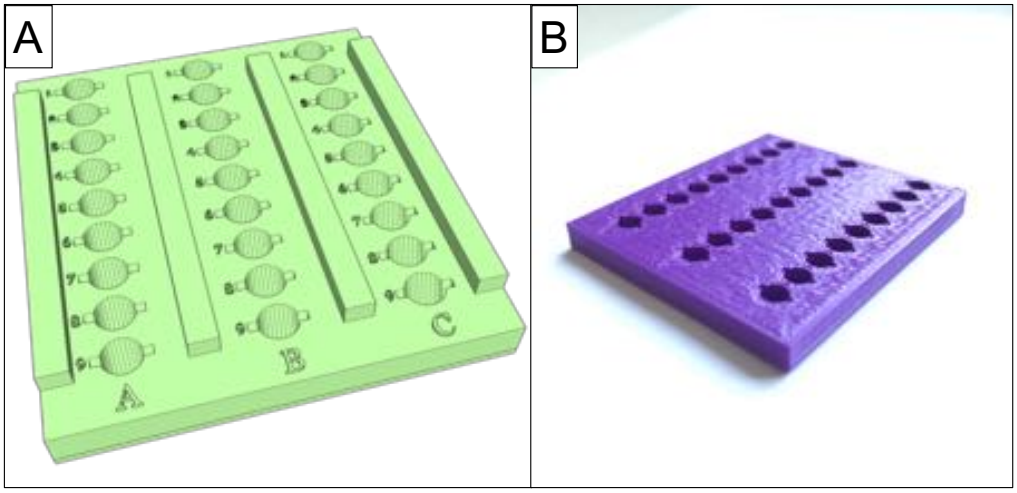

Figure 5.22: 3D Printed Storage Block. (A) Storage block insert designed for shipping 27 individual 5.4 x 5.4 mm chips in a gel-box. Beams between columns help prevent the chips from being stressed by the roof of the box. (B) Example storage block made of extruded ABS plastic without support beams.

these edges should help improve yield and strength.

The etch selectivity of MgF_2 also provides a difficult fabrication challenge, as it is difficult to remove the material once deposited. The largest pores in production on the silicon nanomembrane platform are 8 μm diameters. If we were to try and make the nanomembrane even thicker for more stability, this size will put an upper limit on the thickness of the material. The larger pore size would also be a concern for cell attachment, as larger pore sizes tend to have an adverse effect on cell adhesion. The 0.5 μm pore template size used in this work could ultimately have a $\sim$1 μm MgF_2 maximum film thickness, with severely reduced porosity.

These challenges demonstrate that there is still a substantial process

window for further improving the mechanical properties of these materials, while still maintaining the desirable Raman-compatibility and porosity characteristics. While there have been many complications, the membranes have been useful to establish cell culture on these evaporated thin films, which is a necessary first step before delving into more specific physiological questions.

5.7 Conclusions

We have demonstrated the fabrication of freestanding, ultrathin MgF_2 nanomembranes using NPN and microporous SiN membranes as a template. Future improvements could be made to increase the mechanical strength of these materials, such as adding a support structure to the freestanding film. The new material can withstand higher illumination intensities, which will lead to decreases in interrogation time for measurements made using Raman spectroscopy. The new cytoscaffolds are biocompatible, and can support cell culture for up to 4 weeks, allowing epithelial cells to develop a healthy morphology. These nanomembranes will become even more valuable when experimental imaging can be combined with transport studies on the cultured cells. Furthermore, the strategy used here can be extended to create other new nanomembranes out of different materials.

Chapter 6

Silicon-Based Nanomembrane Use in Surfaced-Enhanced Raman Spectroscopy

6.1 Introduction

Thus far in this thesis, silicon-based nanomembranes have been used as passive elements, as a structural guide for DNA or a cell culture substrate. Their material and structural properties have been examined as parts of a greater system that operates and senses biomolecules through other means. However, a silicon nanomembrane itself can be used as an active sensor [17]. This chapter details the structural, material, and functional characterization of a new chemical sensor that relies on a hybrid silicon-based nanomembrane structure to enhance Raman signals of bound analytes. I begin by reviewing essential theory of Surface-Enhanced Raman Scattering (SERS) based sensors.

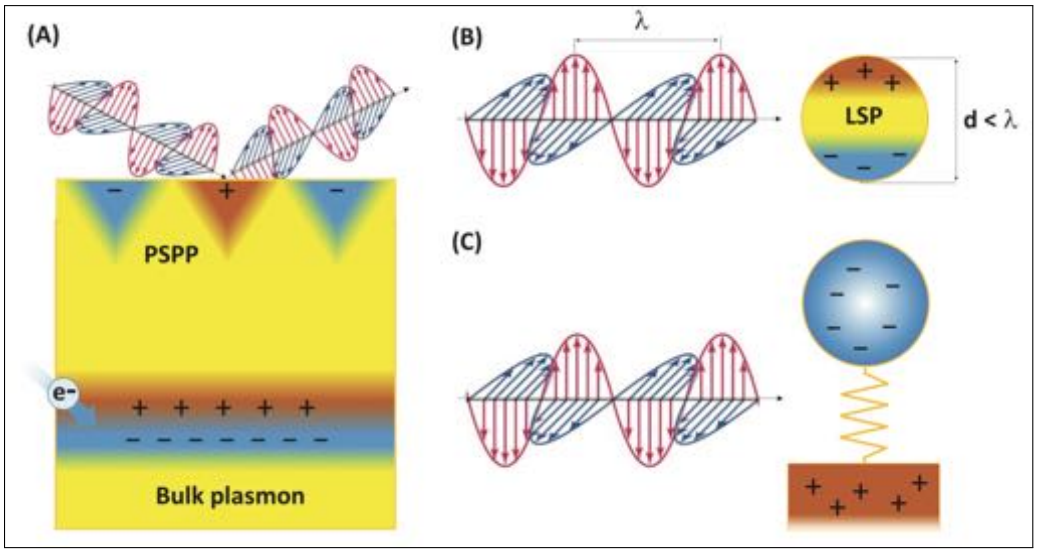

Figure 6.1: Surface Plasmon Illustration. Graphical illustration of plasmons in bulk gold (A) and nanoparticles (B). (A) Bulk plasmons can be excited by an electron beam (bottom), while PSPPs are excited by the evanescent field of light (top). (B) LSPs are excited by light propagating in free space or dielectric media. (C) The LSP in Au nanoparticles can be modeled, as a first approximation, like a spring-mass harmonic oscillator, where the free-electron density is the equivalent of the mass. Reprinted by permission from Copyright Clearance Center: IOP Publishing, **?**], Copyright 2017.

6.2 Surface-Enhanced Raman Scattering (SERS) Theory

Spontaneous Raman, described in Chapter 1, is a useful technique for gathering information about the types of material in an observational volume. However, the effect is very small and inefficient. In the early 1970s, stronger Raman spectra were observed when pyridine molecules were imaged on roughened silver electrodes [140]. Given the constraints of spontaneous Raman measurements, this seemed impossible [141]. At the

time, other researchers expected $\sim$25 cps (991 cm^{-1}) for 1 W of laser power; Fleischmann et al. [140] measured $\sim$500-1000 cps for 0.1 W of laser power [141]. This phenomenon was debated for a few years; SERS was first observed in 1973, but not correctly understood as SERS until 1977 [142]. The anomalously strong signals were not wholly a product of surface roughness, as Jeanmaire and Van Duyne [142] showed there were optimal roughening conditions for this effect, producing an enhancement of $\sim$10^5-10^6. Around the same time, Albrecht and Creighton [143] independently showed that the increase in surface area, and thus more pyridine molecules in the observation, could not solely account for the stronger Raman spectra gathered.

Understanding the basic mechanisms thought to be behind SERS requires knowledge of electromagnetic theory. To begin, phenomena known as surface plasmons are essential to generating a SERS response. A plasmon is a collective oscillation of electrons in a metal [**?**]. These oscillations can be induced by other electromagnetic fields (light) along the surfaces of metals, which then is known as a surface plasmon polariton (SPP). Polariton oscillations can travel along the surfaces of metals, but not in the bulk volume of the film (Figure 6.1A). If the metal film is thin enough (sub 100 nm), the plasmon does not propagate and instead is a localized surface plasmon (LSP, Figure 6.1B).

The layer in Figure 6.1 is made of a precious metal, such as copper, silver, or gold, which have been valued since antiquity for their brightness

and shine, hereafter referred to as ”coinage” metals. The reason for their appearance is their strong reflectance of light across the visible spectrum. This is due to a strong negative real-component of the refractive index for these materials, which is important to generating plasmons. Once the complex refractive index (real and imaginary components) of the material is understood, Maxwell's equations can be solved to determine the electric field around nanostructures. However, there are only a few analytical solutions for simple geometries and most calculations rely upon numerical analysis [144].

A common simplifying assumption is to treat the field as static, which is an excellent assumption for features much smaller than the wavelength of incident light. For visible light with 500-600 nm illumination, the assumption is valid for $\sim$10 nm features, though this simplification is often used for larger features [144]. In the case of a metal 2D cylinder surrounded by a medium, the solution for the strength of the induced dipole's moment (P) constrained by the shape of the cylinder is approximated as [144]:

$$P \propto \left(\frac{\epsilon(\lambda) - \epsilon_m}{\epsilon(\lambda) + \epsilon_m} \right) \tag{6.1}$$

where $\epsilon(\lambda)$ is the wavelength dependent refractive index of the metal and ϵ_m is the refractive index of the medium. As the coinage metal has a negative real-component to the refractive index, this portion can cancel out with the medium's refractive index in the denominator, vastly increasing the

strength of the field. For a metallic 3D spherical particle surrounded by a medium, the equation is very similar [144],

$$P \propto \left(\frac{\epsilon_p(\lambda) - \epsilon_m}{\epsilon_p(\lambda) + 2\epsilon_m} \right), \tag{6.2}$$

with scattering (C_{sc}) and absorption (C_{abs}) cross-sections given as [145]:

$$C_{sc} = \pi a^2 * \frac{8}{3}(ka)^4 \left| \frac{\epsilon_d - 1}{\epsilon_d + 2} \right|^2 \tag{6.3}$$

$$C_{abs} = \pi a^2 * 4ka \; Im \left[\frac{\epsilon_d - 1}{\epsilon_d + 2} \right] \tag{6.4}$$

where $\epsilon_d = \epsilon_p(\lambda)/\epsilon_m$, a is the particle radius, k is the wavevector in the medium. Thus, the LSP resonance will occur for differently sized structures at different wavelengths as long as the boundary conditions along the structure are met (the denominator term in Equation 6.1 and 6.2). The intensity enhancement factor (IEF) of the field is then given as

$$IEF(r, \omega) = \frac{|E(r, \omega)|^2}{|E_0(r, \omega)|^2}, \tag{6.5}$$

a ratio of the induced ($|E|^2$) to native intensity ($|E_0|^2$). As the intensity in the region is proportional to the square of electric field, small increases in the electric field can create a much stronger intensity enhancement factor. If the surrounding medium changes from lower to higher refractive index (i.e. air to water), the resonance is red-shifted to accommodate the in-

dex shift [144]. For more complicated structures, the interaction between many different LSP resonances determines the overall LSP response of the structure. The spectrum of electromagnetic enhancements depend on the shape and size of individual particles and on the gaps between them [146].

If we consider a perfectly smooth, flat, coinage metal plate instead of a sphere or cylinder, IEF < 1 for normally incident light, meaning that the electric field is weaker, and the intensity in the region is quenched [144]. If the incident light is angled, these photons can create regions of enhancement as a traveling wave (SPP) or localized plasmon if the metal plate is thin (LSP). In reality, no metal surface is perfectly smooth. LSPs can be also assigned to features on a curved metal surface, which can have complicated boundary conditions, creating complex enhancements near these features. While the solution for particles can sometimes be solved, the solutions for arbitrary surfaces is not so simple.

With regard to SERS, the increase in a Raman scattering event at roughened surfaces is caused by two different factors: chemical or electromagnetic enhancement [147]. The total enhancement is then

$$I_{SERS} \approx SEF_{EM} * SEF_{CE}, \tag{6.6}$$

where SEF_{EM} and SEF_{CE} are the electromagnetic and chemical enhancements respectively. The electromagnetic enhancement stems from

the organization of the SERS sensor surface. Increasing the electric field around an analyte molecule is analogous to increasing the power of the laser that is illuminating the molecule [144]. As both the incident photon and scattered photon are in the presence of the increased intensity, they are both assumed to be enhanced by the same field, leading to an electromagnetic SERS enhancement factor (SEF_{EM}) [144]:

$$(SEF_{EM}) = (IEF)^2 = \frac{|E_{init}(r,\omega)|^2}{|E_0(r,\omega)|^2} * \frac{|E_{scat}(r,\omega)|^2}{|E_0(r,\omega)|^2} = \frac{|E(r,\omega)|^4}{|E_0(r,\omega)|^4}. \quad (6.7)$$

Some electromagnetic enhancement factors have been reported as high as 10^8-10^{11} [147]. The chemical enhancement is directly related to the bond structure of the analyte molecule and its electronic interaction with the coinage metal. Given the large non-linear variation in electromagnetic enhancement with a strong dependence on structure and position of analyte molecules, the chemical enhancement factor of SERS might be more attractive as a stable source of enhancement. Some chemical enhancement factors have been reported as high as 10^3 [148]. However, it is difficult to appreciably control the chemical enhancement factor of SERS in a general way, as this is reliant on the analyte bonding event, analyte's chemical structure, and light-induced charge transfer [149]. Therefore, the much larger SEF_{EM} is most commonly considered dominant, along with the $|E|^4$ scaling that goes with it.

The theory described above is not exhaustive. There are many other detailed mechanisms that can contribute to SERS, such as analyte orientation and surface-selection rules for nanostructures. However, this theory provides a basic understanding of the mechanism used to make a SERS sensor. The following work will focus on the structural enhancement provided by SERS substrates.

6.3 SERS Detection Substrates

6.3.1 Roughened Thin Films

The original discovery of SERS on a roughened silver film [140] has led to further investigation of the enhancements provided by roughened coinage metal films. The nanoscale features required for SERS are produced with simple wet etches (dependent on the metal, nitric acid, ammonium hydroxide). These etches can produce surface roughness on the order of R_q = 1 μm and structures that have ragged leaflets (Figure 6.2). The heterogeneity of the leaflets is useful to create a critical feature within which an analyte can bind and be enhanced. Given the large variance in structure, it is difficult to reproduce a consistent enhancement; 10^3-10^8 enhancement factors are reported [150]. The choice of material is often governed by what can be detected. Silver has the strongest extinction across the visible spectrum (used in mirrors), however, it can tarnish, and become poisonous to

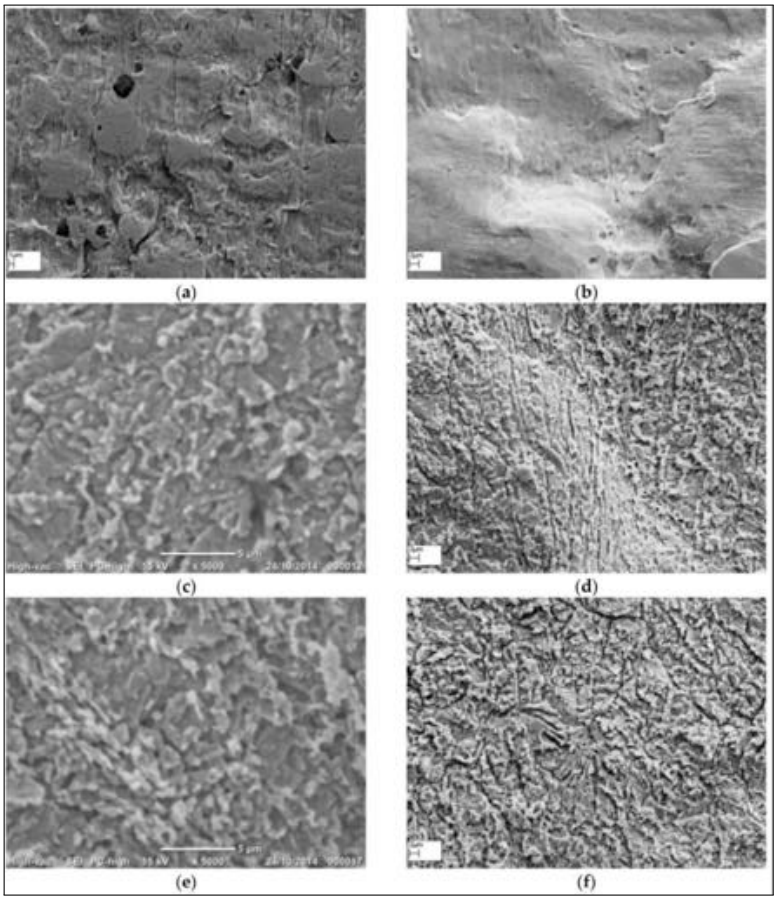

Figure 6.2: Roughened Silver Film. Effect of the different chemical etching treatments on surface morphology of Ag metal surface as seen under scanning electron microscope (SEM): (a) native as-flattened Ag wire; (b) 30 s NH_4OH; (c) 10 s HNO_3; (d) 2 m HNO_3; (e) 30 s NH_4OH followed by 10 s HNO_3; and (f) 30 s NH_4OH followed by 2 m HNO_3. Reprinted from Wijesuriya et al. [150], Creative Commons License (CC-BY-4.0).

biological samples. Gold is very inert and used widely with biological samples.

6.3.2 Metallic Nanoparticles

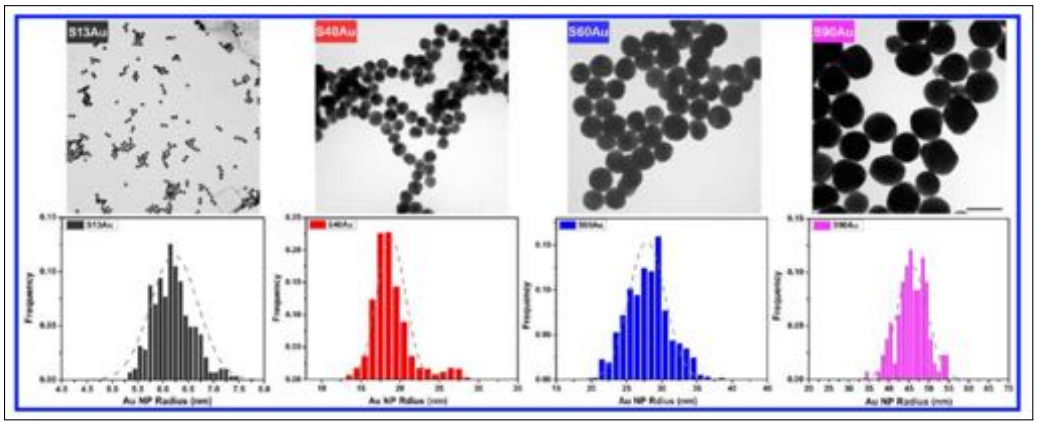

Figure 6.3: Au Nanoparticle Electron Microscopy. Upper: TEM images of various Au NPs dried from as-synthesized aqueous Au NP colloids. Lower: the corresponding radius histograms with fitted Gaussian distributions (gray dashed line). The scale bar is 100 nm for all TEM images. Reprinted with permission from Yang et al. [151]. Copyright (2017) American Chemical Society.

Nanoparticle plasmons have been utilized for centuries in stained glass windows. Medieval glassworkers found that suspensions of gold particles created within molten glass changed the color of the glass, allowing them to create deep shades of red [**?**]. The reason for this change is the plasmonic behavior of gold nanoparticles. The nanoparticle has a strong extinction coefficient that is related to the oscillatory resonance of electrons on the surface of the nanoparticle when illuminated (Equation 6.2). Further

analysis in our modern era showed that the nanoparticle shapes and sizes were extremely influential in modulating the extinction of solutions containing them. Nanoparticles sizes (i.e. 5-100 nm) can produce a range of colors, and changing the shape of nanoparticles from spherical to cube-like had similar effects [152]. As such, using these resonances is an effective way to create regions of electromagnetic enhancement.

The chief utility of the metallic nanoparticles as SERS substrates is that they are easier to create, obtain, and use than other methods. They can be very versatile and incorporated into many different kinds of experiments by simply adding a known concentration of particles to substrates with different structures. Researchers can assemble or immobilize nanoparticles on a surface (Figure 6.3) and then introduce the analyte, or they can use the nanoparticles in suspension and bind the analyte through surface chemistry. Colloidal Au nanoparticles can be dried down into dense populations which can then be infiltrated with biological materials [153]. Even polymeric membranes can be infiltrated with dense numbers of nanoparticles [154]. However, large aggregates of nanoparticles have worse electromagnetic enhancement profiles than dimer or trimer configurations [155]. Nanoparticles themselves can be difficult to arrange on a surface, causing a lot of heterogeneity, and consequently the strongest enhancement is probably originating from a subpopulation of nanoparticles [156]. This limitation is most evident by examining the enhancement on multiple samples or at multiple points within a sample. As a way to make the enhancement more

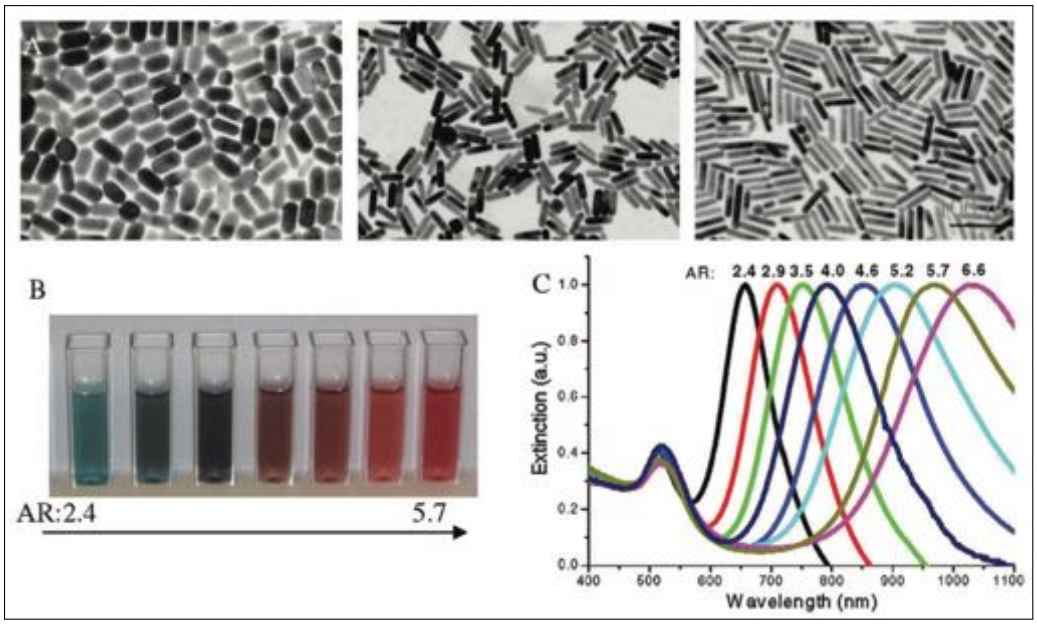

Figure 6.4: Tunable Optical Properties of Gold Nanorods by Changing the Aspect Ratios. Gold nanorods of different aspect ratios exhibit different dimensions as seen by TEM (A), in different color (B) and different SPR wavelength (C). Adapted from Huang and El-Sayed [158] with permission from Elsevier. Copyright 2010.

consistent, researchers have coated particles to fix the distance between dimers [157]. Examining the resonances and enhancement profiles of Si-coated Au nanoparticle dimer and trimers suggests that the enhancement factor of these structures is relatively consistent, but the LSP resonance can shift widely across the visible spectrum [157].

Considering the size of spherical nanoparticles alone, Rayleigh scattering describes the elastic light scattering of particles that are much smaller than the wavelength of light, while Mie theory describes particles that are closer in size to the wavelength of light [145]. These models can then

be used to predict and tune the properties of nanoparticles that are fabricated. Some have shaped and sculpted particles to be rod-like for particular extinction characteristics (Figure 6.4). Non-spherical nanorods exhibit different resonant peaks as a consequence of polarization-dependent illumination. For a non-spherical long rod illuminated with light parallel along its length, the region of largest enhancement is localized to the longitudinal ends of the structure [152].

6.3.3 Metallic Nanostructures

Metallic nanoparticles as separate elements are most commonly used in SERS. However, there are other ways to generate a LSP that can provide enhancement by patterning other plasmonic metals. Electron-beam lithographic patterning has existed for many years in the semiconductor industry. Taking advantage of the ability to draw nanometer-sized features and position them with nanometer-sized tolerance, it is possible to surround a small spot with separately patterned gold features (Figure 6.5). This is accomplished through a gold deposition, then e-beam patterning, and finally the use of a lift-off process or plasma etching of the gold layer to pattern the surface. Developing relief patterns into inverted nanodiscs, pyramids, and split-ring resonators created enhancement factors on the order of 10^5, with gaps on the order of 50 nm.

Optical-lithography patterned substrates such as Klarite® (Figure 6.6)

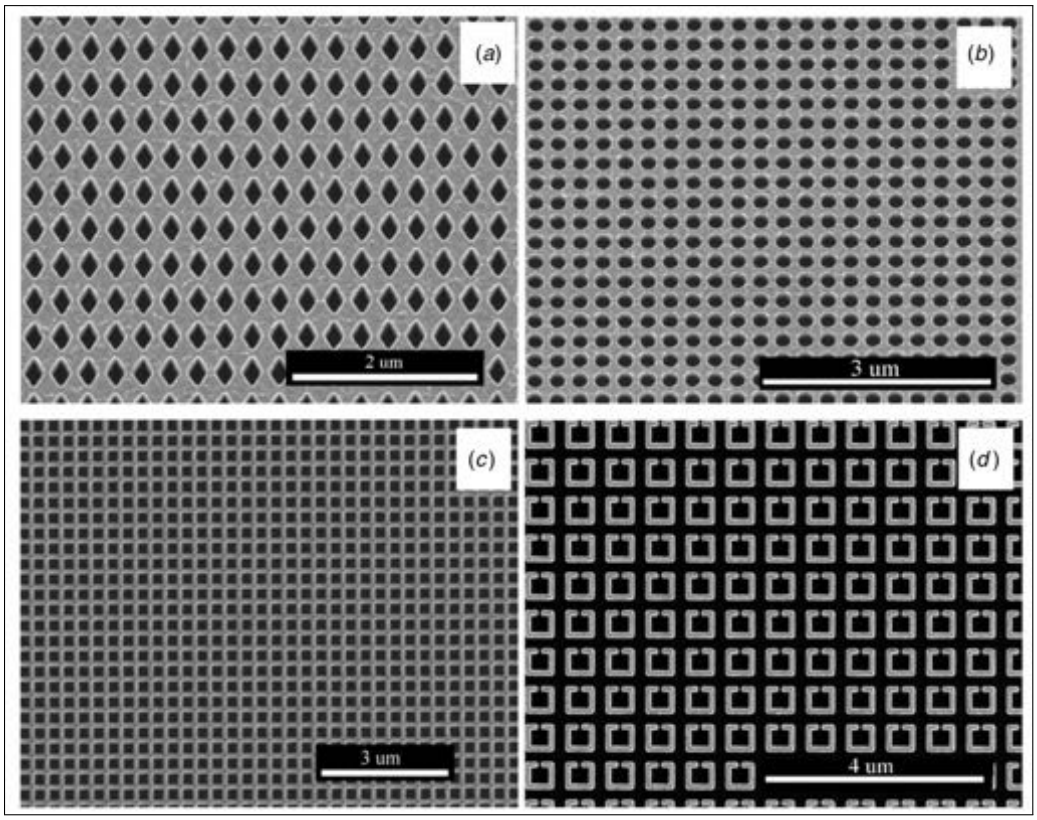

Figure 6.5: E-Beam Lithography Creates SERS-Active Structures. SEM images of gold nanostructures fabricated with e-beam lithography combined with plasma etching. (a) Pyramids, (b) discs, (c) cubes, and (d) split-ring resonators. Republished with permission of IOP Publishing, from Weisheng et al. [159], lightly adapted; permission conveyed through Copyright Clearance Center, Inc.

provide another way to impose structure on the plasmonic metal surface [160, 161]. By patterning square shaped wells onto a silicon wafer, a silicon etchant (EDP) that preferentially etches certain planes in the wafer produces pyramidal wells with a 54.7° angle of decline. A subsequent metal deposition produces grains of gold that line the sidewalls of the inverted pyramidal structure, where analyte molecules can be introduced across the

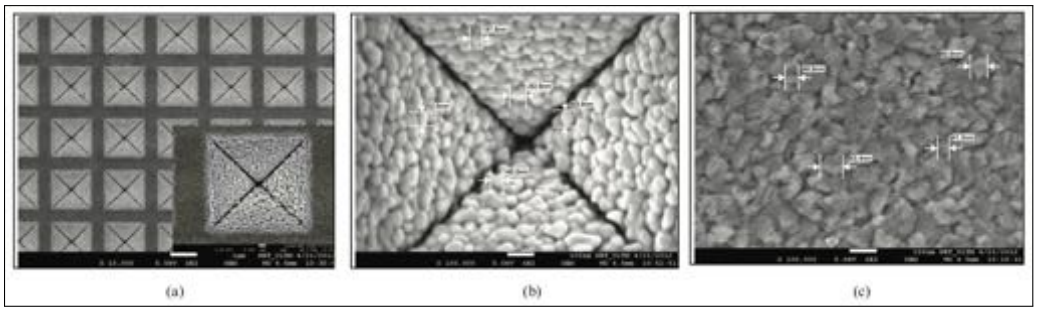

Figure 6.6: Klarite® Structure. a,b) FE-SEM images of Klarite® and c) Gold coated slide. Reprinted by permission from RightsLink Permissions Customer Service Centre GmbH: Elsevier Procedia Engineering, Radzol et al. [160], Copyright 2012.

population of wells. Simulated smooth thin films of gold suggest that the greatest enhancement of the film occurs at the apex of this structure [160], though this could still occur for the real particulate structures, as agglomerates would be in close proximity to each other at the apex. In contrast, a simple gold coated glass slide does not have this additional microstructure, even though individual grains of gold are similarly sized (Figure 6.6c). Adding the additional microstructure effectively expands the surface area of the Klarite® sensor for random AuNP enhancements, in addition to the enhancement at the bottom of the well.

Another strategy to create closely spaced plasmonic structures involves using another membrane as a template [162]. Anodized aluminum oxide (AAO) nanomembranes can have wall thicknesses less than 10 nm in width. This tiny gap between features is preserved during manufacturing a sensor; patterned gold and subsequent removal of the AAO template produces gold-capped nanopillars with an enhancement factor of 10^8

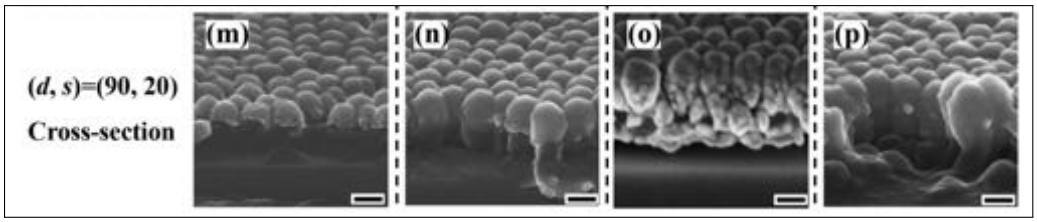

Figure 6.7: SERS Nanopillar Array. {d, s} represent the size and spacing distance of the nanopillar array. (m-p) Cross-sectional SEM images of gold/PC nanopillars arrays with {d, s} = {90, 20} nm, and the height (h) of the pillars are (m) 30 nm, (n) 60 nm, (o) 90 nm, (p) 120 nm, respectively. The scale bars represent 400 nm. Adapted with permission from Liu et al. [162], Creative Commons License (CC BY 4.0).

on average and 18% standard deviation. The semiregular spacing of the nanopillars is useful, but the heterogeneity of the supported particles is the primary driver of electromagnetic enhancement (Figure 6.7). Here, the maximum density of features is limited by the size and spacing of particles in a planar array.

6.4 Challenges in SERS Sensing

Making successful SERS measurements of chemical analytes requires some methodological consideration [144, 163].

- Substrates must be reproducible and robust over the course of measurement. Checking the substrate with a monitoring standard is essential.
- Analytes should adsorb on surfaces. This will provide enhancement closest to the surface.

- Ideally, analytes would have a higher SERS cross-section than other competing molecules in the observation volume.
- Measurement intensity must be low enough to prevent unwanted photochemical reactions that would contaminate the experiment.
- Quantitative measurements should be made by controlling for the number of active SERS sites as well as averaging over many events.

Detecting analytes depends on many different factors (Chapter 1), but having prior knowledge of molecules, surface chemistries, and measurement equipment is very important. The need for reproducibility and robustness is applicable to all sensing technologies, but in the case of SERS sensing, is especially appropriate as the mechanism for enhancement relies upon nanoscopic features that within even minute variations can cause vast differences in performance. Averaging many individual events together and monitoring the strength of the measurement with a standard enable some compensation for the large amount of variation that can occur with the substrate enhancement. Ideally, we would have well designed structures that reliably provided enhancement; the challenges relate to manufacturing these structures reliably to provide the same enhancement.

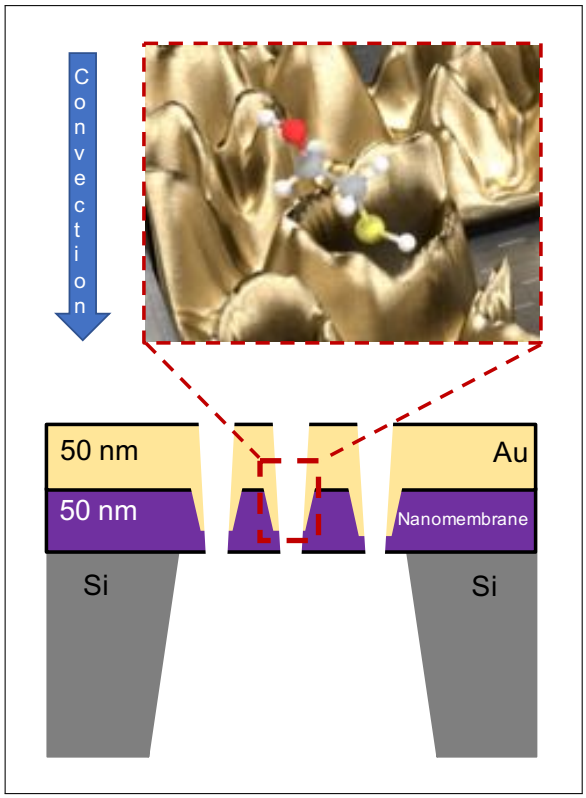

Figure 6.8: Theoretical Silicon-Based Nanomembrane SERS Sensor. Metallizing a silicon-based nanomembrane with a coinage metal (such as gold) would create an infilled structure. Molecules can flow through the sensor and interact with the sensing metal element on the nanopore walls.

6.5 Theoretical Silicon-Based Nanomembrane Structure

An improved SERS sensor could be made by using a flow-through detection strategy on a nanomembrane-based platform (Figure 6.8). SERS is a very sensitive technique with even single molecule detections being reported [164]. However, detection typically relies on molecules diffusing

from the bulk solution into a limited active region. With a flow-through sensor, low concentrations of analyte could be convected to the SERS active region along the walls/ends of the nanopore, increasing the probability of an analyte molecule encountering the active region. When considering material properties, the use of gold prevents many of the problems associated with silver coatings, such as oxidation which can change the shape of the substrate surface and poor biocompatibility, while still providing enhancement across visible wavelength illumination. The fabrication of the sensor relies on direct, line-of-sight fabrication techniques (sputtering or evaporation), which would create gold surfaces that taper into nanopores, while maintaining the nanomembrane porosity (Nanoporous Gold, npAu). The organization of the npAu structure would also be more homogeneous than a nanoparticle based detector due to the infilling process, creating contiguous films across the whole sensor, but variations would stem from the pore distribution of the underlying template, creating cones of gold with a distribution of enhancement properties. The template contiguity with out of plane features also obviates the need for the use of an adhesion layer, like titanium, to increase the mechanical stability of the sensing layer. Titanium has been shown to vastly decrease plasmonic behavior at thicknesses above 2 nm, due to broadening of Au resonances and impurities at the Ti/Au interface [165]. The silicon-based nanomembrane platform is an excellent choice to create this sensor because it is closely related to the material stack found on gold coated glass structures described above,

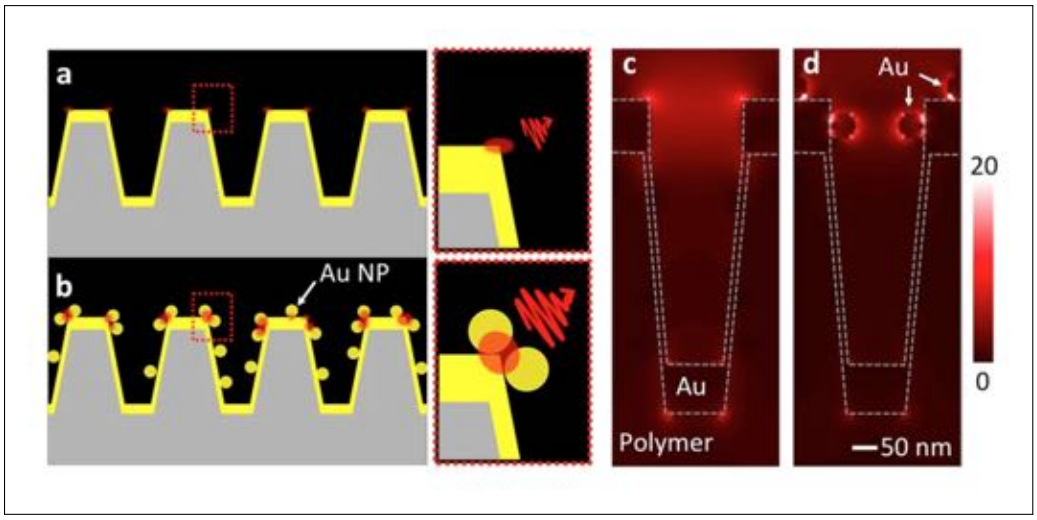

Figure 6.9: Example Au-NP-Pitted SERS Structure. (a,b) Schematic representation of the SERS enhancement mechanism on the nanoLCA (Nano-Lycurgus cup array) and the NP-nanoLCA. (b) Denser hot spot formation by self-assembling NPs on the colorimetric plasmonic substrate drives larger SERS EF. 3D-FDTD simulated electric field distributions (|E|) on (c) the nanoLCA and (d) the NP-nanoLCA show that the NPs attached in the nanocup effectively confine the electric field near the surface of the nanocup. Reprinted from Seo et al. [166], Creative Commons License (CC-BY-4.0).

while providing dense nanofeatures that provide many separate opportunities for enhancement.

Contrast this proposed structure with a recently published SERS substrate (Figure 6.9) [166]. This sensor is formed much like the nanopillar array in Figure 6.7, with imprint lithography forming the cup array, and deposition of 9 nm Ti and 90 nm Au to form the sensing structure. The design forms small divots approximately 100 nm across and 300-400 nm deep, which are metallized with the sensing film stack. To improve the enhancement, the authors link nanoparticles to the surface using cysteamine

(60-fold improvement over metal substrate alone). In essence, the authors have created a way to increase the surface area of the substrate, allowing more nanoparticles to form dimers, trimers, and aggregates that have stronger enhancements. In our structure (Figure 6.8), we do not have such long surfaces (50-100 nm vs 300-400 nm), but our density of nanopore features is $\sim$6-10x greater (60-100 pores/μm^2 vs 9 cups/μm^2) while maintaining flow-through introduction of reagent.

6.6 Fabrication of Nanoporous Au on Nanoporous MgF_2

6.6.1 Initial Attempts

The first attempts at making a SERS substrate with our nanomembrane materials was performed with leftover NPN and freestanding npMgF_2 membranes from a development effort in making porous, Raman-silent cell substrates (Chapter 5). We evaporated thin films of MgF_2 on top of a nanoporous silicon nitride template (NPN, SiMPore Inc.) with various pore distributions and then removed the template using reactive ion etch (Figure 6.10). While this method of production can be characterized as a simple etch-release process, it is not trivial to remove small amounts of silicon and maintain an intact free-standing nanomembrane. In order to complete the sensor, a single Au sputtering deposition (platen rotation, 15 mA) is performed to

reach a thickness target of 50 nm, as depicted in Figure 6.8. Additionally, the process can be adapted to produce thin freestanding versions of gold using NPN alone as a template (Figure 6.11), but these films are very weak and difficult to handle. Simple handling through the air can be enough to rupture these membranes.

By evaporating only a thin film, the npMgF_2 film maintains some porosity, though some is lost due to infilling of the nanopores resulting in conical features (Figure 6.12). These out-of-plane features appear to be substantial, on the order of 10-30 nm protrusions from the NPN/MgF_2 interface. The high selectivity of MgF_2 to the RIE etch means that these delicate features remain even after the template has been removed. Viewed *en face*, the npMgF_2 remains open, though narrowed due to the infill. An example quantification of this effect is realized by mapping and counting pores in SEM micrographs [10], showing that the narrowing can be a substantial shift (Figure 6.12). In this case, the average distribution of the NPN template was 35 nm, and the fabricated npMgF_2 distribution was 25 nm, a change of more than 25%. This calculation is performed for a different set of NPN/npMgF_2 than the one that is shown in Figure 6.12. The nanoscale npMgF_2 structure will ultimately govern the placement of gold within the cone.

To evaluate the SERS response of our structures, we chose to incubate differently manufactured substrates with a reporter molecule (thiophenol) and record its spectrum. The choice of thiophenol as a reporter molecule

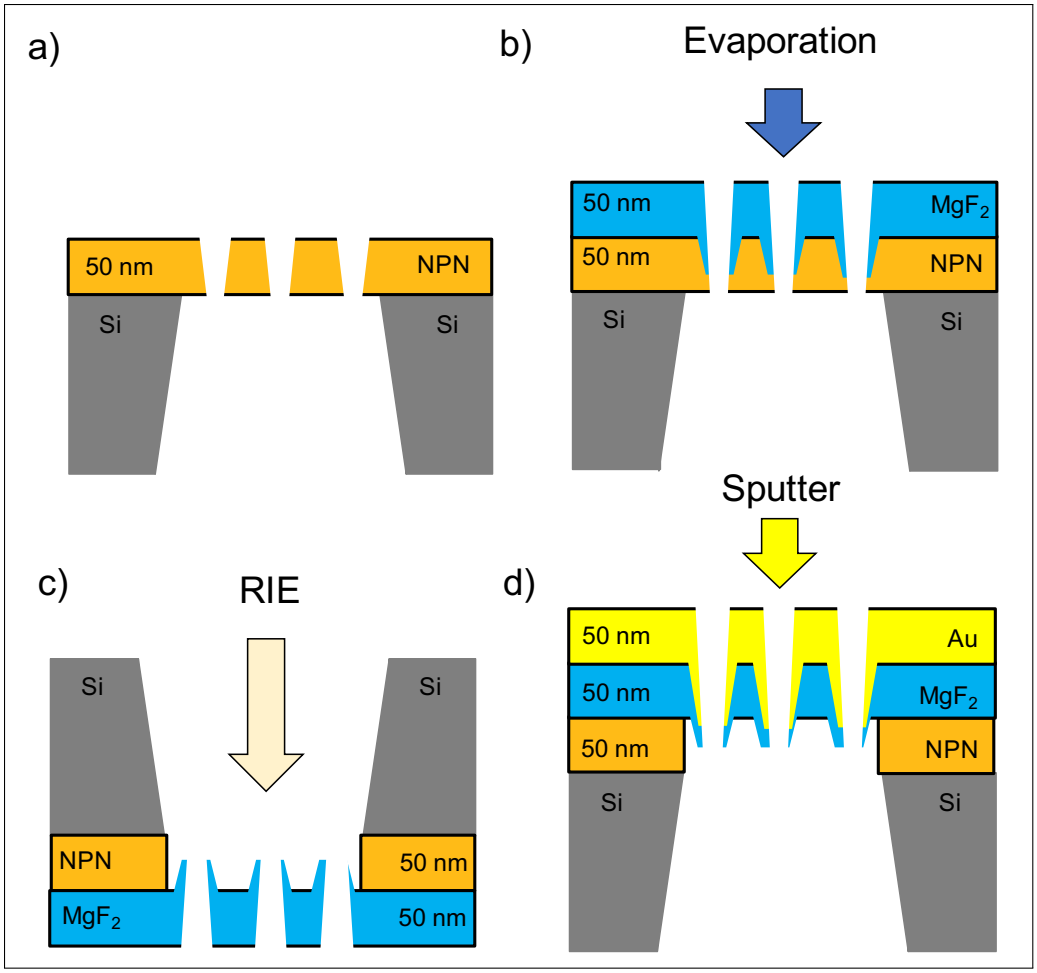

Figure 6.10: npAu/npMgF$_2$ First Fabrication Flow. MgF$_2$ relief pattern transfer, with cartoon cross-sections of nanoporous films (not to scale). Beginning with a freestanding film of nanoporous silicon nitride (NPN) (a), MgF$_2$ is evaporated onto the substrate (50 nm, 0.1-0.3 nm/sec, 250°C, Platen Rotation), coating the porous substrate, resulting in a hybrid material, (b). The film stack is then inverted and purified using RIE (90% CHF$_3$, 10% Oxygen, 75 mTorr, 100 W), releasing a freestanding nanoporous film of MgF$_2$ (c). This general strategy can be applied to other materials, such as gold or platinum deposited with sputtering. (d) Au is sputtered on the film stack (15-30 mA, 50-200 mTorr, 0.1 nm/sec, Platen Rotation) to complete the sensor

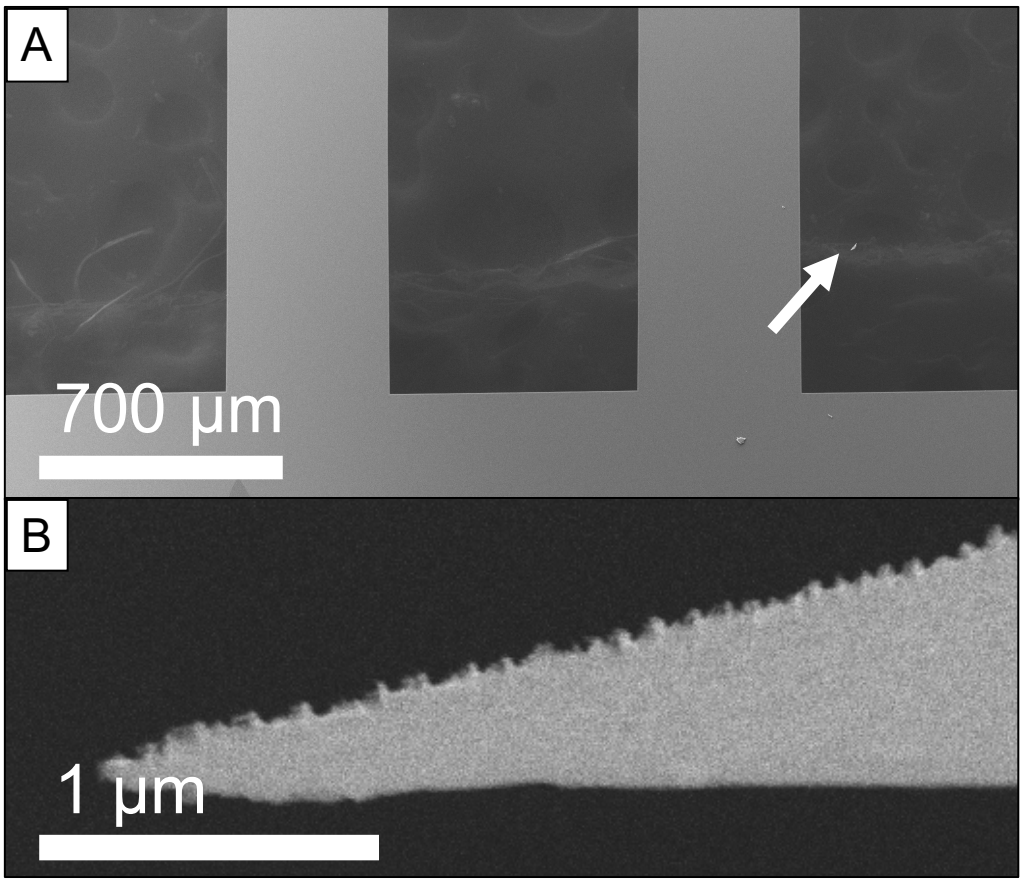

Figure 6.11: Freestanding npAu SEM Images. (A) Aerial image reveals that the npAu membrane is porous enough to image carbon tape structures underneath the membrane area. Arrow indicates a particle on the npAu membrane. (B) npAu cross-section shows fabricated out-of-plane features.

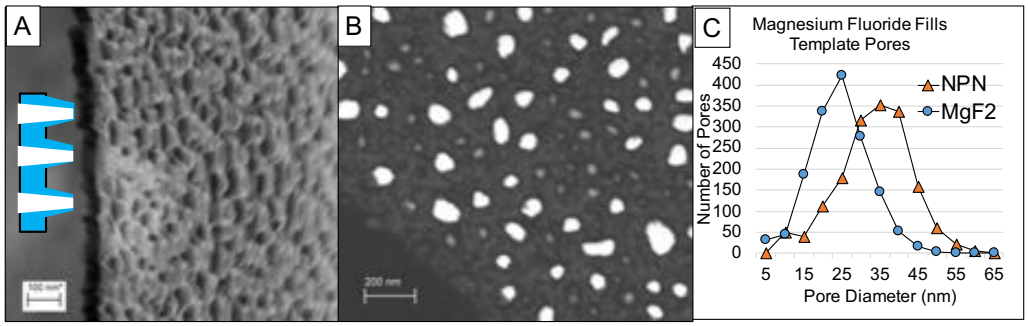

Figure 6.12: npMgF$_2$ EM Cross-section and Aerial Image. (A) SEM cross-section of a 50 nm MgF$_2$ freestanding nanomembranes reveals conical 'volcano' features, resultant from pore infilling during the evaporation process. (B) Representative STEM image of npMgF$_2$ from a different NPN template depicts open nanopores (white ovals, large pores). (C) Example pore distribution histogram of fabricated nanoporous MgF$_2$ and NPN template. Pore infilling of the NPN produces a smaller npMgF$_2$ pore distribution, for all substrate pore sizes. (B), (C) reproduced from Figure 5.2 for convenience.

is convenient as the thiol group binds well to gold, forming dense self-assembled monolayers that experience chemical enhancement through electronic coupling to the surface. Increasing the local concentration of molecule in the 'hotspots' of the enhancement substrate is useful to maximize the signal observed from these molecules, however, it is not totally necessary; molecules can move in and out of the enhancement region and be detected. A flow-through sensor created from this structure must effectively balance the flow rate through the membrane and the dwell time around the enhancement hotspots. As a matter of practicality, the self assembled monolayers make it easier to observe consistent results through the defined orientation of the molecules caused by steric packing. Example spectra for this molecule are seen in Figure 6.13, where different sub-

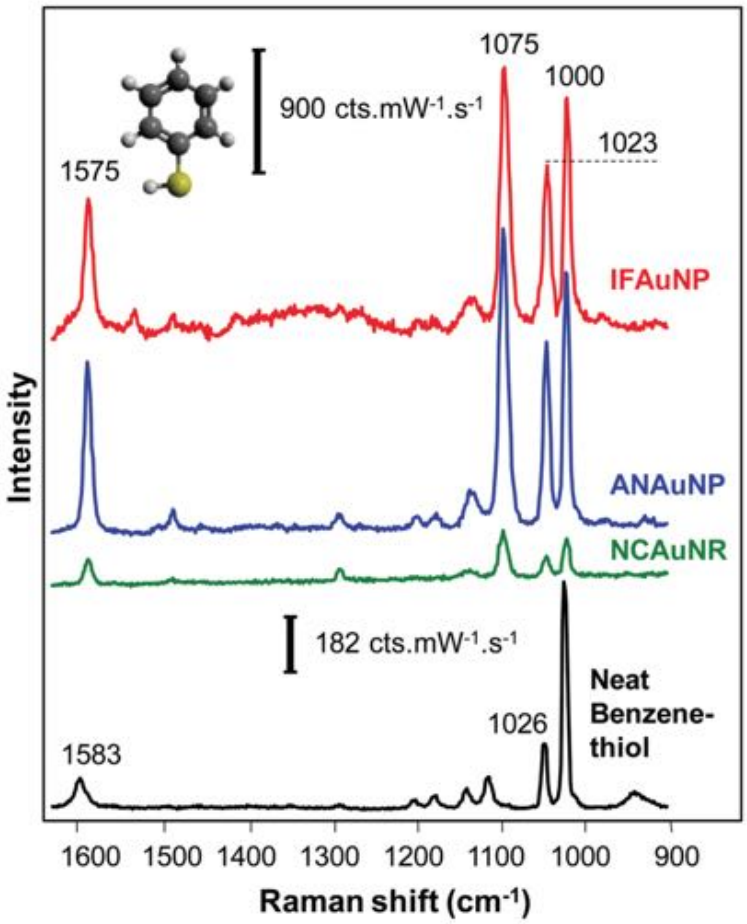

Figure 6.13: Characteristic Thiophenol Raman Peaks. SERS spectra of benzenethiol (inset) acquired on IFAuNP (red), ANAuNP (blue), and NCAuNR (green) 3D SERS substrates. λ = 785 nm, P = 103 μW, and T = 10 s. Normal Raman spectrum of neat benzenethiol obtained at λ = 785 nm, P = 2.5 mW, and T = 1 s. Adapted from Kurouski et al. [167] with permission of The Royal Society of Chemistry.

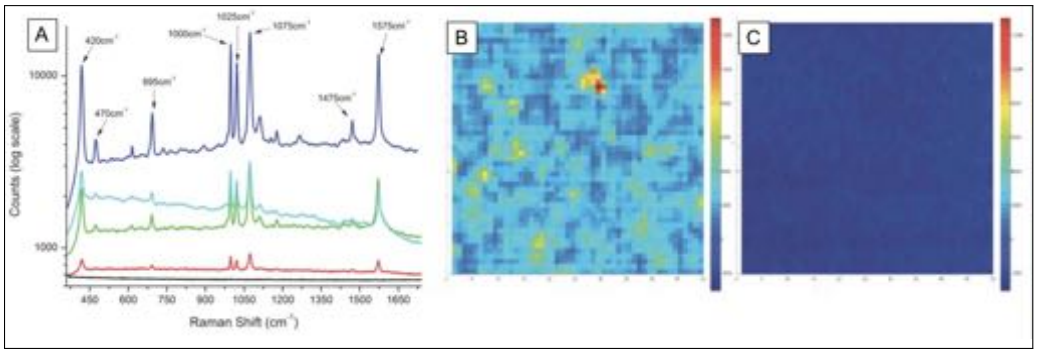

Figure 6.14: npMgF$_2$/npAu Initial SERS Performance Comparison. A) Raman (SERS) spectra of benzenethiol absorbed on different substrates, imaged for all but bare gold at 10 s integration time and 2 mW laser power. Black: bare gold. Red: npAu upper side; Green: npAu, template side. Cyan: Klarite® substrate. Blue: npAu/npMgF$_2$, measured from the template side. The bare gold spectrum was taken with 150 mW of laser power at the sample and 20 s integration time. Arrows represent typical benzenethiol Raman vibrational frequencies. B) SERS enhancement uniformity of benzenethiol 1075 cm^{-1} peak on Klarite® substrate mapped at 1 μm/step, 50x50 pixels. C) SERS enhancement uniformity of npAu/npMgF$_2$, mapped at the same scale, providing much more even enhancement across the entire field of view. Adapted from Pascut et al. [168].

strates were incubated with thiophenol (iFyber LLC = IFAuNP, AnSERS = ANAuNP, Non-commercial nanorods = NCAuNR). Characteristic peaks at 1575, 1075, 1023, and 1000 cm^{-1} are observed on the SERS substrates.

Many gold sensing layers were created on npMgF$_2$ and NPN substrates with five 0.1 x 3 mm windows, including freestanding gold by itself (50 nm, npAu), as described in Figure 6.12. To test the SERS response of freestanding npAu and npAu/npMgF$_2$ nanomembranes, thiophenol was adsorbed onto a number of different substrates and measured using a confocal Raman microspectrometer (model 77200 Oriel, 1000 lines/mm grating, cooled CCD detector). Substrates were incubated with 4 mM thiophenol at room temperature for 1 hr to saturate the surface, then rinsed

thoroughly with absolute ethanol. The illumination (2 mW, λ = 725 nm, Ti:Sapphire laser, Spectra Physics) was directed onto the sample using a water-immersion objective (63x, numerical aperture 1.0).

Figure 6.14 summarizes the chief results of this process. A gold-coated coverslide showed no appreciable spectral peaks. The freestanding npAu measured on the flat surface (away from the nanovolcanoes, Red) performed considerably worse than the measurement on the nanovolcanoes (Green). Compared to a commercially available substrate (Klarite®, Cyan), the spectra for thiophenol on npAu is similar. However, the best performance is measured with the hybrid npAu/npMgF_2 film stack on the trench surface with the out of plane features. Characteristic spectral peaks of thiophenol (1000, 1025, 1075, 1575 cm^{-1}) are taller than that of the Klarite® sensor, as well as producing some peaks that aren't obvious on the commercial substrate (470, 695, 1475 cm^{-1}), providing a 7-fold relative improvement.

Similarly, if spectra are gathered across the substrate surface, a map of their enhancement uniformity can be gathered. Figure 6.14B shows the enhancement uniformity of the 1075 cm^{-1} peak on the Klarite® substrate with a few spots of larger enhancement that provide much more signal compared to the rest of the mapped area. In contrast, Figure 6.14C shows the npAu/npMgF_2 is much more uniform, lacking any appreciable hot spots (about 10x more uniform than the Klarite® sensor, calculated from the standard deviation of 100 x 100 spectra). This would lead to greater utility, by

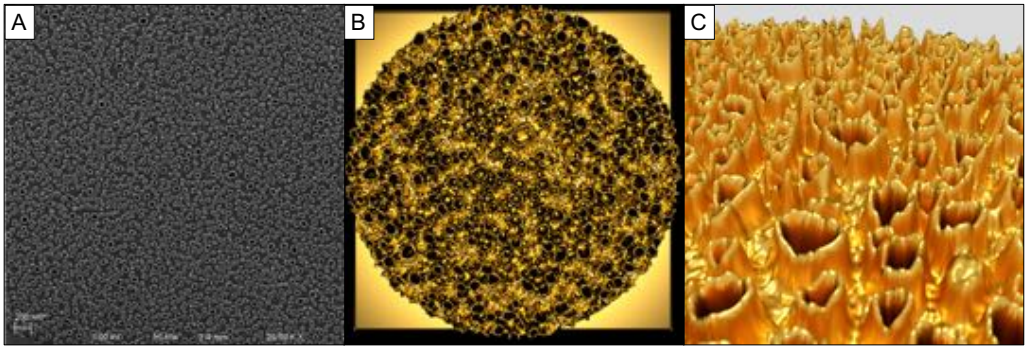

Figure 6.15: Rendered Height Maps of npAu Surface. (a) SEM aerial image of npAu on NPN template. The white rings around nanopores are gold coatings on the sidewalls of the template. (b) Intensity-height mapping of (a) produces 3d structure. There are hundreds of nanofeatures within a 1 μm confocal spot that can contribute to a SERS effect. (c) Cross-sectional view of (b). Out-of-plane gold nanocones are thought to conformally line the surface of npMgF_2 nanovolcanoes.

being able to reproduce measurements faithfully without regard to where the measurement is taking place on the sensor, directly addressing the need for invariant substrates mentioned in Section 6.4.

We hypothesized that the large density of features inside a single measurement spot is essential to creating this uniformity. Figure 6.15 depicts a simple height mapping of nanofeatures based on the intensity profile from SEM images gathered of the out of plane features. There is a distribution of npMgF_2 nanovolcano sizes and shapes (Figure 6.12) that provides a gold attachment surface, which should conformally infill these surfaces. The primary layers of gold coating should attach and migrate along these sidewalls, eventually coalescing into thin films. As the fabrication process continues, these thin films will taper into the nanovolcanoes (Figure 6.15B), providing sharp discontinuities and potential regions of electromagnetic en-

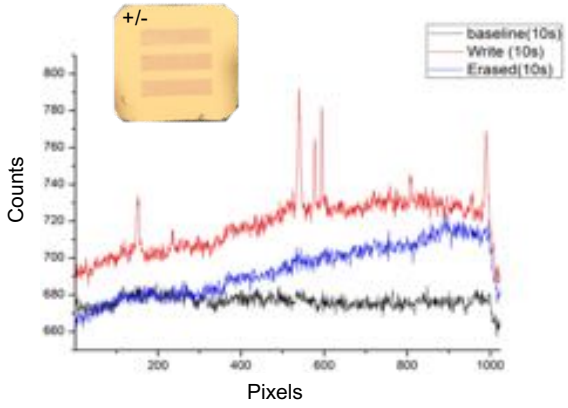

Figure 6.16: Electrochemical npAu Raman Measurements of Thiophenol. Pixel number correlates the Raman shift, 10 sec interrogation time. At baseline (black line), the substrate experiences an applied voltage to attract thiophenol to the surface (red line). The voltage is then reversed, which removes the thiophenol from the surface (blue line). Inset: A gold coated npAu/npMgF$_2$ chip.

hancement.

The contiguity of the sensing structure also permits electrochemical modification of the sensor surface. Figure 6.16 demonstrates the ability of the sensor to influence the binding of the sensing molecule, thiophenol. The presence of characteristic thiophenol peaks are observed as an electric potential is applied to the substrate on the bulk part of the chip, away from the sensing membrane surface. The contiguity of the npAu film allows molecules to be attracted into the nanomembrane area, which are then detected. When the potential is reversed, the characteristic thiophenol peaks vanish.

This initial set of results was very encouraging. The hybrid npAu/npMgF$_2$ structure outperforms the commercially available substrate in terms of uni-

formity, while maintaining the ability to be manufactured in high volume using standard semiconductor fabrication techniques. However, the primary flaw from this fabrication process is that the total yield of fabricated npAu/npMgF$_2$ chips was less than 10%. Most of the loss occurred during the freestanding npMgF$_2$ fabrication step. Chips with multiple nanomembrane windows often had one or two survive, but few chips had all windows survive. Free, broken curls of membrane are often observed, indicating that the stress is very high in the fabricated film. Other attempts to improve the yield of the npMgF$_2$ process were then considered, by evaluating mechanical strength and individual process yields.

6.6.2 Annealed Films

Figure 6.17 describes a fabrication flow that templates a MgF$_2$ thin film onto a NPN substrate utilizing an annealing process. We hope to improve the mechanical strength of the first process flow by annealing the film stack after a lower temperature evaporation, allowing defects or cracks that form in the npMgF$_2$ to be remediated. A similar RIE step is then used again to remove the NPN template, leaving the freestanding film. Figure 6.18 depicts the features of a thin npMgF$_2$ fabricated in this way, revealing that the temperature of the annealing step can influence the underlying structure, causing fissures if the temperature is too high. Both films maintain the nanoporosity of the template, however, the fissures seem to propagate

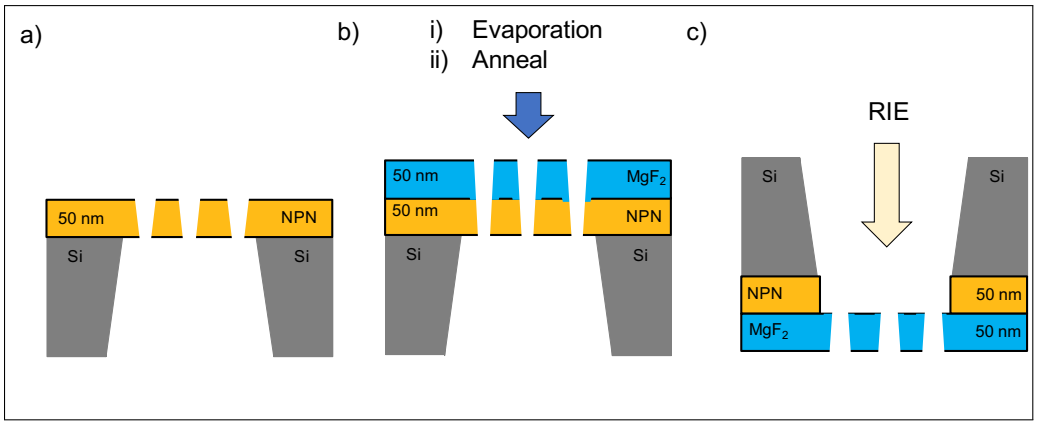

Figure 6.17: Annealed npMgF$_2$ Fabrication. (a)-(c) MgF$_2$ relief pattern transfer, with cartoon cross-sections of nanoporous films (not to scale). Beginning with a freestanding film of nanoporous silicon nitride (NPN) (a), MgF$_2$ is evaporated onto the substrate (50 nm, 0.1-0.3 nm/sec, 20°C, Platen Rotation), coating the porous substrate, resulting in a hybrid material. (b)-(c) The substrate is annealed in an Ar ambient for 2 hrs at 600°C, then inverted and purified using RIE (90% CHF$_3$, 10% Oxygen, 75 mTorr, 100 W), releasing a freestanding nanoporous film of MgF$_2$ (50 nm thick). The out of plane volcano protrusions are resorbed into the npMgF$_2$ film during the annealing step. Data is repeated here for convenience (Figure 5.2).

from pore to pore. A cross-section of the image shows that the nanovolcano features of the npMgF$_2$ are absent, resorbed during the annealing process. This was unexpected at the time, though in retrospect, not difficult to imagine. The npMgF$_2$ nanovolcanoes, while easy to image, contain only a small percentage of the mass of the npMgF$_2$ thin film and would most easily be absorbed. The mechanics at this scale are not heavily influenced by gravity, rather, the surface tension of the hot film is a very likely mechanism for resorption. The lack of out-of-plane features significantly reduces the amount of internal area (20-40%) for gold attachment.

To evaluate the strength of the annealed fabrication flow, NPN mem-

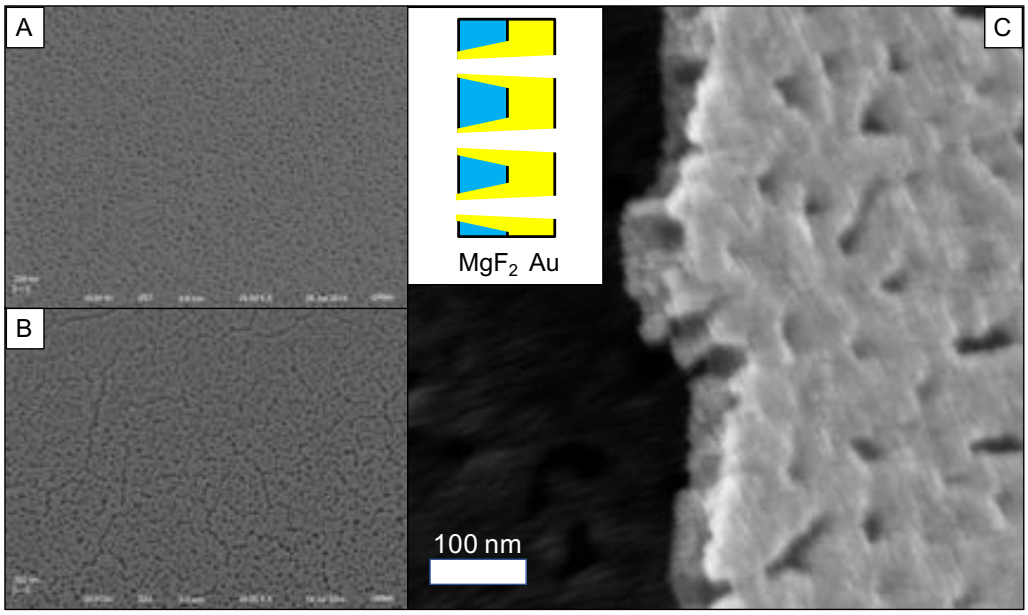

Figure 6.18: Annealed npMgF$_2$ Structure. (A) 600°C annealing promotes contiguous npMgF$_2$ thin film formation. (B) 700°C annealing leaves microfissures in the fabricated npMgF$_2$ film. (C) SEM cross-section of the material coated with a thin layer of gold shows no nanovolcano features. The inset depicts the infilling of the Au film on the npMgF$_2$.

branes of various square window sizes were converted into npMgF$_2$ using the process outlined in Figure 6.17. These membranes were manufactured from 2 NPN wafers with similar pore sizes and porosities (34 nm, 14% vs. 37 nm, 15%) to control for any effects of the underlying pore distributions on mechanical strength. Subsequently, Figure 6.19 characterizes the mechanical performance and yield of the fabricated npMgF$_2$ films. By tracking the numbers of chips that survive through each stage fabrication process, we can see that the etching step causes most of the loss. Overall, 85% of chips survived the annealing process, and 34% of chips survived the full an-

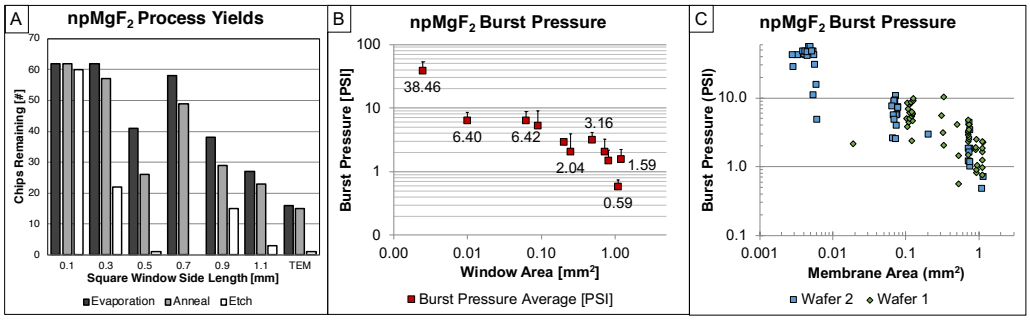

Figure 6.19: Annealed npMgF$_2$ Process Yield and Burst Pressure Data. (A) The etch process is the primary driver of yield loss. TEM chips have four 0.5 x 0.5 mm square windows. (B) Burst pressures were collected using controlled flows of nitrogen. Error bars are 1 standard deviation. Certain window sizes have labeled burst pressures for clarity. (C) npMgF$_2$ windows were fabricated on two wafers with similar pore characteristics, with data jittered to show similar distributions. Data is repeated here for convenience (Table 5.1).

nealing/etching process. The mechanical strength of surviving nanomembranes was evaluated by a burst pressure test. Nitrogen gas was flowed through the porous films in a fixed jig while recording the pressure in the gas line. As the active area of the npMgF$_2$ nanomembrane increases, the strength decreases. Membranes that have burst pressures greater than 5 PSI are generally suitable to use in liquid [4], which would mean npMgF$_2$ window sizes should be limited to 100 μm squares in production. An alternative fabrication flow would be to deposit gold on the evaporated npMgF$_2$ layer before removing the NPN template layer (Figure 6.10d before Figure 6.10b). Adding Au to the nascent film stack could also improve it's mechanical strength, but the gold layer itself is not particularly strong and this has yet to be tested. This would also expose the gold sensing layer to the same etch that is found in the freestanding npAu nanomembrane,

potentially modifying the surface further.

6.6.3 SERS Loss on Annealed Films

While the overall yield of these sensors was much improved compared to the first attempts to manufacture the film stack (34% vs sub-10%), when examined for SERS activity using a thiophenol exposure as in Figure 6.14A, the films were very poorly responsive, producing spectra like the freestanding npAu substrate. It was thought that the nanostructure of the fabricated npMgF_2 was particularly important, specifically the out-of-plane nanovolcano features that would constrict the gold contained within them, and the annealing process removes these features. However, reverting to the first process that produced strong SERS responses (Figure 6.10) on a set of newer NPN materials did not recover the previously strong SERS signal observed. As the methods for evaporation and etching to produce the freestanding npMgF_2 had not changed, this warranted further investigation into the properties of the NPN template.

6.7 Structural Characterization of Fabricated npAu/npMgF$_2$

6.7.1 Surface Characterization

Even though silicon-based nanomembrane materials may have similar physical properties (on the scale of 10 nm), we have observed that their effectiveness as SERS substrates can vary considerably. Each set of nanomembranes that are fabricated from a single silicon wafer are numbered and designated as chips and material from that wafer (Wafer #, Material). Our typical characterization of silicon-based nanomembranes relies on SEM/STEM and measuring the aerial image of the pores directly. Figure 6.20 describes the use of this technique on 1085 NPN, which was one of the first substrates to be fabricated into npAu/npMgF$_2$. Open pores are imaged as white ovals, which after some light image processing via background correction and thresholding are measured [10]. Through this technique, we lose much of the surface information about the silicon-based nanomembrane, such as the depth profile of the nanopores and the roughness of the inner pore walls. In the current model, we assume the aerial image of the thresholded nanopores is propagated with perfect fidelity through the full thickness of the nanomembrane. We need to better understand the sources of variation in our fabrication, and the surfaces of all the films in this process are most likely important to the SERS effectiveness of the re-

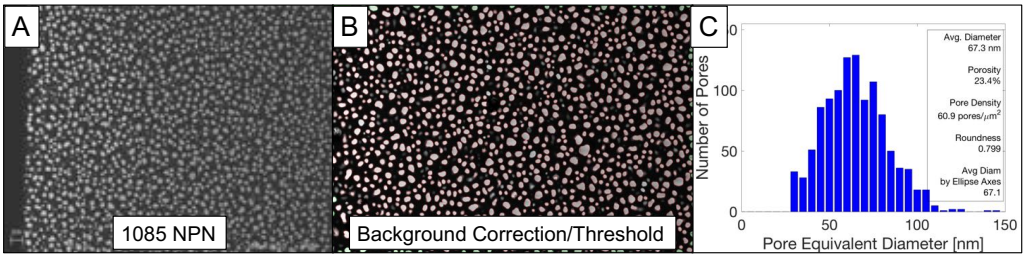

Figure 6.20: SEM and Pore Analysis of 1085 NPN Substrate. (A) STEM image of 1085 NPN. (B) Thresholded and outlined pores contribute to the pore histogram (C). Green square indicates the size of the background correction.

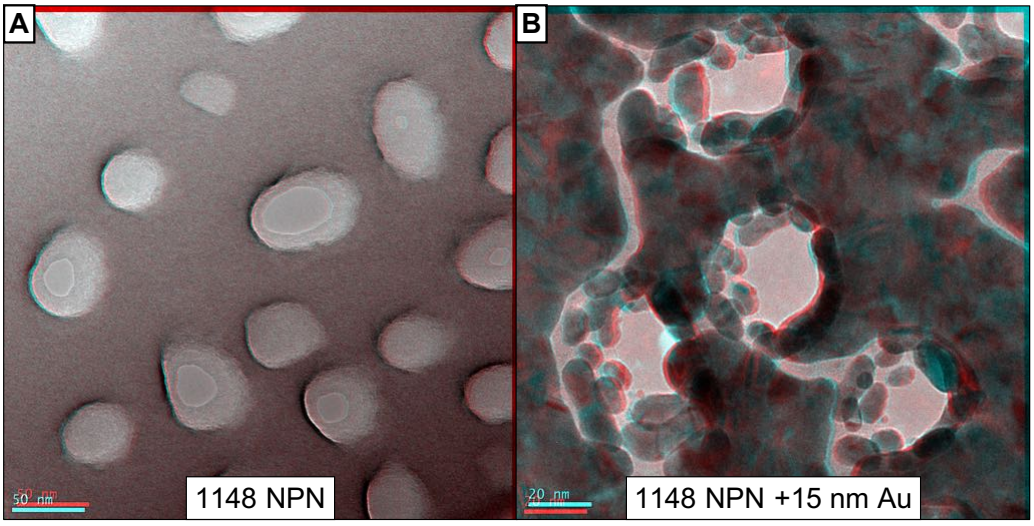

Figure 6.21: NPN Anaglyph with +15 nm Au. (A) Native 1148 NPN anaglyph. (B) 1148 NPN metallized with +15 nm Au anaglyph. Each membrane was imaged from -14° to +14°, in 2° increments. The anaglyph was formed by taking the +14° and +10° images, aligning them, and assigning them to red and cyan color channels. Viewed with red/cyan glasses, these images can provide the illusion of depth.

sultant structure. To better assess the quality of starting NPN templates, over 20 different production runs of NPN were imaged using TEM. A summary of these techniques and results is found in Chapter 4.4.

Given the infilled characteristic of the npMgF_2 templated from NPN, it is desirable to know how gold is localized to these surfaces when it is introduced. Using the reconstructive techniques described in Chapter 4, the nanofeatures imaged in Figure 6.21, display tiny Au nanoparticles (black ovals) coating the walls of a NPN nanopore (Wafer 1148, 50 nm thick, 33.5 nm average pore diameter, 6.3% porosity). It is clear that these particles appear at different heights within the nanopore. The major limitation of these images is that the technique requires electron transmissive samples, that is, samples that are thin enough to be observed with the TEM. Gold is very electron dense, so even small amounts of gold are difficult to image with this technique. Thicker amounts of gold in a plasmonic region of interest are opaque using TEM (above $\sim$20 nm). Thicker gold films could be reconstructed using this tomogram reconstruction technique with SEM, but the resolution is worse and cannot capture fine details (small gaps and fissures) of the film inside the nanopores.

Assigning segments to different heights in the stack and knowing the physical dimension of the NPN thickness allows us to characterize the size and location of different nanoparticles in the pore. The STL file is then imported into free animation and modeling software (Blender 2.79c, `https://www.blender.org/`) for visualization purposes. Examining the Blender rendered nanoparticle contours reveals a number of interesting things about the structure of gold inside the NPN nanopore. A single 15 nm thick Au layer deposition is not enough to form a stable continuous film, however, there

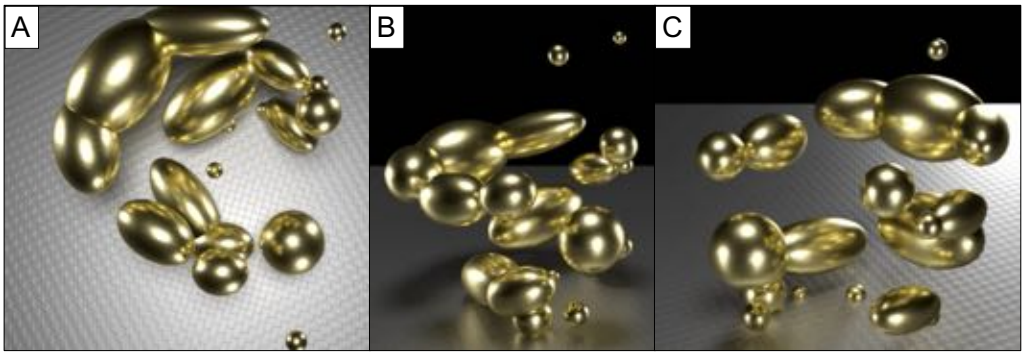

Figure 6.22: Reconstructed AuNPs inside NPN nanopores. 1148 NPN was metallized with +15 nm Au, then AuNPs were imaged, reconstructed, segmented and visualized using the method described in Chapter 4. (a) Aerial image as seen in anaglyph. (b) Cross-sectional view. (c) Stratified layers of gold form inside the nanopore.

appear to be banded patterns of deposition along the length of the pore, indicating that there were contractions of a continuous film into these particles, during the nucleation phase of thin film growth. The nanoparticles are not necessarily spherical, and some have complicated oblate shapes. In the context of particle plasmons, the shape of the nanoparticle will directly change it's absorption characteristic [152]. In this reconstruction, spherical nanoparticle diameters range between 5-25 nm, while the more complicated oblate rods are 40-70 nm long, producing aspect ratios from 2-4. This would lead to an extinction spectra that is maximized anywhere from 650-900 nm, along the longitudinal axis of the rods. However, this view is very simplistic and does not account for the positioning of the gold inside the pores, nor the "crescent-moon" shape of gold following the contours of the nanopore. Closely-spaced gold nanorods in parallel have already

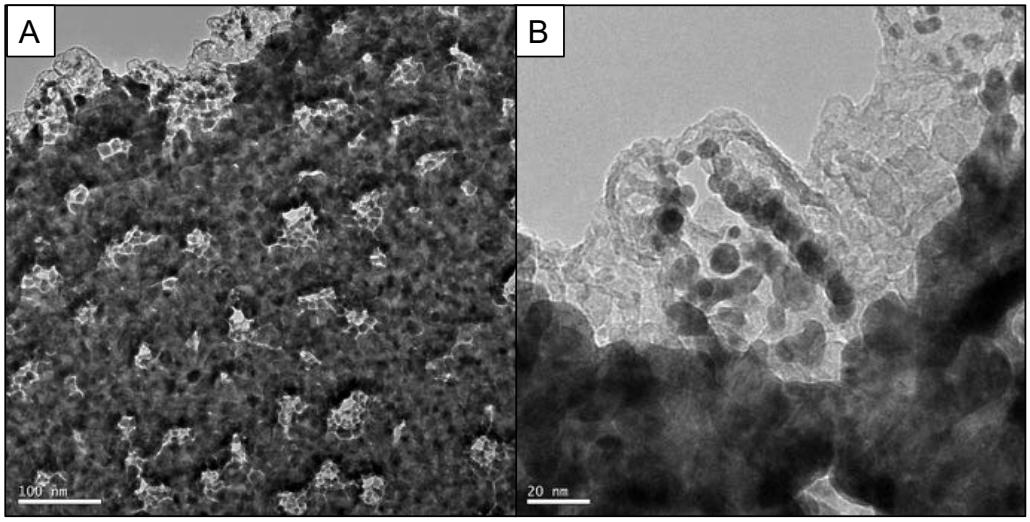

Figure 6.23: Gold Nanoparticles Fill npMgF$_2$ Nanovolcanoes. A) $\sim$25 nm of gold was sputtered onto a 50 nm thick npMgF$_2$ substrate (fabricated from 1236 NPN), then broken and imaged using TEM. The viewing angle is approximately 45°. The bulk film is too opaque to image properly, but the sidewalls of the nanovolcanoes contain dense nanoparticle features. B) Even at thinly deposited thicknesses of gold, nanoparticles infill along the whole sidewall of the nanovolcano.

shown to influence the extinction characteristic of neighboring nanorods [169]. A 3D model of the electric field around these nanostructures in tight confining nanopores is necessary to make better predictions.

Figure 6.23 depicts a npMgF$_2$ substrate coated with gold. This material was templated from 1236 NPN, creating a membrane with 25.6 nm average pore diameter and 5.6% porosity. The npAu features inside the nanopores are thought to control the SERS behavior of the sensor. A target of 50 nm gold film is too dense to image properly, but some methodological changes can be used to image thinner gold films. The line-of-sight fabrication of the gold film propagates into the pores and coats the sidewalls of the

nanopores, providing another mechanism for adjusting the npAu surface characteristic. By sectioning the npAu/npMgF_2 sensor and observing the sidewalls of the nanopores, some structure can still be observed even with $\sim$25 nm Au thickness. As more gold is added, the separate nanoparticles observed in Figure 6.21 tend to merge and become more consistent. There appear to be small gaps between particles at the end of these nanovolcanoes, much less than 10 nm apart, which would be potential hot spots for electromagnetic enhancement. If the substrates in Figure 6.14 had small nanoparticle tips at the end of the volcano in a 'halo-like' structure (Figure 6.22), it would provide many opportunities for enhancement in each nanopore. In Figure 6.23, there are 30-60 particles per nanopore, and at least that many gaps between them. Combined with the density of features in a resolved confocal spot ($\sim$1 μm diameter, 1236 npMgF_2 = 70 pores/μm^2, 55 features), there are over 1650-3300 features in a single measurement that could contribute to a measurement. This feature density could explain the uniformity of measurement observed on these types of substrates.

As there are many nanofeatures integrated in a single SERS measurement, the gold inside the pores may not be the only active element on the npMgF_2 sensor. Therefore, it is useful to consider the overall roughness of the top surface parts of the membrane. To measure the surface roughness, we use Atomic Force Microscopy (AFM) which uses a small cantilever to track position near surfaces. The samples were affixed to the AFM holder with nail polish, and then immersed in DI water. Small scans were made on

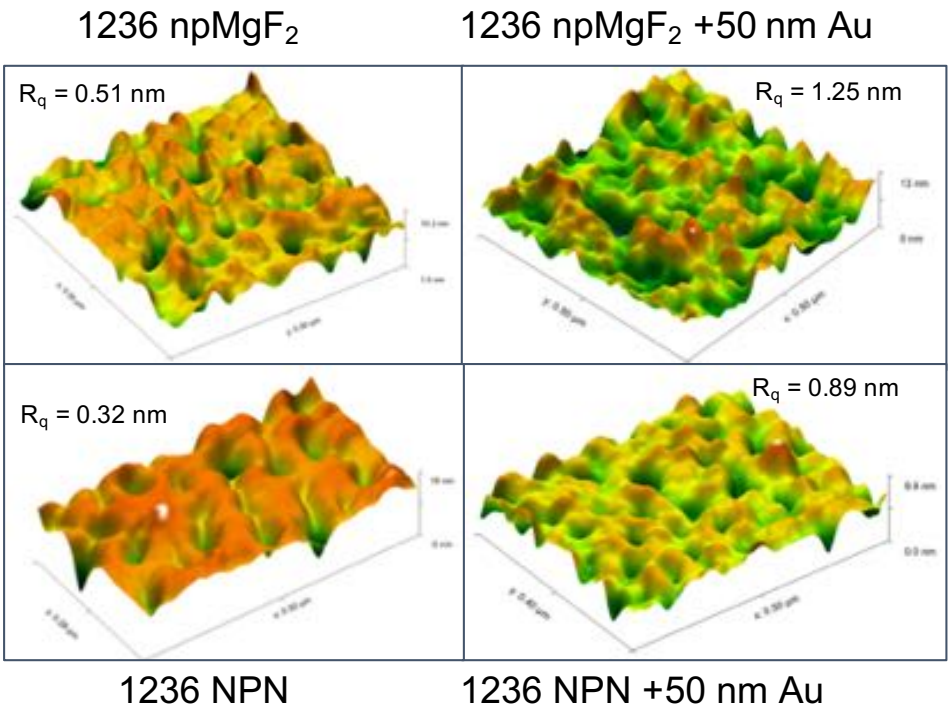

Figure 6.24: AFM Roughness Scans of SERS Substrates.

the chip on the bulk part of the chip near the window; the thin windows were too fragile to place into contact without tearing. R_q values describe the root mean square average of height deviation taken from the mean image data plane. In these images, the roughness values were calculated from areas that did not include any nanopores. The depth of the nanopore would improperly contribute to height deviations of the thin films we measure.

Figure 6.24 describes the surface roughness of the npAu/npMgF$_2$ sensor at various stages of fabrication. As the starting substrate is relatively smooth (1236 NPN), adding subsequent layers makes the structure rougher.

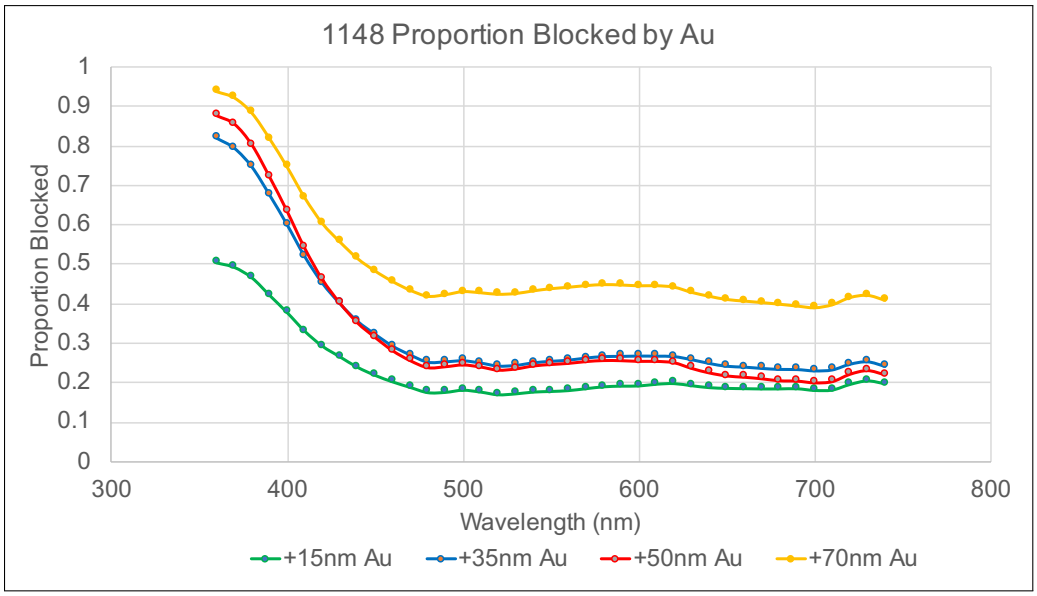

Figure 6.25: Light Blockage Contribution of npAu/NPN SERS Substrate for Various Thicknesses of Au.

The roughest surface is the final npAu/npMgF$_2$ film stack. Comparing the two SERS active conditions (NPN+Au R_q = 0.89 nm, npMgF$_2$+Au R_q = 1.25 nm), both surfaces are rougher than what would be expected from the native substrates alone (NPN R_q = 0.32 nm, npMgF$_2$ R_q = 0.51 nm). However, these values are an 1-2 orders of magnitude less than the roughened metal surfaces used in SERS detection [148, 150, 170], indicating that the features within the nanopores are probably responsible for electromagnetic enhancement, not any roughness on the spans in between the pores.

6.7.2 npAu Film Absorbance

Evaluating the absorbance characteristics of the npAu film would provide useful information about the resonances over the visible spectrum where we working. Some work has previously been performed examining the transmittance properties of contiguous metallized silicon based nanomembranes in the context of SPR, where both the template and ambient medium affected the transmissive responses (Shome [24], Chapter 3). Transmission minima were calculated for single 15 nm or 30 nm nanoholes on pnc-Si around λ = 700 nm, though the effects of having real pore distributions minimized the magnitude of the peak. Other simulated stacks in Shome [24] featuring a 30 nm nanopore in a 30 nm silicon film sandwiched between two 15 nm gold films produced large extinctions around λ = 800 nm, however, this would vary substantially by changing the geometries and thicknesses of these features.

In this work, NPN templates (Wafer 1148) were sputtered with varying amounts of gold (15 mA, 100 mTorr) and evaluated using a UV-Visible integrating sphere spectrophotometer (Konica Minolta, CM-3700A, Xe pulse lamp) in air. An aperture was fabricated to hold 5.4 x 5.4 mm silicon chips in the tool. After initial tool calibration (0% and 100%), baseline transmission measurements of broken windows were made, providing the actual nanomembrane aperture. Then measurements of bare NPN substrates were made, providing the base film stack, and then transmission measure-

ments with intact Au films were gathered. Figure 6.25 depicts the amount of light blocked by different gold film thicknesses. There is a small local peak observed for all gold thicknesses at $\sim$730 nm, which is similar to the prediction found in Shome [24], however, the substrate is not the same as what was previously simulated, using NPN instead of silicon. All of the curves have similar shapes, but as the film thickness increases, the relative proportion of the light blocked by the gold film compared to the template increases.

6.8 Effects of Gold and MgF_2 Thickness on SERS Performance

6.8.1 Experimental Central Composite Design

We know that the thickness of a gold layer directly impacts the plasmonic resonance of the film. Similarly, the size and shape of the nanopores formed in the freestanding MgF_2 film will change as the thickness of the MgF_2 changes. To investigate these two potential factors affecting SERS performance at multiple levels, we can use a technique known as a Central Composite Design (CCD). Figure 6.26 describes the experimental design space. The experiment is centered on a hypothesized optimum for SERS performance, and then the testing space is expanded orthogonally along each of the factor conditions. The value of the CCD is that it reduces the

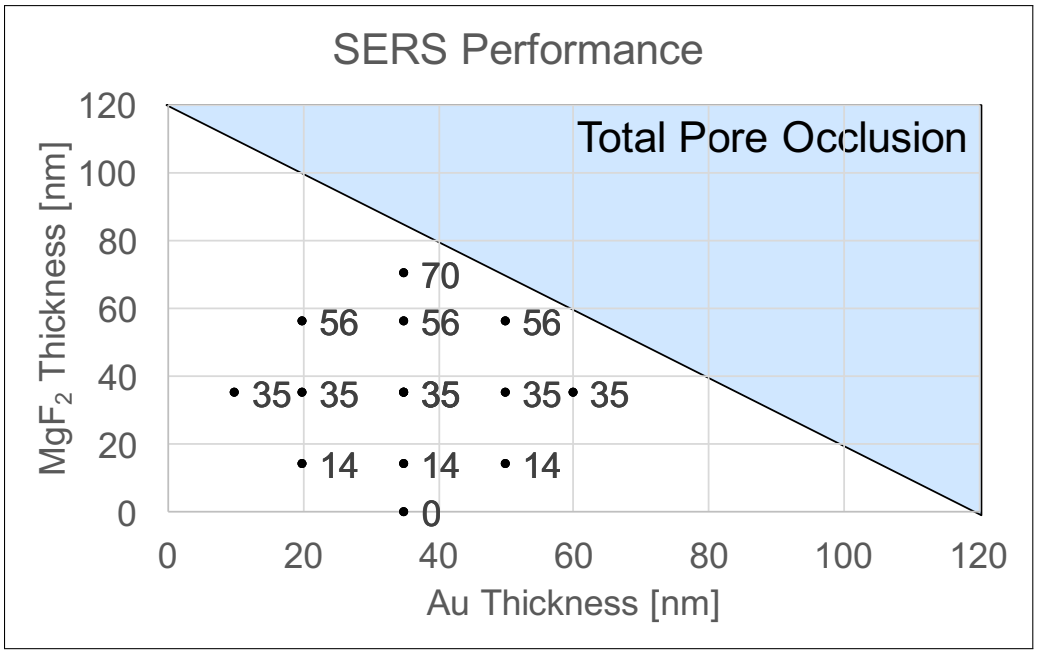

Figure 6.26: Central Composite Design of Au Thickness and MgF_2 Thickness for $npMg_2$ Thiophenol SERS Response. Numbers adjacent to points on the grid are targeted MgF_2 thicknesses.

number of experimental combinations to be tried, while still investigating the full range of the factors. A full 5^2 factorial design would have 25 combinations, but our CCD has only 13. The efficiency is gained by omitting the areas of the design where extreme combinations of the factors occur (max+max, max+min, min+max, min+min). This leads the experimental space to appear 'diamond-like', rather than the square in the case of the full factorial design. If other factors are considered, such as the starting NPN template distribution, the efficiency gains are even higher. The state diagram in Figure 6.26 shows a hypothetical area at which all the pores will

be occluded by the combination of gold and npMgF$_2$ thin films. The CCD also avoids this region. By interpolation, we hope to observe an optimum in the SERS performance of the npAu/npMgF$_2$ sensor.

6.8.2 Fabrication Characterization

Figure 6.27 displays the resultant manufacture of npMgF$_2$ chips for the CCD described in Figure 6.26. MgF$_2$ films were evaporated on NPN chips in 5 separate runs, and released using RIE as described in Figure 6.10. The format of these 1236 NPN (50 nm thick) chips was nine 50 x 50 μm square windows, with 49.5 nm average pore diameter and 25.3% porosity. Each of the films have different color viewed under white light due to the varying thickness of the deposited thin film. These colors match well by comparison with simulation (`https://www.filmetrics.com/reflectance-calculator`) using mixed polarization, 0° incident light for an Air-MgF$_2$-Si$_3$N$_4$-Si film stack; relative maxima at violet wavelengths (360-380 nm) in the reflected spectra occur for 50 nm and 70 nm MgF$_2$ thicknesses which contribute to the purple/blue colors at these thicknesses. While each of the depositions were targeted at certain evaporated thicknesses for the CCD outline in Figure 6.26, the produced thicknesses were slightly different, but sufficient to capture the spread of the experimental design.

Figure 6.28 depicts representative TEM micrographs of the fabricated npMgF$_2$ chips. As the deposited thin film thickness increases, the porosity

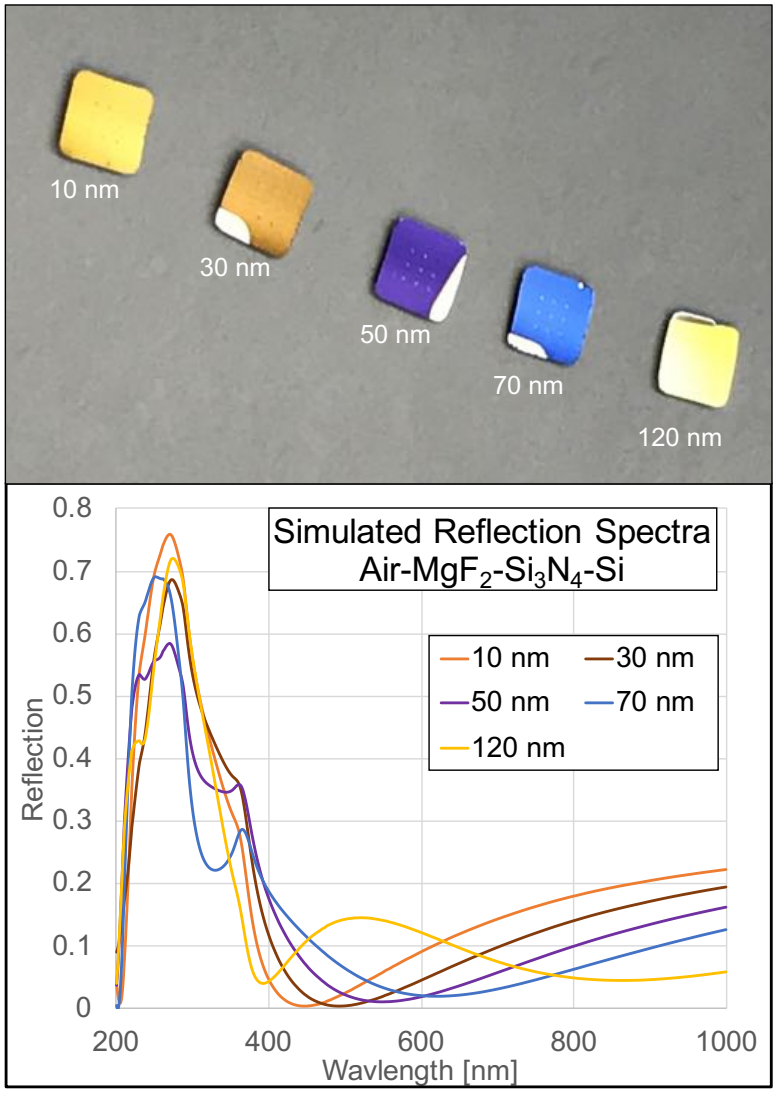

Figure 6.27: CCD npMgF$_2$ Fabricated Chip Colors. npMgF$_2$ of different thicknesses produce different colors when illuminated with white light due to thin film interferometric effects on top of the 50 nm NPN + Si substrate. Yellow-brown (10 nm), brown (30 nm), purple (50 nm), blue (70 nm), and yellow-gold (120 nm) were observed in room light. Spectra were simulated (`https://www.filmetrics.com/reflectance-calculator`) using mixed polarization, 0° incident light for an Air-MgF$_2$-Si$_3$N$_4$-Si film stack by varying the MgF$_2$ thickness. Relative maxima at violet wavelengths (360-380 nm) occur for 50 nm and 70 nm MgF$_2$ thicknesses.

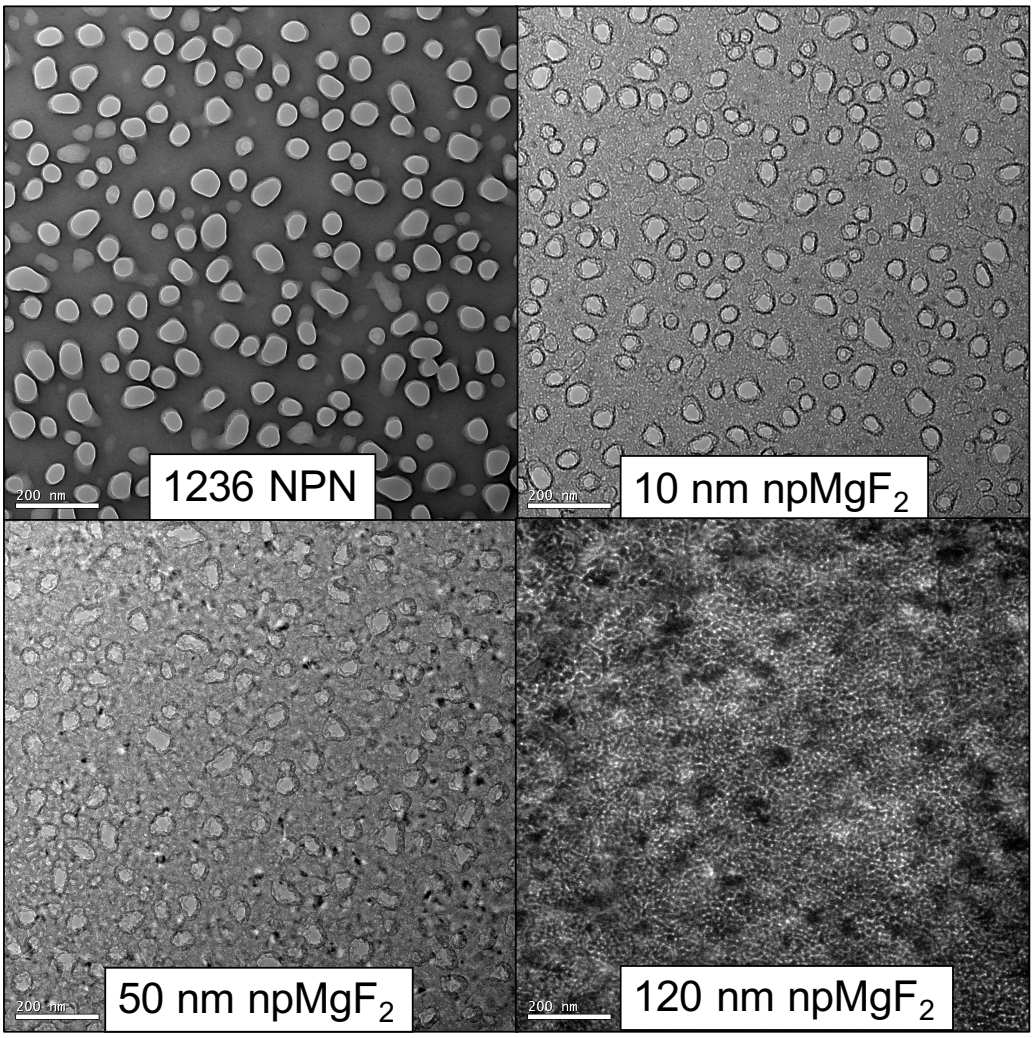

Figure 6.28: CCD $npMgF_2$ TEM Aerial Images. Pores become more occluded as the thickness of the $npMgF_2$ increases.

of the membranes decrease due to infilling along the substrate pore walls. The pore structure also changes as the infilling occurs, becoming more jagged and irregular. The TEM imaging also suffers as the thickness of the sample increases.

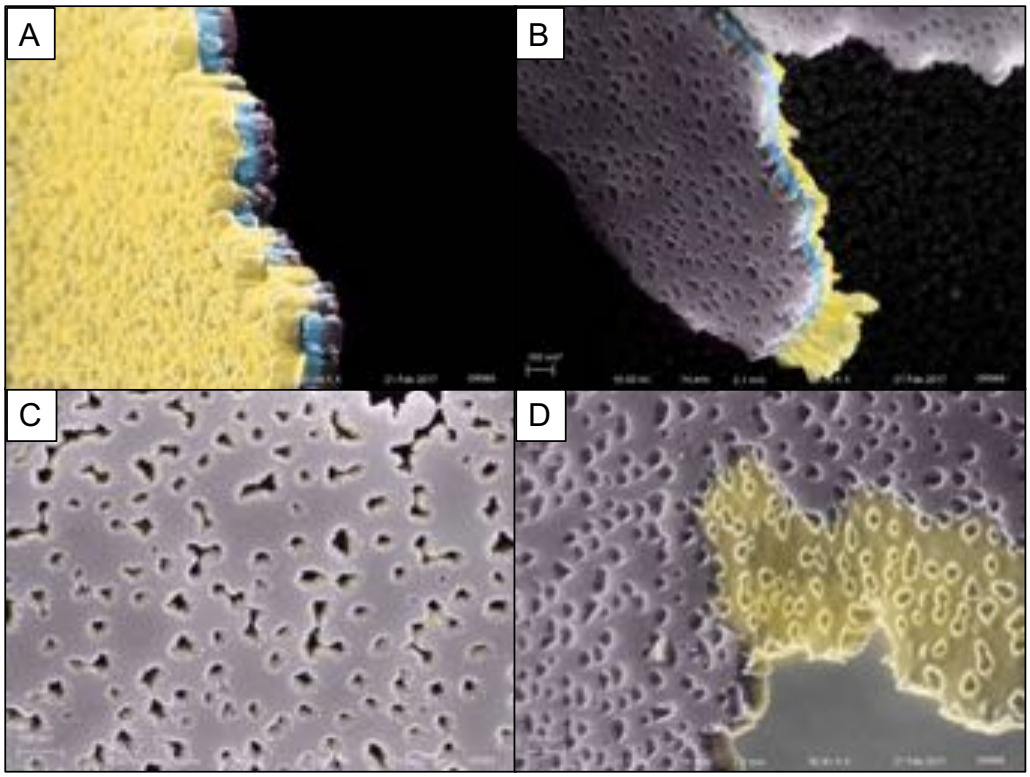

Figure 6.29: CCD npMgF$_2$ Structural SEM. False colored. (A) Cross-section of 1236 NPN (purple), 50 nm thick npMgF$_2$ (blue), and 50 nm thick npAu (yellow). (B) Viewed from the NPN template side, the npAu has small cones of gold, infilling the npMgF$_2$. (C) 1236 NPN etched for 40 seconds shows a high degree of pore merging. The npAu film conforms to the irregular shape of the pores. (D) 1236 NPN etched for 30 seconds show wider pores, and the npAu fills this pattern faithfully.

Figure 6.29 depicts representative SEM images of npAu/npMgF$_2$ and npAu/npMgF$_2$. The false color helps outline the different materials in the

film stacks. The npAu is shown penetrating the npMgF_2 layer along the irregular cuts of the cross-section; they are the inner surfaces of gold cones filling the nanopores. Similarly in Figure 6.29B, the npAu layer is delaminated and the gold cones are revealed. 6.29C, D have npAu templated on top of 1236 NPN that has been further etched and thinned to create wider pore distributions. The merged pores create tortuous shapes that appear to support the adhesion of gold to NPN, without the need for a separate adhesion layer.

6.8.3 Detection of Thiophenol on Nanostructured Nanomembranes

Partially etched silicon-based nanomembranes would produce a different pore distribution and surface than the original template and thus might impact some of the SERS activity inside the pores. Figure 6.30 displays thiophenol SERS spectra collected from npAu/NPN membranes. A simple ratio of the signal to the average background level (SAB) was used as a metric for evaluating the strength of SERS response. The strong characteristic peaks of thiophenol are observed (1575, 1075, 1023, and 1000 cm^{-1}), but the smaller peaks are not present as in Figure 6.14. Each of the partially etched membranes is similar to unetched NPN, indicating that larger pore diameters alone may not be helpful in recapturing stronger SERS activity. However, by partially etching the NPN templates, we reduced the internal surface area of the nanomembrane, thus reducing the deposition area for

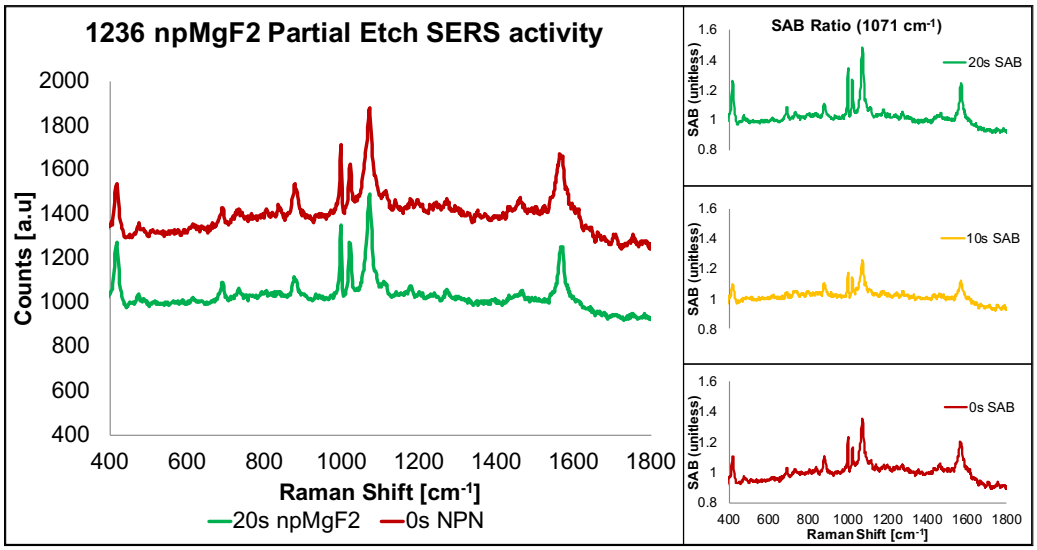

Figure 6.30: CCD 1236 npMgF$_2$ Partial Etch SERS Activity. Thiophenol was incubated on npAu/npMgF$_2$ (50 nm/ 50 nm) formed on partially etched NPN templates, displaying only weak SERS activity (λ = 725 nm, 10 s integration, 2 mW). The signal-average-background ratio for the 1075 cm^{-1} peak of thiophenol is calculated. The npAu/npMgF$_2$ produced from a partially etched substrate (1.48, 20 s) shows a small improvement over a baseline NPN template (1.35, 0 s).

MgF$_2$ and Au, which could confound the pore distribution/size impact on the sensor's performance.

A typical result from the CCD is shown in Figure 6.31, where the performance of the npAu/npMgF$_2$ is evaluated against npAu/NPN made from the same template. For all npAu/npMgF$_2$ combinations, the npAu/NPN had stronger SERS performance. However, given imaging conditions similar to Figure 6.14, the performance is diminished, below Klarite® and more in line with freestanding npAu. Comparing these two structures indicates that the npMgF$_2$ or NPN substrate had little effect on the SERS performance for this amount of gold. At a similar deposited gold thickness, the inner struc-

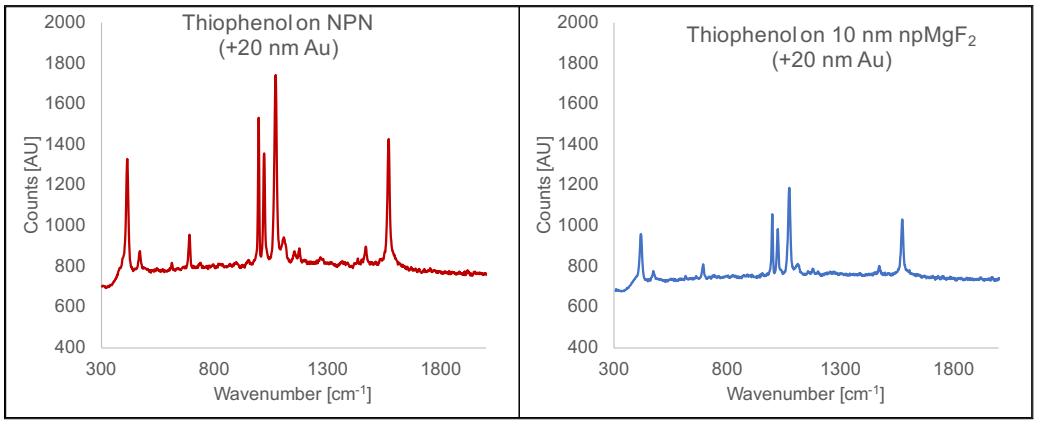

Figure 6.31: 1236 NPN Template Stronger SERS Than npMgF$_2$. Thiophenol spectra are displayed for 1236 npAu/NPN and 1236 npAu/npMgF$_2$ (λ = 725 nm, 10 s integration, 2 mW).

ture of the nanopore governs the npAu cones that form, which should be contiguous above 30 nm, and nested particles below 30 nm, based on previous TEM imaging (Figure 6.23). All npMgF$_2$ templates have smaller pore distributions than the template NPN due to infilling, as well as having more irregular shapes, and this would be the chief difference in the contours of gold cones that form inside the nanopores of each material. In this case, wider template pores seem to give better SERS performance.

Figure 6.32 displays the SERS response characteristics for the CCD. Using a metric of SAB $\geq$ 1.2, thiophenol can be detected on both substrates with these imaging conditions. The fact that the response characteristic is not the same shape for each substrate type demonstrates that the SERS response is not affected by npAu alone, rather, there is be a significant interaction between the gold layer deposited and the substrate. The nanos-

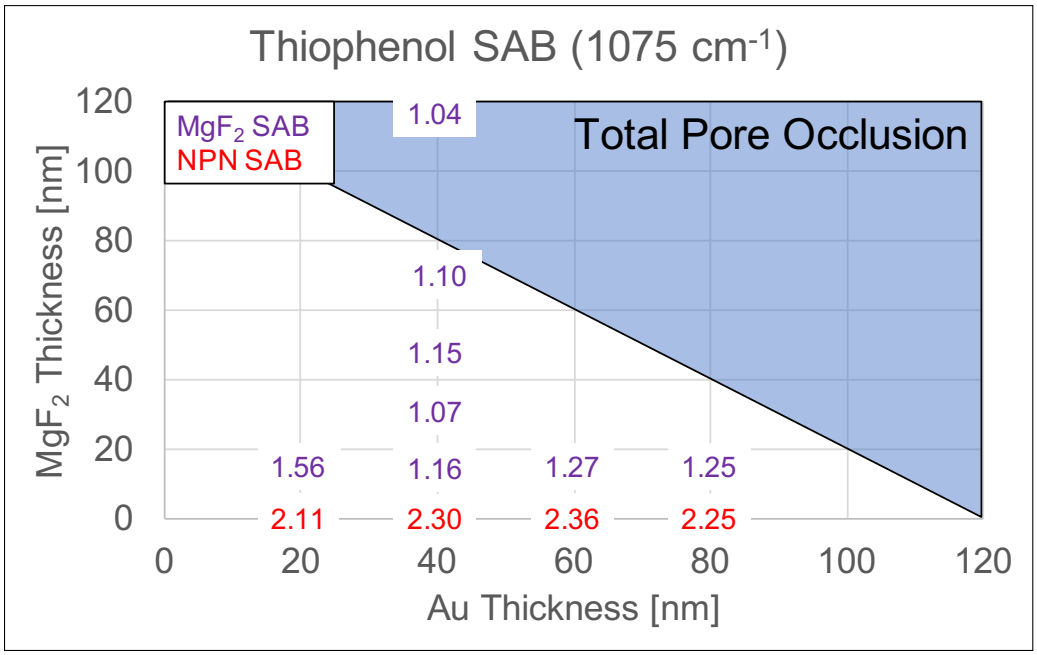

Figure 6.32: CCD 1236 NPN and npAu/npMgF$_2$ SERS Response Characteristics. The signal-average-background ratio for the 1075 cm^{-1} peak of thiophenol is calculated. The NPN has a stronger overall signal/background relationship, but is maximized at a different thickness of gold than the 10 nm npMgF$_2$, indicating that the SERS response can be influenced by the underlying layer. However, for a consistent thickness of gold, the deposited npMgF$_2$ thickness does not influence the SAB ratio.

tructure of the nanomembranes impacts the SERS response, producing better SAB ratios at different optimums. For a thinner level of gold deposition, the npMgF$_2$ based sensor has a marked improvement (SAB = 1.56 vs 1.22 avg). The same gold thickness produces the opposite effect for the NPN based sensor, providing a relative decrease in SERS response (SAB = 2.36 vs 2.11). Based on previous TEM images, the npAu in the nanopores may be incomplete cones of gold or stratified oblate nanoparticles, but the fact that the substrates differ in characteristic indicate that the

gold structures do not behave the same in each substrate material.

However, measured near the SAB optimum of gold thickness for NPN, the SAB of npAu/npMgF_2 is not impacted by the underlying changes in pore structure, remaining flat from 10-100 nm. We designed the CCD to be centered on a theoretical optimum for both gold and MgF_2 thickness factors, but this result indicates that we have not found an optimum peak along the central part of the design. If the SERS structure depends on morphological characteristics in fabrication that aren't linear (npAu nanocones vs npAu oblate nanoparticles), this design could be too broadly spaced to find it.

6.8.4 Detection of Mercaptans on Nanostructured Nanomembranes

Thiophenol is not the only molecule that can be detected on npAu substrates. Other molecules closely related in structure can be detected, such as mercaptans. These molecules are more interesting because they are used as additives in the food processing industry. Additionally, they are closely related to the thiophenol standard we have been using as a reporter molecule; the benzene ring and the positioning of the thiol group for gold attachment are key differences. After incubation with a 1236 npAu/NPN sensor, Figure 6.33 displays the results of detecting a variety of mercaptan compounds on separate chips. This displays the utility of SERS as a general chemical sensor; each of the mercaptans has a different Raman spec-

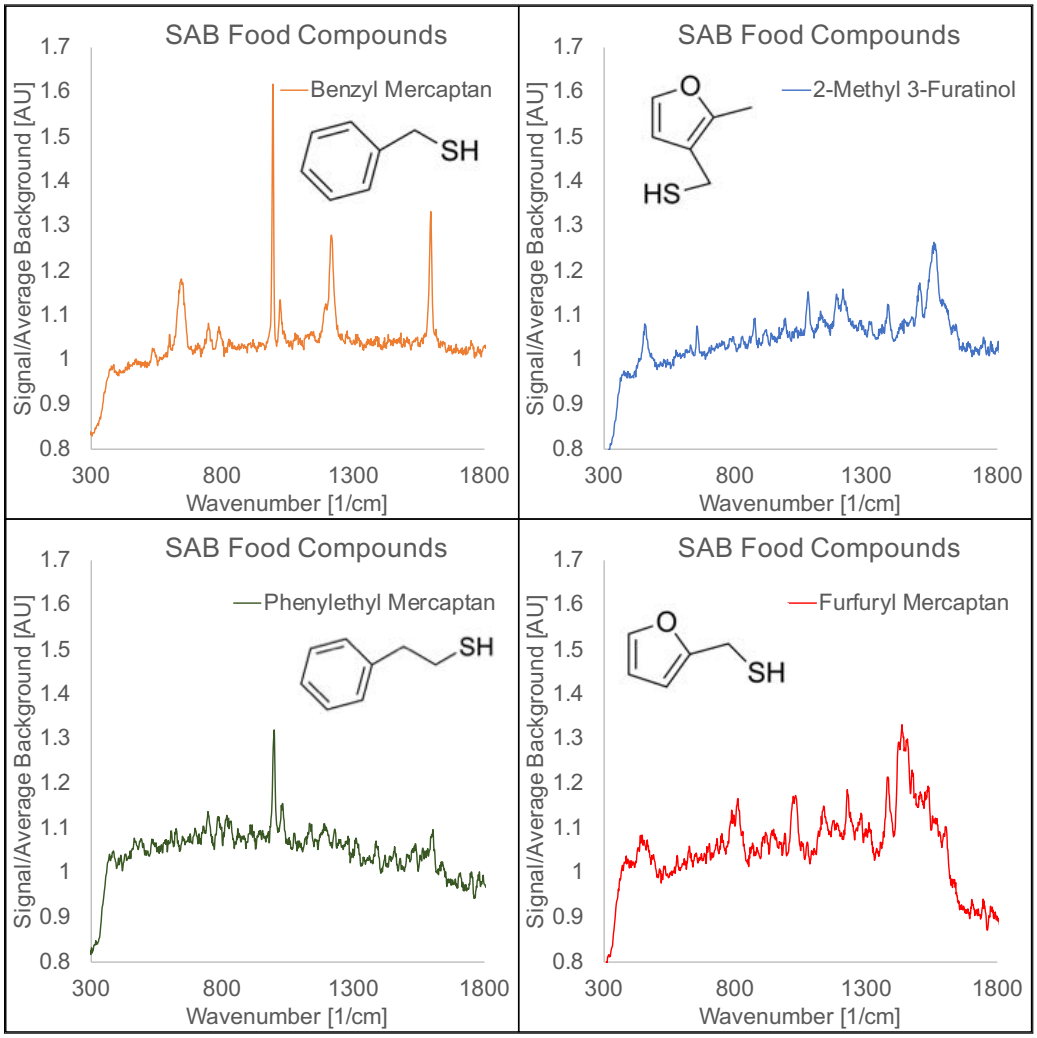

Figure 6.33: Mercaptan Detection via SERS on 1236 npAu/NPN. Mercaptan Detection on 10/50 nm thick npAu/NPN. 2-Methyl 3-Furatinol (roast-beef), benzyl mercaptan (garlic-like), furfuryl mercaptan (coffee flavor), and phenylethyl mercaptan (meat-like) have peaks that can be detected 20% above the background signal level.

tra. Ideally, spectra from mixtures of molecules could be identified using principal component analysis and measured quantitatively. Here, we can detect many separate mercaptan peaks by using a metric of SAB $\geq$ 1.2. The closest related molecule (by structure) to thiophenol, benzyl mercaptan, displays several peaks with a maximal SAB of 1.6, while phenylethyl mercaptan only differs by a single bond length and only one peak with SAB of 1.3. The furfuryl compounds have more complicated spectra compared to the benzene-ring containing mercaptans, which given the level of noise in the signal, makes only a few peaks available at our metric level.

6.9 Challenges and Future Directions

In this chapter, we have created and characterized silicon-based nanomembrane chemical sensors that could be used in a flow-through configuration. SERS detection is attractive because it has the potential to be used across many different analytes with excellent sensitivity.

However, there is still a need to examine the characteristics of npAu on silicon-based nanomembranes. While modulating npMgF_2 and npAu layer thicknesses alone has not yet recovered the original performance observed in Figure 6.14, both the template pore distribution and npAu surface configuration should be tested in a similar way. There have been difficulties in recreating material with the characteristics of Wafer 1085 NPN (50 nm thick, 67 nm average pore size, 60 pores/μm^2, Figure 6.20). This material

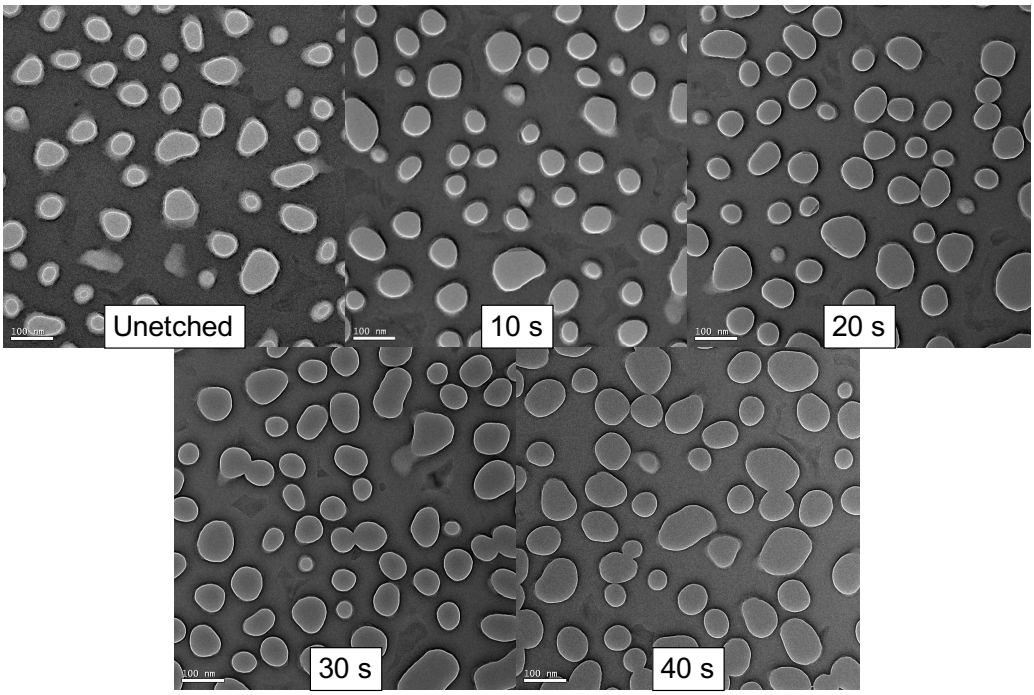

Figure 6.34: 1257 NPN Partial Etch TEM Study. RIE was used to thin the baseline nanomembrane and widen pores from their baseline size (57 nm average pore size, 62 pores/μm^2) and thickness (100 nm).

was the substrate upon which the original SERS discoveries were made (Figure 6.14). All the NPN material used to build npMgF_2/npAu sensors afterwards has had smaller pores and pore densities, or etched too thinly (Figure 6.29). Recently, a series of timed etches on a 100 nm thick NPN substrate (Wafer 1257, Figure 6.34, Figure 6.35) has approached and superseded the pore characteristics from 1085 NPN, allowing us to attempt a new set of experiments from material that more resembles the original template.

A number of observations point toward the structure of npAu inside

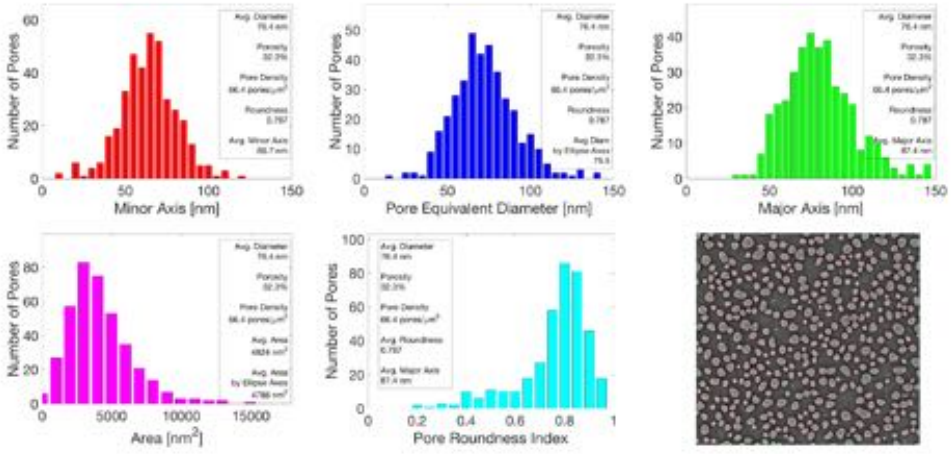

Figure 6.35: 1257 NPN Partial Etch Pore Statistics. RIE (20s) was used to widen pores from their baseline size. (Top Left) Minor Axis, (Top Center) Pore Equivalent Diameter, (Top Right) Major Axis of nanopore histograms. (Bottom Left) Area of nanopore Histogram. (Bottom Center) Roundness of nanopore Histogram. (Bottom Right) TEM Aerial image used to calculate pore statistics. Tomographic reconstruction of pores from sample estimate the thickness of the etched membrane as 68 nm thick.

the nanopores as being the key factor in SERS activity for these sensing schemes:

- The strongest enhancement factors occur between gaps with single nanometer sized spacings [171]. Gaps on the order of 6 nm produce enhancement factors around 10^8, while gaps less than 2 nm apart could lead to enhancement factors on the order of 10^{11}.
- Gold is known to coalesce into thin films around 50 nm thick [172]. Below this thickness, nanoparticles or islands of gold form, before coalescing into a contiguous film [173].
- We have observed that the thickness of the gold inside the nanopores

can create complicated particle and thin film surfaces (Figures 6.23 and 6.22).

- Data presented in Figure 6.32 suggests that the SERS properties of the npAu can change depending on the underlying template. A very thin deposition of gold provided the relative best SAB for the npMgF_2 in the CCD, but the relative worst SAB for the NPN substrate.

- Freestanding npAu would lack any ability to host gold nanoparticles away from the contiguous gold film. A template could serve as a substrate if the gold film separated into particles inside the nanopore.

- Freestanding npAu has considerably lower SERS activity than the combined npAu/npMgF_2 film stack in Figure 6.14.

Assuming that the gold structures inside the nanopores are mostly responsible for the SERS performance, if the nanoparticle separation/disintegration observed in Figure 6.23 occurred for sensors measured in Figure 6.14, but not Figure 6.30 or 6.31, this could explain differences measured between them. Arranging tiny nanoparticles in such a small space would be difficult as they are not necessarily well-adhered to the substrate. Given the large non-linear response of SERS, it would be difficult to create reproducible substrates which depend on nanometer sized spacings of nanoparticles. Even small changes in the sputter deposition system could influence the size and shape of particles deposited on substrates. However, a nanopore template provides a way to confine and limit the scale

of gold film transformations. Furthermore, the npAu structure fabricated in nanopores could be evaluated against SERS performance in a few different ways:

- SERS activity could be recorded and then the Au nanostructures in nanopores could be imaged and reconstructed using electron tomography, in a blinded study. This provides a control against motivated segmentations of particle structures, which is essential to defining small gaps between these reconstructions.
- The structure of nanoparticles formed inside npAu cones can be changed via chemical etchants, heat treatments, or other in-situ processing which should also change SERS performance.
- The underlying substrate structure (NPN or npMgF_2) could influence the kinetics of npAu film growth/disintegration and provide changes in SERS performance.
- If the same gold nanoparticles exist in both film stacks, removal of the baseline NPN from npMgF_2 in the fabrication flow should not impact the SERS performance, except as an additional opacity to be considered while collecting photons or changing the refractive index of the boundary condition for these particles. However, if the baseline NPN removal is essential to the formation of a particular npAu structure, it could drastically impact the SERS performance.

- Nanoparticle (5-25 nm spheres) and nanorod features (40-70 nm long, 10-20 nm wide, Aspect Ratio: 2-4) observed in Figure 6.23 would have certain extinction characteristics that could be predicted with a 3D electrostatic simulation as well as potentially optimized for the illumination wavelength. The simulation is necessary due to the density of features, as Ni et al. [169] indicates that both the specific curved shape of the ends of gold nanorods and the arrangement of side-by-side nanorods (like stratified structures observed in Figure 6.23) can blue-shift the absorption peaks by hundreds of nanometers. Figure 6.4 displays extinction characteristics for a large variety of gold nanorods [158]. For 725 nm illumination, a homogeneous nanorod population with an aspect ratio of $\sim$3 would seem to be optimal.

Combined with the additional tomography techniques demonstrated here, it would be possible to create more faithful representations of the gold nanostructures than is commonly done with SERS based simulations, which would lead to better information about the enhancement of the nanostructures. A combination of fabrication method, template size, template material, and template shape is likely to create a variety of rough surfaces and these could be imaged, reconstructed, and simulated faithfully, with real comparisons of SERS activity.

Chapter 7

Summary and Outlook

In this work, we have advanced the use of silicon nanomembrane technology to overcome limitations in novel platforms for molecular sensing. In Chapters 2 and 3, we constructed a DNA straightening element over a single nanopore sensor that facilitated measurements through the nanomembrane. In this case, the chief limitation was to create a porous cavity that would not interfere with the ability of the sensor to attract DNA. The limitation was overcome by a fabrication technique that facilitated *in situ* fabrication of a wet, porous, self-aligned cavity. In Chapter 5, we created a Raman-silent substrate for material compatibility with a particular technique, improving the substrate for certain cell cultures by making substrate porous. Here, the chief limitation was the silicon-derived nanomembrane having a Raman background inimical to making biological measurements. Silicon nanomembranes, such as pnc-Si, have strong spectral peaks near the biological fingerprint region and are destroyed by a modest amount of illumination power (30 mW). The limitation was overcome by a fabrication

technique that copied the silicon-derived nanomembrane's pore structure into a Raman-compatible materials (MgF_2); a process that is adaptable to many other materials for other applications.

In Chapter 6, we developed a silicon-based nanomembrane SERS sensor that can detect and distinguish an array of with many different analytes, demonstrated here with industrially-relevant food flavoring compounds sharing structural similarity to the gold-standard comparison analyte (thiophenol). A key limitation of many SERS sensors is the heterogeneity of SERS enhancement, observed both among and within individual sensors. This limitation was improved upon by shifting the SERS sensing structure into narrowly confined nanopores, which also facilitates efficient introduction of the analyte to the sensing surface. Though the SERS-active npAu layer demands further investigation, a strategy for quantifying the performance of the behavior was developed through TEM tomography reconstruction techniques (Chapter 4). The combination of powerful computational hardware, freely available software, and precise electron microscopy tools will permit investigation into the organization of realistic gold nanostructures at a scale that is often simulated, but not validated, in 3D. As the spacing between such structures exponentially affects the strength of the SERS effect, nanometer-scale positioning of nanoparticles has a dramatic effect on the efficacy of the device.

The process flexibility of the silicon nanomembrane stems in part from it's basis in semiconductor fabrication technology, in which this work uti-

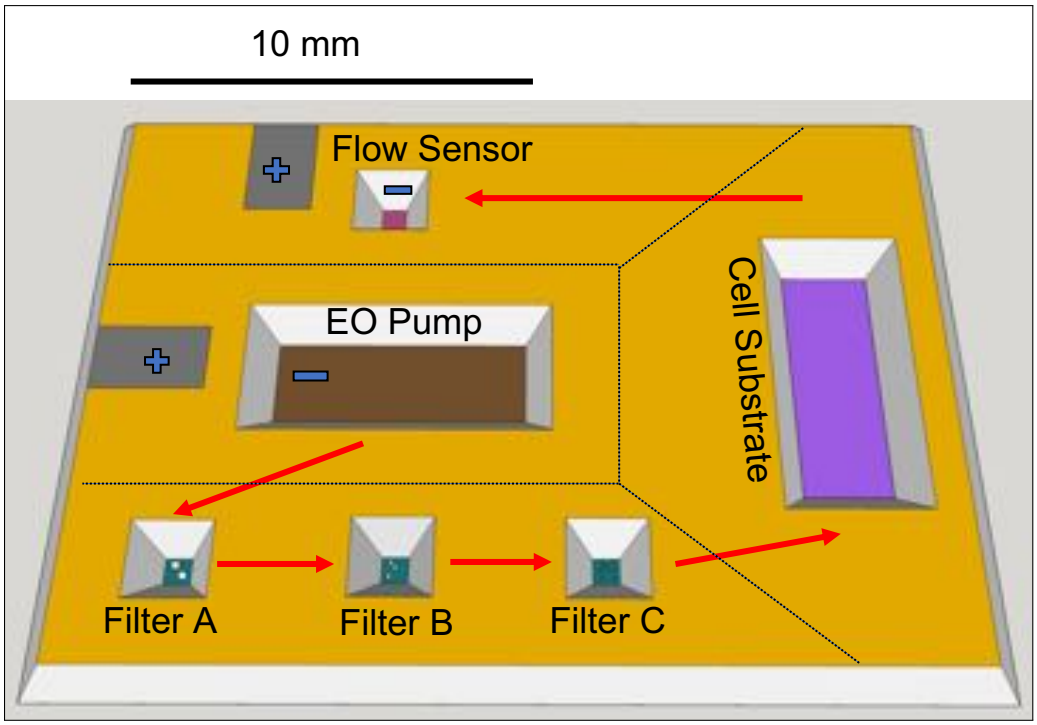

Figure 7.1: Silicon Nanomembrane Microsystem. Different regions on a silicon nanomembrane chip are defined through the use of semiconductor processing techniques. These regions can be developed with individual characteristics at scale with the appropriate process flow. Combining the chip with imprint-lithography PDMS microfluidics and metallized contact patches would facilitate the creation of a lab-on-a-chip device that can pump, filter, sense, and support reactants/analytes within the system.

lizes many different techniques to accomplish its goals. This same flexibility can be used to not only develop separate process flows for particular applications, but to integrate and combine many different measurements in a single miniaturized space. Figure 7.1 describes this concept.

Many separate applications of silicon-based nanomembranes have been discussed above or researched as chemical sensors [17, 44], filters [3, 18], cell culture substrates [4, 19], electroosmotic pumps [20] or as a protec-

tive element [21]. These applications have the potential to be miniaturized and optimized together at the locus of detection. This would minimize the amount of 'dead-volume' in a fluidic application, preventing wasteful and inefficient use of expensive reagents, as well as permit the interrogation of very tiny sample volumes. The layout of this microsystem could be patterned using common lithographic and etching tools, after which other materials could be deposited and removed using a combination of masking layers. These layers could include electrode contacts, observation windows, nanopore or micropore filters, all made of different materials optimized for their particular application. Considering a useful range of microfluidic channel cross-section geometries (50 x 50 μm to 1000 x 1000 μm), samples on the order of 1-100 μL could be efficiently transported by electroosmotic pump, pushed through a set of size filters, observed under a microscope, and detected by chemical sensors in a package the size of a thumbnail.

In conclusion, there are many different strategies used in biosensing and the silicon-based nanomembrane platform has been made useful for many different forms of metrology. Confining molecules or reagents of interest into nanometer-sized containers continues to be a fruitful area of exploration. Facilitating other forms of metrology while maintaining the structure of the nanomembrane is essential to the usefulness of these explorations. The versatility of the silicon-based nanomembrane platform is an asset, and will continue to be in demand as new and challenging appli-

cations arise.

Bibliography

[1] Albert van den Berg and Matthias Wessling. Silicon for the perfect membrane. *Nature*, 445:726, 2007. doi: 10.1038/445726a. URL http://dx.doi.org/10.1038/445726a.

[2] Christopher C. Striemer, Thomas R. Gaborski, James L. McGrath, and Philippe M. Fauchet. Charge- and size-based separation of macromolecules using ultrathin silicon membranes. *Nature*, 445 (7129):749–753, 2007. ISSN 0028-0836. URL http://dx.doi.org/10.1038/nature05532.

[3] Thomas R. Gaborski, Jessica L. Snyder, Christopher C. Striemer, David Z. Fang, Michael Hoffman, Philippe M. Fauchet, and James L. McGrath. High-performance separation of nanoparticles with ultrathin porous nanocrystalline silicon membranes. *ACS Nano*, 4(11): 6973–6981, 2010. ISSN 1936-0851. doi: 10.1021/nn102064c. URL http://dx.doi.org/10.1021/nn102064c.

[4] A. A. Agrawal, B. J. Nehilla, K. V. Reisig, T. R. Gaborski, D. Z. Fang, C. C. Striemer, P. M. Fauchet, and J. L. McGrath. Porous nanocrystalline silicon membranes as highly permeable and molecularly thin substrates for cell culture. *Biomaterials*, 31(20):5408–5417, 2010. ISSN 0142-9612. doi: http://dx.doi.org/10.1016/j.biomaterials.2010.03.041. URL http://dx.doi.org/10.1016/j.biomaterials.2010.03.041.

[5] Nikhil Bhalla, Pawan Jolly, Nello Formisano, and Pedro Estrela. Introduction to biosensors. *Essays in Biochemistry*, 60(1):1–8, 2016. ISSN 0071-1365 1744-1358. doi: 10.1042/EBC20150001. URL http://www.ncbi.nlm.nih.gov/pmc/articles/PMC4986445/.

[6] J. M. Nelson and Edward G. Griffin. Adsorption of invertase. *Journal of the American Chemical Society*, 38(5):1109–1115, 1916. ISSN 0002-7863. doi: 10.1021/ja02262a018. URL https://doi.org/10.1021/ja02262a018.

[7] P. Bergveld. Development of an ion-sensitive solid-state device for neurophysiological measurements. *IEEE Transactions on Biomedical Engineering*, BME-17(1):70–71, 1970. ISSN 0018-9294. doi: 10.1109/TBME.1970.4502688.

[8] Jiali Li, Derek Stein, Ciaran McMullan, Daniel Branton, Michael J. Aziz, and Jene A. Golovchenko. Ion-beam sculpting at nanometre length scales. *Nature*, 412:166, 2001. doi: 10.1038/35084037. URL http://dx.doi.org/10.1038/35084037.

[9] David Z. Fang, Christopher C. Striemer, Thomas R. Gaborski, James L. McGrath, and Philippe M. Fauchet. Pore size control of ultrathin silicon membranes by rapid thermal carbonization. *Nano Letters*, 10(10):3904–3908, 2010. ISSN 1530-6984. doi: 10.1021/nl101602z. URL http://dx.doi.org/10.1021/nl101602z.

[10] D. Z. Fang, C. C. Striemer, T. R. Gaborski, J. L. McGrath, and P. M. Fauchet. Methods for controlling the pore properties of ultrathin nanocrystalline silicon membranes. *Journal of Physics: Condensed Matter*, 22(45):454134, 2010. ISSN 0953-8984. URL http://stacks.iop.org/0953-8984/22/i=45/a=454134.

[11] M. N. Kavalenka, C. C. Striemer, D. Z. Fang, T. R. Gaborski, J. L. McGrath, and P. M. Fauchet. Ballistic and non-ballistic gas flow through ultrathin nanopores. *Nanotechnology*, 23(14):145706, 2012. ISSN 0957-4484. URL http://stacks.iop.org/0957-4484/23/i=14/a=145706.

[12] Eunkyoung Kim, Hui Xiong, Christopher C. Striemer, David Z. Fang, Philippe M. Fauchet, James L. McGrath, and Shigeru Amemiya. A structure?permeability relationship of ultrathin nanoporous silicon membrane:? a comparison with the nuclear envelope. *Journal of the American Chemical Society*, 130(13):4230–4231, 2008. ISSN 0002-7863. doi: 10.1021/ja711258w. URL http://dx.doi.org/10.1021/ja711258w.

[13] J. L. Snyder, A. Clark Jr, D. Z. Fang, T. R. Gaborski, C. C. Striemer, P. M. Fauchet, and J. L. McGrath. An experimental and theoretical analysis of molecular separations by diffusion through ultrathin nanoporous membranes. *Journal of Membrane Science*, 369 (1?2):119–129, 2011. ISSN 0376-7388. doi: http://dx.doi.org/10.1016/j.memsci.2010.11.056. URL http://dx.doi.org/10.1016/j.memsci.2010.11.056.

[14] Getpreecharsawas Jirachai, L. McGrath James, and A. Borkholder David. The electric field strength in orifice-like nanopores of ultrathin membranes. *Nanotechnology*, 26(4):045704, 2015. ISSN 0957-4484. URL http://stacks.iop.org/0957-4484/26/i=4/a=045704.

[15] Ryoichi Ishimatsu, Jiyeon Kim, Ping Jing, Christopher C. Striemer, David Z. Fang, Philippe M. Fauchet, James L. McGrath, and Shigeru Amemiya. Ion-selective permeability of an ultrathin nanoporous silicon membrane as probed by scanning electrochemical microscopy using micropipet-supported ities tips. *Analytical Chemistry*, 82(17): 7127–7134, 2010. ISSN 0003-2700. doi: 10.1021/ac1005052. URL http://dx.doi.org/10.1021/ac1005052.

[16] J. D. Winans, K. J. P. Smith, T. R. Gaborski, J. A. Roussie, and J. L. McGrath. Membrane capacity and fouling mechanisms for ultrathin nanomembranes in dead-end filtration. *Journal of Membrane Science*, 499:282–289, 2016. ISSN 0376-7388. doi: https://doi.org/10.1016/j.memsci.2015.10.053. URL http://www.sciencedirect.com/science/article/pii/S0376738815302830.

[17] Maryna N. Kavalenka, Christopher C. Striemer, Jon-Paul S. DesOrmeaux, James L. McGrath, and Philippe M. Fauchet. Chemical capacitive sensing using ultrathin flexible nanoporous electrodes. *Sensors and Actuators B: Chemical*, 162(1):22–26, 2012. ISSN 0925-4005. doi: http://dx.doi.org/10.1016/j.snb.2011.11.076. URL http://dx.doi.org/10.1016/j.snb.2011.11.076.

[18] Dean G. Johnson, Tejas S. Khire, Yekaterina L. Lyubarskaya, Karl J. P. Smith, Jon-Paul S. DesOrmeaux, Jeremy G. Taylor, Thomas R. Gaborski, Alexander A. Shestopalov, Christopher C. Striemer, and

James L. McGrath. Ultrathin silicon membranes for wearable dialysis. *Advances in Chronic Kidney Disease*, 20(6):508–515, 2013. ISSN 1548-5595. doi: https://doi.org/10.1053/j.ackd.2013.08.001. URL https://doi.org/10.1053/j.ackd.2013.08.001.

[19] Barrett J. Nehilla, Nakul Nataraj, Thomas R. Gaborski, and James L. McGrath. Endothelial vacuolization induced by highly permeable silicon membranes. *Acta Biomaterialia*, 10(11):4670–4677, 2014. ISSN 1742-7061. doi: http://dx.doi.org/10.1016/j.actbio.2014.07.022. URL http://dx.doi.org/10.1016/j.actbio.2014.07.022.

[20] Jessica L. Snyder, Jirachai Getpreecharsawas, David Z. Fang, Thomas R. Gaborski, Christopher C. Striemer, Philippe M. Fauchet, David A. Borkholder, and James L. McGrath. High-performance, low-voltage electroosmotic pumps with molecularly thin silicon nanomembranes. *Proceedings of the National Academy of Sciences*, 110(46):18425–18430, 2013. doi: 10.1073/pnas.1308109110. URL http://www.pnas.org/content/110/46/18425.abstract.

[21] Henry H. Chung, Charles K. Chan, Tejas S. Khire, Graham A. Marsh, Alfred Clark, Richard E. Waugh, and James L. McGrath. Highly permeable silicon membranes for shear free chemotaxis and rapid cell labeling. *Lab on a Chip*, 14(14):2456–2468, 2014. ISSN 1473-0197. doi: 10.1039/C4LC00326H. URL http://dx.doi.org/10.1039/C4LC00326H.

[22] J. P. S. DesOrmeaux, J. D. Winans, S. E. Wayson, T. R. Gaborski, T. S. Khire, C. C. Striemer, and J. L. McGrath. Nanoporous silicon nitride membranes fabricated from porous nanocrystalline silicon templates. *Nanoscale*, 6(18):10798–10805, 2014. ISSN 2040-3364. doi: 10.1039/C4NR03070B. URL http://dx.doi.org/10.1039/C4NR03070B.

[23] Steven R. Gillmer, David Z. Fang, Sarah E. Wayson, Joshua D. Winans, Niaz Abdolrahim, Jon-Paul S. DesOrmeaux, Jirachai Getpreecharsawas, Jonathan D. Ellis, Philippe M. Fauchet, and James L. McGrath. Predicting the failure of ultrathin porous membranes in bulge tests. *Thin Solid Films*, 631:152–160, 2017. ISSN

0040-6090. doi: https://doi.org/10.1016/j.tsf.2017.04.004. URL https://doi.org/10.1016/j.tsf.2017.04.004.

[24] Krishanu Shome. *Interaction of Light with Metallized Ultrathin Silicon Membrane*. PhD thesis, University of Rochester, New York, 2013.

[25] Fatemeh Eftekhari, Carlos Escobedo, Jacqueline Ferreira, Xiaobo Duan, Emerson M. Girotto, Alexandre G. Brolo, Reuven Gordon, and David Sinton. Nanoholes as nanochannels: Flow-through plasmonic sensing. *Analytical Chemistry*, 81 (11):4308–4311, 2009. ISSN 0003-2700. doi: 10.1021/ac900221y. URL https://doi.org/10.1021/ac900221yhttps://pubs.acs.org/doi/pdfplus/10.1021/ac900221y.

[26] John. Crank. *The Mathematics of Diffusion*, page 32. Oxford: Clarendon Press, England, 1975. ISBN 0198533446, 0198534116.

[27] J. P. Brody, P. Yager, R. E. Goldstein, and R. H. Austin. Biotechnology at low reynolds numbers. *Biophysical Journal*, 71(6): 3430–3441, 1996. ISSN 0006-3495. doi: https://doi.org/10.1016/S0006-3495(96)79538-3.

[28] Meni Wanunu, Will Morrison, Yitzhak Rabin, Alexander Y. Grosberg, and Amit Meller. Electrostatic focusing of unlabeled dna into nanoscale pores using a salt gradient. *Nature nanotechnology*, 5(2):160–165, 2010. ISSN 1748-3387 1748-3395. doi: 10.1038/nnano.2009.379. URL http://www.ncbi.nlm.nih.gov/pmc/articles/PMC2849735/.

[29] Alexander Y. Grosberg and Yitzhak Rabin. Dna capture into a nanopore: Interplay of diffusion and electrohydrodynamics. *The Journal of Chemical Physics*, 133(16): 165102, 2010. doi: 10.1063/1.3495481. URL https://aip.scitation.org/doi/abs/10.1063/1.3495481https://aip.scitation.org/doi/pdf/10.1063/1.3495481.

[30] Axel E. Nkodo, Jean M. Garnier, Bernard Tinland, Hongji Ren, Claude Desruisseaux, Laurette C. McCormick, Guy Drouin, and Gary W. Slater. Diffusion coefficient of dna molecules during

free solution electrophoresis. *ELECTROPHORESIS*, 22(12):2424–2432, 2001. doi: doi:10.1002/1522-2683(200107)22:12<2424::AID-ELPS2424>3.0.CO;2-1.

[31] A. D. Hershey and Martha Chase. Independent functions of viral protein and nucleic acid in growth of bacteriophage. *The Journal of General Physiology*, 36(1):39–56, 1952. doi: 10.1085/jgp.36.1.39. URL http://jgp.rupress.org/content/jgp/36/1/39.full.pdf.

[32] Stefano Cagnin, Marcelo Caraballo, Carlotta Guiducci, Paolo Martini, Marty Ross, Mark SantaAna, David Danley, Todd West, and Gerolamo Lanfranchi. Overview of electrochemical dna biosensors: New approaches to detect the expression of life. *Sensors*, 9(4), 2009. ISSN 1424-8220. doi: 10.3390/s90403122.

[33] Gerald S. Manning. The persistence length of dna is reached from the persistence length of its null isomer through an internal electrostatic stretching force. *Biophysical Journal*, 91(10):3607–3616, 2006. ISSN 0006-3495 1542-0086. doi: 10.1529/biophysj.106.089029. URL http://www.ncbi.nlm.nih.gov/pmc/articles/PMC1630458/.

[34] Daniel Branton, David W. Deamer, Andre Marziali, Hagan Bayley, Steven A. Benner, Thomas Butler, Massimiliano Di Ventra, Slaven Garaj, Andrew Hibbs, Xiaohua Huang, Stevan B. Jovanovich, Predrag S. Krstic, Stuart Lindsay, Xinsheng Sean Ling, Carlos H. Mastrangelo, Amit Meller, John S. Oliver, Yuriy V. Pershin, J. Michael Ramsey, Robert Riehn, Gautam V. Soni, Vincent Tabard-Cossa, Meni Wanunu, Matthew Wiggin, and Jeffery A. Schloss. The potential and challenges of nanopore sequencing. *Nature Biotechnology*, 26:1146, 2008. doi: 10.1038/nbt.1495. URL http://dx.doi.org/10.1038/nbt.1495https://www.nature.com/articles/nbt.1495.pdf.

[35] Stephanie J. Heerema and Cees Dekker. Graphene nanodevices for dna sequencing. *Nature Nanotechnology*, 11:127, 2016. doi: 10.1038/nnano.2015.307. URL http://dx.doi.org/10.1038/nnano.2015.307https://www.nature.com/articles/nnano.2015.307.pdf.

[36] Harold Kwok, Kyle Briggs, and Vincent Tabard-Cossa. Nanopore fabrication by controlled dielectric breakdown. *PLOS ONE*, 9(3): e92880, 2014. doi: 10.1371/journal.pone.0092880.

[37] Meller Amit. Dynamics of polynucleotide transport through nanometre-scale pores. *Journal of Physics: Condensed Matter*, 15 (17):R581, 2003. ISSN 0953-8984. URL http://stacks.iop.org/0953-8984/15/i=17/a=202.

[38] Holly J. Butler, Lorna Ashton, Benjamin Bird, Gianfelice Cinque, Kelly Curtis, Jennifer Dorney, Karen Esmonde-White, Nigel J. Fullwood, Benjamin Gardner, Pierre L. Martin-Hirsch, Michael J. Walsh, Martin R. McAinsh, Nicholas Stone, and Francis L. Martin. Using raman spectroscopy to characterize biological materials. *Nature Protocols*, 11:664, 2016. doi: 10.1038/nprot.2016.036. URL http://dx.doi.org/10.1038/nprot.2016.036http://www.nature.com/articles/nprot.2016.036.

[39] C. V. Raman and K. S. Krishnan. A new type of secondary radiation. *Nature*, 121:501, 1928. doi: 10.1038/121501c0. URL http://dx.doi.org/10.1038/121501c0.

[40] Charles H. Camp Jr and Marcus T. Cicerone. Chemically sensitive bioimaging with coherent raman scattering. *Nature Photonics*, 9:295, 2015. doi: 10.1038/nphoton.2015.60. URL http://dx.doi.org/10.1038/nphoton.2015.60https://www.nature.com/articles/nphoton.2015.60.pdf.

[41] P.F. Bernath. *Spectra of Atoms and Molecules*, volume 8. Oxford University Press, 2005. ISBN 9780195346459.

[42] Katherine J. I. Ember, Marieke A. Hoeve, Sarah L. McAughtrie, Mads S. Bergholt, Benjamin J. Dwyer, Molly M. Stevens, Karen Faulds, Stuart J. Forbes, and Colin J. Campbell. Raman spectroscopy and regenerative medicine: a review. *npj Regenerative Medicine*, 2(1):12, 2017. ISSN 2057-3995. doi: 10.1038/s41536-017-0014-3. URL https://doi.org/10.1038/s41536-017-0014-3https://www.nature.com/articles/s41536-017-0014-3.pdf.

[43] Xiaoran Ning, Ivan W. Selesnick, and Laurent Duval. Chromatogram baseline estimation and denoising using sparsity (beads). *Chemometrics and Intelligent Laboratory Systems*, 139:156–167, 2014. ISSN 0169-7439. doi: https://doi.org/10.1016/j.chemolab.2014.09.014.

[44] Kyle Briggs, Gregory Madejski, Martin Magill, Konstantinos Kastritis, Hendrick W. de Haan, James L. McGrath, and Vincent Tabard-Cossa. Dna translocations through nanopores under nanoscale preconfinement. *Nano Letters*, 18(2):660–668, 2018. ISSN 1530-6984. doi: 10.1021/acs.nanolett.7b03987. URL `https://doi.org/10.1021/acs.nanolett.7b03987https://www.ncbi.nlm.nih.gov/pmc/articles/PMC5814347/pdf/nihms928590.pdf`.

[45] Carson Spencer and Wanunu Meni. Challenges in dna motion control and sequence readout using nanopore devices. *Nanotechnology*, 26(7):074004, 2015. ISSN 0957-4484. URL `http://stacks.iop.org/0957-4484/26/i=7/a=074004`.

[46] Cees Dekker. Solid-state nanopores. *Nature Nanotechnology*, 2:209, 2007. doi: 10.1038/nnano.2007.27. URL `http://dx.doi.org/10.1038/nnano.2007.27https://www.nature.com/articles/nnano.2007.27.pdf`.

[47] Stijn van Dorp, Ulrich F. Keyser, Nynke H. Dekker, Cees Dekker, and Serge G. Lemay. Origin of the electrophoretic force on dna in solid-state nanopores. *Nature Physics*, 5:347, 2009. doi: 10.1038/nphys1230. URL `http://dx.doi.org/10.1038/nphys1230https://www.nature.com/articles/nphys1230.pdf`.

[48] Marc Gershow and J. A. Golovchenko. Recapturing and trapping single molecules with a solid state nanopore. *Nature nanotechnology*, 2(12):775–779, 2007. ISSN 1748-3387 1748-3395. doi: 10.1038/nnano.2007.381.

[49] Bo Lu, Fernando Albertorio, David P Hoogerheide, and Jene A Golovchenko. Origins and consequences of velocity fluctuations during dna passage through a nanopore. *Biophysical Journal*, 101(1):70–79, 2011. ISSN 0006-3495. doi: https://doi.org/10.1016/j.bpj.2011.05.034.

[50] Kyle Briggs, Harold Kwok, and Vincent Tabard-Cossa. Automated fabrication of 2-nm solid-state nanopores for nucleic acid analysis. *Small*, 10(10):2077–2086, 2014. ISSN 1613-6829. doi: 10.1002/smll.201303602. URL http://dx.doi.org/10.1002/smll.201303602.

[51] Yuhui He, Makusu Tsutsui, Chun Fan, Masateru Taniguchi, and Tomoji Kawai. Controlling dna translocation through gate modulation of nanopore wall surface charges. *ACS Nano*, 5(7):5509–5518, 2011. ISSN 1936-0851. doi: 10.1021/nn201883b. URL https://doi.org/10.1021/nn201883b.

[52] Aleksij Aksimentiev, Jiunn B. Heng, Gregory Timp, and Klaus Schulten. Microscopic kinetics of dna translocation through synthetic nanopores. *Biophysical Journal*, 87(3):2086–2097, 2004. ISSN 0006-3495 1542-0086. doi: 10.1529/biophysj.104.042960. URL http://www.ncbi.nlm.nih.gov/pmc/articles/PMC1304610/.

[53] Matthew Waugh, Autumn Carlsen, David Sean, W. Slater Gary, Kyle Briggs, Harold Kwok, and Vincent Tabard-Cossa. Interfacing solid-state nanopores with gel media to slow dna translocations. *Electrophoresis*, 36(15):1759–1767, 2015. ISSN 0173-0835. doi: 10.1002/elps.201400488. URL https://doi.org/10.1002/elps.201400488.

[54] Allison Squires, Joseph S. Hersey, Mark W. Grinstaff, and Amit Meller. A nanopore-nanofiber mesh biosensor to control dna translocation. *Journal of the American Chemical Society*, 135(44):16304–16307, 2013. ISSN 0002-7863 1520-5126. doi: 10.1021/ja408685x. URL http://www.ncbi.nlm.nih.gov/pmc/articles/PMC4039743/ https://pubs.acs.org/doi/pdfplus/10.1021/ja408685x.

[55] Stefan W. Kowalczyk, David B. Wells, Aleksei Aksimentiev, and Cees Dekker. Slowing down dna translocation through a nanopore in lithium chloride. *Nano Letters*, 12(2):1038–1044, 2012. ISSN 1530-6984 1530-6992. doi: 10.1021/nl204273h. URL http://www.ncbi.nlm.nih.gov/pmc/articles/PMC3349906/.

[56] Jiandong Feng, Ke Liu, Roman D. Bulushev, Sergey Khlybov, Dumitru Dumcenco, Andras Kis, and Aleksandra Radenovic. Identi-

fication of single nucleotides in mos2 nanopores. *Nature Nanotechnology*, 10:1070, 2015. doi: 10.1038/nnano.2015.219https://www.nature.com/articles/nnano.2015.219#supplementary-information. URL http://dx.doi.org/10.1038/nnano.2015.219.

[57] Nicolas Di Fiori, Allison Squires, Daniel Bar, Tal Gilboa, Theodore D. Moustakas, and Amit Meller. Optoelectronic control of surface charge and translocation dynamics in solid-state nanopores. *Nature Nanotechnology*, 8:946, 2013. doi: 10.1038/nnano.2013.221.

[58] Daniel Fologea, James Uplinger, Brian Thomas, David S. McNabb, and Jiali Li. Slowing dna translocation in a solid state nanopore. *Nano letters*, 5(9):1734–1737, 2005. ISSN 1530-6984 1530-6992. doi: 10.1021/nl051063o. URL http://www.ncbi.nlm.nih.gov/pmc/articles/PMC3037730/.

[59] Joseph Larkin, Robert Henley, David C. Bell, Tzahi Cohen-Karni, Jacob K. Rosenstein, and Meni Wanunu. Slow dna transport through nanopores in hafnium oxide membranes. *ACS nano*, 7(11):10121–10128, 2013. ISSN 1936-0851 1936-086X. doi: 10.1021/nn404326f. URL http://www.ncbi.nlm.nih.gov/pmc/articles/PMC4729694/.

[60] Harold Kwok, Matthew Waugh, Josustamante, Kyle Briggs, and Vincent Tabard-Cossa. Long passage times of short ssdna molecules through metallized nanopores fabricated by controlled breakdown. *Advanced Functional Materials*, 24(48):7745–7753, 2014. ISSN 1616-3028. doi: 10.1002/adfm.201402468.

[61] Spencer Carson, James Wilson, Aleksei Aksimentiev, and Meni Wanunu. Smooth dna transport through a narrowed pore geometry. *Biophysical Journal*, 107(10):2381–2393, 2014. ISSN 0006-3495. doi: https://doi.org/10.1016/j.bpj.2014.10.017.

[62] Calin Plesa, Nick van Loo, Philip Ketterer, Hendrik Dietz, and Cees Dekker. Velocity of dna during translocation through a solid-state nanopore. *Nano Letters*, 15(1):732–737, 2015. ISSN 1530-6984. doi: 10.1021/nl504375c. URL https://doi.org/10.1021/nl504375chttps://pubs.acs.org/doi/pdfplus/10.1021/nl504375c.

[63] N. A. W. Bell and U. F. Keyser. Where now for plasmonics? *Nature Nanotechnology*, 11:1, 2016. doi: 10.1038/nnano.2015.333. URL http://dx.doi.org/10.1038/nnano.2015.333https://www.nature.com/articles/nnano.2015.333.pdf.

[64] N. A. W. Bell and U. F. Keyser. Direct measurements reveal non-Markovian fluctuations of DNA threading through a solid-state nanopore. *ArXiv e-prints*, July 2016.

[65] Sarah C. Vollmer and Hendrick W. de Haan. Translocation is a nonequilibrium process at all stages: Simulating the capture and translocation of a polymer by a nanopore. *The Journal of Chemical Physics*, 145(15):154902, 2016. ISSN 0021-9606. doi: 10.1063/1.4964630. URL https://doi.org/10.1063/1.4964630http://aip.scitation.org/doi/pdf/10.1063/1.4964630.

[66] David Sean, Hendrick W. de Haan, and Gary W. Slater. Translocation of a polymer through a nanopore starting from a confining nanotube. *ELECTROPHORESIS*, 36(5):682–691, 2015. ISSN 1522-2683. doi: 10.1002/elps.201400418.

[67] Xu Liu, Mirna Mihovilovic Skanata, and Derek Stein. Entropic cages for trapping dna near a nanopore. *Nature Communications*, 6:6222, 2015. doi: 10.1038/ncomms7222https://www.nature.com/articles/ncomms7222#supplementary-information. URL http://dx.doi.org/10.1038/ncomms7222.

[68] Martin Langecker, Daniel Pedone, Friedrich C. Simmel, and Ulrich Rant. Electrophoretic time-of-flight measurements of single dna molecules with two stacked nanopores. *Nano Letters*, 11(11):5002–5007, 2011. ISSN 1530-6984. doi: 10.1021/nl2030079. URL https://doi.org/10.1021/nl2030079.

[69] Zachary D. Harms, Klaus B. Mogensen, Pedro S. Nunes, Kaimeng Zhou, Brett W. Hildenbrand, Indranil Mitra, Zhenning Tan, Adam Zlotnick, J P. Kutter, and Stephen C. Jacobson. Nanofluidic devices with two pores in series for resistive-pulse sensing of single virus capsids. *Analytical chemistry*, 83(24):9573–9578, 2011. ISSN 0003-2700 1520-6882. doi: 10.1021/ac202358t. URL http://www.ncbi.nlm.nih.gov/pmc/articles/PMC3237903/.

[70] Daniel Pedone, Martin Langecker, Gerhard Abstreiter, and Ulrich Rant. A pore-cavity-pore device to trap and investigate single nanoparticles and dna molecules in a femtoliter compartment: Confined diffusion and narrow escape. *Nano Letters*, 11(4):1561–1567, 2011. ISSN 1530-6984. doi: 10.1021/nl104359c. URL https://doi.org/10.1021/nl104359c.

[71] Nicholas A. W. Bell, Kaikai Chen, Sandip Ghosal, Maria Ricci, and Ulrich F. Keyser. Asymmetric dynamics of dna entering and exiting a strongly confining nanopore. *Nature Communications*, 8:380, 2017. ISSN 2041-1723. doi: 10.1038/s41467-017-00423-9. URL http://www.ncbi.nlm.nih.gov/pmc/articles/PMC5577289/.

[72] Kyle Briggs, Martin Charron, Harold Kwok, Timothea Le, Sanmeet Chahal, JosBustamante, Matthew Waugh, and Vincent Tabard-Cossa. Kinetics of nanopore fabrication during controlled breakdown of dielectric membranes in solution. *Nanotechnology*, 26(8):084004, 2015. ISSN 0957-4484. URL http://stacks.iop.org/0957-4484/26/i=8/a=084004.

[73] Mirna Mihovilovic, Nicholas Hagerty, and Derek Stein. Statistics of dna capture by a solid-state nanopore. *Physical Review Letters*, 110 (2):028102, 2013. ISSN 1079-7114 (Electronic) 0031-9007 (Linking). doi: 10.1103/PhysRevLett.110.028102.

[74] Autumn T. Carlsen, Kyle Briggs, Adam R. Hall, and Vincent Tabard-Cossa. Solid-state nanopore localization by controlled breakdown of selectively thinned membranes. *Nanotechnology*, 28(8):085304, 2017. ISSN 0957-4484. URL http://stacks.iop.org/0957-4484/28/i=8/a=085304.

[75] A. J. Storm, J. H. Chen, H. W. Zandbergen, and C. Dekker. Translocation of double-strand dna through a silicon oxide nanopore. *Physical Review E*, 71(5):051903, 2005. URL https://link.aps.org/doi/10.1103/PhysRevE.71.051903.

[76] Arnold J. Storm, Cornelis Storm, Jianghua Chen, Henny Zandbergen, Jean-Frans Joanny, and Cees Dekker. Fast dna translocation through a solid-state nanopore. *Nano Letters*, 5(7):1193–1197, 2005. ISSN 1530-6984. doi: 10.1021/

nl048030d. URL https://doi.org/10.1021/nl048030dhttps://pubs.acs.org/doi/pdfplus/10.1021/nl048030d.

[77] Hendrick W. de Haan, David Sean, and Gary W. Slater. Using a péclet number for the translocation of a polymer through a nanopore to tune coarse-grained simulations to experimental conditions. *Physical Review E*, 91(2):022601, 2015. URL https://link.aps.org/doi/10.1103/PhysRevE.91.022601.

[78] T. Ikonen, A. Bhattacharya, T. Ala-Nissila, and W. Sung. Unifying model of driven polymer translocation. *Physical Review E*, 85(5):051803, 2012. URL https://link.aps.org/doi/10.1103/PhysRevE.85.051803.

[79] Iwao Teraoka. *Thermodynamics and Dynamics of Semidilute Solutions*, pages 277–332. John Wiley & Sons, Inc., 2002. ISBN 9780471224518. doi: 10.1002/0471224510.

[80] Farnoush Farahpour, Azadeh Maleknejad, Fathollah Varnik, and Mohammad Reza Ejtehadi. Chain deformation in translocation phenomena. *Soft Matter*, 9(9):2750–2759, 2013. ISSN 1744-683X. doi: 10.1039/C2SM27416G. URL http://dx.doi.org/10.1039/C2SM27416G.

[81] Payam Rowghanian and Alexander Y. Grosberg. Electrophoretic capture of a dna chain into a nanopore. *Physical Review E*, 87(4):042722, 2013. URL https://link.aps.org/doi/10.1103/PhysRevE.87.042722.

[82] Trevor J. Morin, Tyler Shropshire, Xu Liu, Kyle Briggs, Cindy Huynh, Vincent Tabard-Cossa, Hongyun Wang, and William B. Dunbar. Nanopore-based target sequence detection. *PLoS ONE*, 11(5):e0154426, 2016. ISSN 1932-6203. doi: 10.1371/journal.pone.0154426. URL http://www.ncbi.nlm.nih.gov/pmc/articles/PMC4858282/.

[83] Alon Singer, Meni Wanunu, Will Morrison, Heiko Kuhn, Maxim Frank-Kamenetskii, and Amit Meller. Nanopore-based sequence-specific detection of duplex dna for genomic profiling. *Nano letters*, 10 (2):738–742, 2010. ISSN 1530-6984 1530-6992. doi: 10.1021/

nl100058y. URL http://www.ncbi.nlm.nih.gov/pmc/articles/PMC2834191/.

[84] Evrim Atas, Alon Singer, and Amit Meller. Dna sequencing and bar-coding using solid-state nanopores. *Electrophoresis*, 33(23): 3437–3447, 2012. ISSN 0173-0835 1522-2683. doi: 10.1002/elps.201200266. URL http://www.ncbi.nlm.nih.gov/pmc/articles/PMC3773941/.

[85] Calin Plesa, Justus W. Ruitenberg, Menno J. Witteveen, and Cees Dekker. Detection of individual proteins bound along dna using solid-state nanopores. *Nano Letters*, 15(5):3153–3158, 2015. ISSN 1530-6984. doi: 10.1021/acs.nanolett.5b00249. URL https://doi.org/10.1021/acs.nanolett.5b00249.

[86] Hout Michiel van den, R. Hall Adam, Wu Meng Yue, W. Zandbergen Henny, Dekker Cees, and H. Dekker Nynke. Controlling nanopore size, shape and stability. *Nanotechnology*, 21(11):115304, 2010. ISSN 0957-4484. URL http://stacks.iop.org/0957-4484/21/i=11/a=115304.

[87] Ryan Rollings, Edward Graef, Nathan Walsh, Santoshi Nandivada, Mourad Benamara, and Jiali Li. The effects of geometry and stability of solid-state nanopores on detecting single dna molecules. *Nanotechnology*, 26(4):044001, 2015. ISSN 0957-4484. URL http://stacks.iop.org/0957-4484/26/i=4/a=044001.

[88] Arvind Balijepalli, Jessica Ettedgui, Andrew T. Cornio, Joseph W. F. Robertson, Kin P. Cheung, John J. Kasianowicz, and Canute Vaz. Quantifying short-lived events in multistate ionic current measurements. *ACS Nano*, 8(2):1547–1553, 2014. ISSN 1936-0851. doi: 10.1021/nn405761y.

[89] Jacob H. Forstater, Kyle Briggs, Joseph W. F. Robertson, Jessica Ettedgui, Olivier Marie-Rose, Canute Vaz, John J. Kasianowicz, Vincent Tabard-Cossa, and Arvind Balijepalli. Mosaic: A modular single-molecule analysis interface for decoding multistate nanopore data. *Analytical Chemistry*, 88(23):11900–11907, 2016. ISSN 0003-2700. doi: 10.1021/acs.analchem.6b03725.

URL http://dx.doi.org/10.1021/acs.analchem.6b03725http://pubs.acs.org/doi/pdfplus/10.1021/acs.analchem.6b03725.

[90] C. Raillon, P. Granjon, M. Graf, L. J. Steinbock, and A. Radenovic. Fast and automatic processing of multi-level events in nanopore translocation experiments. *Nanoscale*, 4(16):4916–4924, 2012. ISSN 2040-3364. doi: 10.1039/C2NR30951C. URL http://dx.doi.org/10.1039/C2NR30951Chttp://pubs.rsc.org/en/content/articlepdf/2012/nr/c2nr30951c.

[91] Stefan W. Kowalczyk, Alexander Y. Grosberg, Yitzhak Rabin, and Cees Dekker. Modeling the conductance and dna blockade of solid-state nanopores. *Nanotechnology*, 22(31):315101, 2011. ISSN 0957-4484. URL http://stacks.iop.org/0957-4484/22/i=31/a=315101.

[92] M. Muthukumar and H. H. Katkar. Reading nanopore clocks inngle-molecule electrophoresis experiments. *Biophysical Journal*, 108(1):17–19, 2015. ISSN 0006-3495 1542-0086. doi: 10.1016/j.bpj.2014.11.3452. URL http://www.ncbi.nlm.nih.gov/pmc/articles/PMC4286606/https://www.ncbi.nlm.nih.gov/pmc/articles/PMC4286606/pdf/main.pdf.

[93] A. Berthold, L. Nicola, P. M. Sarro, and M. J. Vellekoop. Glass-to-glass anodic bonding with standard ic technology thin films as intermediate layers. *Sensors and Actuators A: Physical*, 82(1?3):224–228, 2000. ISSN 0924-4247. doi: http://dx.doi.org/10.1016/S0924-4247(99)00376-3.

[94] K. M. Knowles and A. T. J. van Helvoort. Anodic bonding. *International Materials Reviews*, 51(5):273–311, 2006. ISSN 0950-6608. doi: 10.1179/174328006X102501. URL http://dx.doi.org/10.1179/174328006X102501.

[95] Petra Nitzsche, Klaus Lange, Bernd Schmidt, Stephan Grigull, Ulrich Kreissig, Berthold Thomas, and Karin Herzog. Ion drift processes in pyrex type alkali borosilicate glass during anodic bonding. *Journal of The Electrochemical Society*, 145(5):1755–1762, 1998. doi: 10.1149/1.1838553. URL http://jes.ecsdl.org/content/145/5/1755.abstract.

[96] S. Weichel, R. de Reus, S. Bouaidat, P. A. Rasmussen, O. Hansen, K. Birkelund, and H. Dirac. Low-temperature anodic bonding to silicon nitride. *Sensors and Actuators A: Physical*, 82(1?3): 249–253, 2000. ISSN 0924-4247. doi: http://dx.doi.org/10.1016/S0924-4247(99)00372-6.

[97] Gregory Madejski, Kilean Lucas, Flavius Pascut, Kevin Webb, and James McGrath. Tem tomography of pores with application to computational nanoscale flows in nanoporous silicon nitride (npn). *Membranes*, 8(2):26, 2018. ISSN 2077-0375. URL http://www.mdpi.com/2077-0375/8/2/26.

[98] Karl J. P. Smith, Joshua Winans, and James McGrath. Ultrathin membrane fouling mechanism transitions in dead-end filtration of protein. *ASME 2016 14th International Conference on Nanochannels, Microchannels, and Minichannels collocated with the ASME 2016 Heat Transfer Summer Conference and the ASME 2016 Fluids Engineering Division Summer Meeting*, (50343):V001T15A001, 2016. doi: 10.1115/ICNMM2016-7989. URL http://dx.doi.org/10.1115/ICNMM2016-7989http://proceedings.asmedigitalcollection.asme.org/proceeding.aspx?articleid=2583342.

[99] Lisa M. Viculis, Julia J. Mack, and Richard B. Kaner. A chemical route to carbon nanoscrolls. *Science*, 299(5611):1361, 2003. URL http://science.sciencemag.org/content/299/5611/1361.abstracthttp://science.sciencemag.org/content/sci/299/5611/1361.full.pdf.

[100] Vladan Lucic, Friedrich Fter, and Wolfgang Baumeister. Structural studies by electron tomography: From cells to molecules. *Annual Review of Biochemistry*, 74(1):833–865, 2005. ISSN 0066-4154. doi: 10.1146/annurev.biochem.73.011303.074112. URL https://doi.org/10.1146/annurev.biochem.73.011303.074112https://www.annualreviews.org/doi/pdf/10.1146/annurev.biochem.73.011303.074112.

[101] Pawel A. Penczek and Joachim Frank. *Resolution in Electron Tomography*, pages 307–330. Springer New York,

New York, NY, 2006. ISBN 978-0-387-69008-7. doi: 10.1007/978-0-387-69008-7_11. URL https://doi.org/10.1007/978-0-387-69008-7_11https://link.springer.com/content/pdf/10.1007%2F978-0-387-69008-7_11.pdf.

[102] Hanying Li, Huolin L. Xin, David A. Muller, and Lara A. Estroff. Visualizing the 3d internal structure of calcite single crystals grown in agarose hydrogels. *Science*, 326(5957):1244–1247, 2009. doi: 10.1126/science.1178583. URL http://science.sciencemag.org/content/sci/326/5957/1244.full.pdfhttp://science.sciencemag.org/content/326/5957/1244.long.

[103] Chien-Chun Chen, Chun Zhu, Edward R. White, Chin-Yi Chiu, M. C. Scott, B. C. Regan, Laurence D. Marks, Yu Huang, and Jianwei Miao. Three-dimensional imaging of dislocations in a nanoparticle at atomic resolution. *Nature*, 496:74, 2013. doi: 10.1038/nature12009https://www.nature.com/articles/nature12009#supplementary-information. URL http://dx.doi.org/10.1038/nature12009.

[104] Peter Ercius, Osama Alaidi, J. Rames Matthew, and Gang Ren. Electron tomography: A three dimensional analytic tool for hard and soft materials research. *Advanced Materials*, 27(38):5638–5663, 2015. ISSN 0935-9648. doi: 10.1002/adma.201501015. URL https://doi.org/10.1002/adma.201501015https://onlinelibrary.wiley.com/doi/pdf/10.1002/adma.201501015.

[105] Michael Niehle and Achim Trampert. Electron tomography on nanopores embedded in epitaxial gasb thin films. *Micron*, 73:54–62, 2015. ISSN 0968-4328. doi: https://doi.org/10.1016/j.micron.2015.03.010.

[106] Takuya Echigo, Niven Monsegue, Deborah M. Aruguete, Mitsuhiro Murayama, and Michael F. Hochella Jr. Nanopores in hematite (α-fe$_2$o$_3$) nanocrystals observed by electron tomography. *American Mineralogist*, 98(1):154–162, 2013. ISSN 0003-004X. doi: 10.2138/am.2013.4120. URL http://dx.doi.org/10.2138/am.2013.4120https://pubs.geoscienceworld.org/msa/ammin/article-abstract/98/1/154/

45718/nanopores-in-hematite-fe2o3-nanocrystals-observed?redirectedFrom=fulltext.

[107] H. W. Liu, R. Nishitani, T. Fujita, W. Li, L. Zhang, X. Y. Lang, P. Richard, K. S. Nakayama, X. Chen, M. W. Chen, and Q. K. Xue. Inelastic electron-tunneling spectroscopy of nanoporous gold films. *Physical Review B*, 89(3):035426, 2014. doi: 10.1103/PhysRevB.89.035426. URL https://link.aps.org/doi/10.1103/PhysRevB.89.035426.

[108] Min Jun Kim, Ben McNally, Kazuyoshi Murata, and Amit Meller. Characteristics of solid-state nanometre pores fabricated using a transmission electron microscope. *Nanotechnology*, 18(20):205302, 2007. ISSN 0957-4484. URL http://stacks.iop.org/0957-4484/18/i=20/a=205302.

[109] Hitomi Mukaibo, Tonghui Wang, Victor Pz-Gonzz, Jirachai Getpreecharsawas, Jack T Wurzer, Blanca Lapizco-Encinas, and James McGrath. Ultrathin nanoporous membranes for insulator-based dielectrophoresis (idep). *Nanotechnology*, 2018. doi: 10.1088/1361-6528/aab5f7. URL http://iopscience.iop.org/article/10.1088/1361-6528/aab5f7/pdf.

[110] Cic Messaoudi, Thomas Boudier, Carlos Oscar Sanchez Sorzano, and Sergio Marco. Tomoj: tomography software for three-dimensional reconstruction in transmission electron microscopy. *BMC Bioinformatics*, 8(1):288, 2007. ISSN 1471-2105. doi: 10.1186/1471-2105-8-288. URL https://doi.org/10.1186/1471-2105-8-288.

[111] James R. Kremer, David N. Mastronarde, and J. Richard McIntosh. Computer visualization of three-dimensional image data using imod. *Journal of Structural Biology*, 116(1):71–76, 1996. ISSN 1047-8477. doi: https://doi.org/10.1006/jsbi.1996.0013. URL http://www.sciencedirect.com/science/article/pii/S1047847796900131https://www.sciencedirect.com/science/article/pii/S1047847796900131?via%3Dihub.

[112] Karl J. P. Smith, Marina May, Ruth Baltus, and James L. McGrath. A predictive model of separations in dead-end

filtration with ultrathin membranes. *Separation and Purification Technology*, 189:40–47, 2017. ISSN 1383-5866. doi: https://doi.org/10.1016/j.seppur.2017.07.032. URL http://www.sciencedirect.com/science/article/pii/S1383586617304380https://www.sciencedirect.com/science/article/pii/S1383586617304380?via%3Dihub.

[113] Johannes Schindelin, Ignacio Arganda-Carreras, Erwin Frise, Verena Kaynig, Mark Longair, Tobias Pietzsch, Stephan Preibisch, Curtis Rueden, Stephan Saalfeld, Benjamin Schmid, Jean-Yves Tinevez, Daniel James White, Volker Hartenstein, Kevin Eliceiri, Pavel Tomancak, and Albert Cardona. Fiji: an open-source platform for biological-image analysis. *Nature Methods*, 9:676, 2012. doi: 10.1038/nmeth.2019https://www.nature.com/articles/nmeth.2019#supplementary-information. URL http://dx.doi.org/10.1038/nmeth.2019https://www.nature.com/articles/nmeth.2019.pdf.

[114] C. A. Schneider, W. S. Rasband, and K. W. Eliceiri. Nih image to imagej: 25 years of image analysis. *Nat Methods*, 9(7):671–5, 2012. ISSN 1548-7105 (Electronic) 1548-7091 (Linking). doi: 10.1038/nmeth.2089. URL https://www.ncbi.nlm.nih.gov/pubmed/22930834.

[115] Carlos Oscar Sanchez Sorzano, Cic Messaoudi, Matthias Eibauer, J. R. Bilbao-Castro, R. Hegerl, S. Nickell, S. Marco, and J. M. Carazo. Marker-free image registration of electron tomography tilt-series. *BMC Bioinformatics*, 10(1):124, 2009. ISSN 1471-2105. doi: 10.1186/1471-2105-10-124. URL https://doi.org/10.1186/1471-2105-10-124https://bmcbioinformatics.biomedcentral.com/track/pdf/10.1186/1471-2105-10-124.

[116] Peter Gilbert. Iterative methods for the three-dimensional reconstruction of an object from projections. *Journal of Theoretical Biology*, 36(1):105–117, 1972. ISSN 0022-5193. doi: https://doi.org/10.1016/0022-5193(72)90180-4. URL http://www.sciencedirect.com/science/article/pii/

0022519372901804https://www.sciencedirect.com/science/article/pii/0022519372901804?via%3Dihub.

[117] Scientific Computing and Imaging Institute, 2018. URL http://www.seg3d.org.

[118] Paolo Cignoni, Marco Callieri, Massimiliano Corsini, Matteo Dellepiane, Fabio Ganovelli, and Guido Ranzuglia. *MeshLab: an Open-Source Mesh Processing Tool*, pages 129–136. The Eurographics Association, 2008. ISBN 978-3-905673-68-5. doi: 10.2312/LocalChapterEvents/ItalChap/ItalianChapConf2008/129-136.

[119] Armin Delavari and Ruth Baltus. The effect of the pore entrance on particle motion in slit pores: Implications for ultrathin membranes. *Membranes*, 7(3):42, 2017. ISSN 2077-0375. doi: 10.3390/membranes7030042. URL http://www.ncbi.nlm.nih.gov/pmc/articles/PMC5618127/http://www.mdpi.com/2077-0375/7/3/42/pdf.

[120] Handol Lee, Doris Segets, Sebastian S Wolfgang Peukert, Sheng-Chieh Chen, and David Y. H. Pui. Liquid filtration of nanoparticles through track-etched membrane filters under unfavorable and different ionic strength conditions: Experiments and modeling. *Journal of Membrane Science*, 524:682–690, 2017. ISSN 0376-7388. doi: https://doi.org/10.1016/j.memsci.2016.11.023. URL http://www.sciencedirect.com/science/article/pii/S0376738816312352https://www.sciencedirect.com/science/article/pii/S0376738816312352?via%3Dihub.

[121] Dmitriy V. Melnikov, Zachery K. Hulings, and Maria E. Gracheva. Electro-osmotic flow through nanopores in thin and ultrathin membranes. *Physical Review E*, 95(6):063105, 2017. URL https://link.aps.org/doi/10.1103/PhysRevE.95.063105.

[122] A. Klug R. A. Crowther, D. J. DeRosier. The reconstruction of a three-dimensional structure from projections and its application to electron microscopy. *Proceedings of the Royal Society of London. A. Mathematical and Physical Sciences*, 317 (1530):319–340, 1970. doi: 10.1098/rspa.1970.0119. URL

http://rspa.royalsocietypublishing.org/content/royprsa/317/1530/319.full.pdf.

[123] Bruce F. McEwen and Michael Marko. *Chapter 5 Three-Dimensional Transmission Electron Microscopy and Its Application to Mitosis Research*, volume 61, pages 81–111. Academic Press, 1998. ISBN 0091-679X. doi: https://doi.org/10.1016/S0091-679X(08)61976-7.

[124] B. Kann, H. L. Offerhaus, M. Windbergs, and C. Otto. Raman microscopy for cellular investigations–from single cell imaging to drug carrier uptake visualization. *Adv Drug Deliv Rev*, 89(0):71–90, 2015. ISSN 1872-8294 (Electronic) 0169-409X (Linking). doi: 10.1016/j.addr.2015.02.006. URL https://www.ncbi.nlm.nih.gov/pubmed/25728764.

[125] Christian Matth, Amit Kale, Tatyana Chernenko, Vladimir Torchilin, and Max Diem. New ways of imaging uptake and intracellular fate of liposomal drug carrier systems inside individual cells, based on raman microscopy. *Molecular Pharmaceutics*, 5(2):287–293, 2008. ISSN 1543-8384. doi: 10.1021/mp7001158. URL http://dx.doi.org/10.1021/mp7001158.

[126] Hiroyuki Yamakoshi, Kosuke Dodo, Masaya Okada, Jun Ando, Almar Palonpon, Katsumasa Fujita, Satoshi Kawata, and Mikiko Sodeoka. Imaging of edu, an alkyne-tagged cell proliferation probe, by raman microscopy. *Journal of the American Chemical Society*, 133(16):6102–6105, 2011. ISSN 0002-7863. doi: 10.1021/ja108404p. URL http://dx.doi.org/10.1021/ja108404p.

[127] Adrian Ghita, Flavius C. Pascut, Virginie Sottile, Chris Denning, and Ioan Notingher. Applications of raman micro-spectroscopy to stem cell technology: label-free molecular discrimination and monitoring cell differentiation. *EPJ Techniques and Instrumentation*, 2(1):6, 2015. ISSN 2195-7045. doi: 10.1140/epjti/s40485-015-0016-8. URL https://doi.org/10.1140/epjti/s40485-015-0016-8https://www.ncbi.nlm.nih.gov/pmc/articles/PMC4486413/pdf/40485_2015_Article_16.pdf.

[128] Peter Hermann, Heinz Fabian, Dieter Naumann, and Antje Hermelink. Comparative study of far-field and near-field raman spec-

tra from silicon-based samples and biological nanostructures. *The Journal of Physical Chemistry C*, 115(50):24512–24520, 2011. ISSN 1932-7447. doi: 10.1021/jp206659z. URL http://dx.doi.org/10.1021/jp206659z.

[129] Bruce A. Pfeffer and Nancy J. Philp. Cell culture of retinal pigment epithelium: Special issue. *Experimental Eye Research*, 126(0):1–4, 2014. ISSN 0014-4835. doi: http://dx.doi.org/10.1016/j.exer.2014.07.010. URL http://www.sciencedirect.com/science/article/pii/S0014483514001924.

[130] K. C. Dunn, A. E. Aotaki-Keen, F. R. Putkey, and L. M. Hjelmeland. Arpe-19, a human retinal pigment epithelial cell line with differentiated properties. *Experimental Eye Research*, 62(2):155–170, 1996. ISSN 0014-4835. doi: http://dx.doi.org/10.1006/exer.1996.0020. URL http://www.sciencedirect.com/science/article/pii/S0014483596900202.

[131] Lucia V. Mercaldo, Emilia M. Esposito, Paola Delli Veneri, Giuseppe Fameli, Salvo Mirabella, and Giuseppe Nicotra. First and second-order raman scattering in si nanostructures within silicon nitride. *Applied Physics Letters*, 97(15):153112, 2010. doi: doi:http://dx.doi.org/10.1063/1.3501133. URL http://scitation.aip.org/content/aip/journal/apl/97/15/10.1063/1.3501133.

[132] Imran I. Patel and Francis L. Martin. Discrimination of zone-specific spectral signatures in normal human prostate using raman spectroscopy. *Analyst*, 135(12):3060–3069, 2010. ISSN 0003-2654. doi: 10.1039/C0AN00518E. URL http://dx.doi.org/10.1039/C0AN00518E.

[133] Laura T. Kerr, Hugh J. Byrne, and Bryan M. Hennelly. Optimal choice of sample substrate and laser wavelength for raman spectroscopic analysis of biological specimen. *Analytical Methods*, 7(12):5041–5052, 2015. ISSN 1759-9660. doi: 10.1039/C5AY00327J. URL http://dx.doi.org/10.1039/C5AY00327J.

[134] J. D. Zahn, K. J. Gabriel, and G. K. Fedder. A direct plasma etch approach to high aspect ratio polymer micromachining with applications in biomems and cmos-mems. In *Micro Electro Mechanical Systems,*

2002. The Fifteenth IEEE International Conference on, pages 137–140, 2002. ISBN 1084-6999. doi: 10.1109/MEMSYS.2002.984223.

[135] J. Miller Joshua, N. Carter Robert, B. McNabb Kelly, S. Des-Ormeaux Jon-Paul, C. Striemer Christopher, D. Winans Joshua, and R. Gaborski Thomas. Lift-off of large-scale ultrathin nanomembranes. *Journal of Micromechanics and Microengineering*, 25(1): 015011, 2015. ISSN 0960-1317. URL http://stacks.iop.org/0960-1317/25/i=1/a=015011.

[136] E. H. Hirsch. Stress in porous thin films through absorption of polar molecules (and relevance to optical coatings). *Journal of Physics D: Applied Physics*, 13(11):2081, 1980. ISSN 0022-3727. URL http://stacks.iop.org/0022-3727/13/i=11/a=018.

[137] Lara Pasovic, Tor Paaske Utheim, Rima Maria, Torstein Lyberg, Edward B. Messelt, Peder Aabel, Dong Feng Chen, Xiangjun Chen, and Jon Roger Eidet. Optimization of storage temperature for cultured arpe-19 cells. *Journal of Ophthalmology*, 2013:11, 2013. doi: 10.1155/2013/216359. URL http://dx.doi.org/10.1155/2013/216359http://downloads.hindawi.com/journals/joph/2013/216359.pdf.

[138] Tadanobu Yoshikawa, Nahoko Ogata, Hiroshi Izuta, Masamitsu Shimazawa, Hideaki Hara, and Kanji Takahashi. Increased expression of tight junctions in arpe-19 cells under endoplasmic reticulum stress. *Current Eye Research*, 36(12):1153–1163, 2011. ISSN 0271-3683. doi: 10.3109/02713683.2011.606592. URL https://doi.org/10.3109/02713683.2011.606592https://www.tandfonline.com/doi/pdf/10.3109/02713683.2011.606592?needAccess=true.

[139] Alexandra Falamas, S. Kalra, Vasile Chis, and I. Notingher. *Monitoring the RNA Distribution in Human Embryonic Stem Cells using Raman Micro-Spectroscopy and Fluorescence Imaging*, volume 1565. 2013. doi: 10.1063/1.4833693. URL https://aip.scitation.org/doi/abs/10.1063/1.4833693.

Vincenzo Amendola, Roberto Pilot, Marco Frasconi, Onofrio M. Maragand Maria Antonia Iat Surface plasmon resonance in gold

nanoparticles: a review. *Journal of Physics: Condensed Matter*, 29(20):203002, 2017. ISSN 0953-8984. URL http://stacks.iop.org/0953-8984/29/i=20/a=203002.

[140] M. Fleischmann, P. J. Hendra, and A. J. McQuillan. Raman spectra of pyridine adsorbed at a silver electrode. *Chemical Physics Letters*, 26(2):163–166, 1974. ISSN 0009-2614. doi: https://doi.org/10.1016/0009-2614(74)85388-1. URL http://www.sciencedirect.com/science/article/pii/0009261474853881.

[141] Haynes Christy L., Yonzon Chanda Ranjit, Zhang Xiaoyu, and Van Duyne Richard P. Surface?enhanced raman sensors: early history and the development of sensors for quantitative biowarfare agent and glucose detection. *Journal of Raman Spectroscopy*, 36(6?7):471–484, 2005. doi: doi:10.1002/jrs.1376. URL https://onlinelibrary.wiley.com/doi/abs/10.1002/jrs.1376https://onlinelibrary.wiley.com/doi/pdf/10.1002/jrs.1376.

[142] David L. Jeanmaire and Richard P. Van Duyne. Surface raman spectroelectrochemistry: Part i. heterocyclic, aromatic, and aliphatic amines adsorbed on the anodized silver electrode. *Journal of Electroanalytical Chemistry and Interfacial Electrochemistry*, 84(1):1–20, 1977. ISSN 0022-0728. doi: https://doi.org/10.1016/S0022-0728(77)80224-6. URL http://www.sciencedirect.com/science/article/pii/S0022072877802246.

[143] M. Grant Albrecht and J. Alan Creighton. Anomalously intense raman spectra of pyridine at a silver electrode. *Journal of the American Chemical Society*, 99(15):5215–5217, 1977. ISSN 0002-7863. doi: 10.1021/ja00457a071. URL https://doi.org/10.1021/ja00457a071https://pubs.acs.org/doi/pdfplus/10.1021/ja00457a071.

[144] Pablo G. Etchegoin and Eric C. Le Ru. *Basic Electromagnetic Theory of SERS*, book section 1, pages 1–37. Wiley-Blackwell, 2010. ISBN 9783527632756. doi: doi:10.1002/9783527632756.ch1. URL https://onlinelibrary.wiley.com/doi/abs/10.1002/9783527632756.ch1.

[145] Xiaofeng Fan, Weitao Zheng, and David J. Singh. Light scattering and surface plasmons on small spherical particles. *Light: Science & Applications*, 3:e179, 2014. doi: 10.1038/lsa.2014.60. URL http://dx.doi.org/10.1038/lsa.2014.60.

[146] Anatoly V. Zayats, Igor I. Smolyaninov, and Alexei A. Maradudin. Nano-optics of surface plasmon polaritons. *Physics Reports*, 408 (3):131–314, 2005. ISSN 0370-1573. doi: https://doi.org/10.1016/j.physrep.2004.11.001.

[147] S. Schlucker. Surface-enhanced raman spectroscopy: concepts and chemical applications. *Angew Chem Int Ed Engl*, 53(19):4756–95, 2014. ISSN 1521-3773 (Electronic) 1433-7851 (Linking). doi: 10.1002/anie.201205748.

[148] Xinxin Yu, Hongbing Cai, Wenhua Zhang, Xinjing Li, Nan Pan, Yi Luo, Xiaoping Wang, and J. G. Hou. Tuning chemical enhancement of sers by controlling the chemical reduction of graphene oxide nanosheets. *ACS Nano*, 5(2):952–958, 2011. ISSN 1936-0851. doi: 10.1021/nn102291j. URL https://doi.org/10.1021/nn102291jhttps://pubs.acs.org/doi/pdfplus/10.1021/nn102291j.

[149] Andreas Otto. The ”chemical” (electronic) contribution to surface-enhanced raman scattering. *Journal of Raman Spectroscopy*, 36 (6-7):497–509, 2005. ISSN 1097-4555. doi: 10.1002/jrs.1355.

[150] Shavini Wijesuriya, Krishna Burugapalli, Ruth Mackay, Godwin Ajaezi, and Wamadeva Balachandran. Chemically roughened solid silver: A simple, robust and broadband sers substrate. *Sensors*, 16(10):1742, 2016. ISSN 1424-8220. URL http://www.mdpi.com/1424-8220/16/10/1742.

[151] Guang Yang, Jagjit Nanda, Boya Wang, Gang Chen, and Daniel T. Hallinan. Self-assembly of large gold nanoparticles for surface-enhanced raman spectroscopy. *ACS Applied Materials & Interfaces*, 9(15):13457–13470, 2017. ISSN 1944-8244. doi: 10.1021/acsami.7b01121. URL https://doi.org/10.1021/acsami.7b01121https://pubs.acs.org/doi/pdfplus/10.1021/acsami.7b01121.

[152] Min Hu, Jingyi Chen, Zhi-Yuan Li, Leslie Au, Gregory V. Hartland, Xingde Li, Manuel Marquez, and Younan Xia. Gold nanostructures: engineering their plasmonic properties for biomedical applications. *Chemical Society Reviews*, 35(11):1084–1094, 2006. ISSN 0306-0012. doi: 10.1039/B517615H. URL http://dx.doi.org/10.1039/B517615Hhttp://pubs.rsc.org/en/content/articlepdf/2006/cs/b517615h.

[153] Jaena Park, Miyeon Hwang, ByeongHyeon Choi, Hyesun Jeong, Jik-han Jung, Hyun Koo Kim, Sunghoi Hong, Ji-ho Park, and Yeonho Choi. Exosome classification by pattern analysis of surface-enhanced raman spectroscopy data for lung cancer diagnosis. *Analytical Chemistry*, 89(12):6695–6701, 2017. ISSN 0003-2700. doi: 10.1021/acs.analchem.7b00911. URL https://doi.org/10.1021/acs.analchem.7b00911https://pubs.acs.org/doi/pdfplus/10.1021/acs.analchem.7b00911.

[154] Lei Chen, Huiying Yan, Xiangxin Xue, Dayu Jiang, Yuxi Cai, Dongmei Liang, Young Mee Jung, Xiao Xia Han, and Bing Zhao. Surface-enhanced raman scattering (sers) active gold nanoparticles decorated on a porous polymer filter. *Applied Spectroscopy*, 71(7):1543–1550, 2017. URL http://as.osa.org/abstract.cfm?URI=as-71-7-1543http://journals.sagepub.com/doi/pdf/10.1177/0003702817703293.

[155] Juan C. Fraire, Luis A. Pz, and Eduardo A. Coronado. Cluster size effects in the surface-enhanced raman scattering response of ag and au nanoparticle aggregates: Experimental and theoretical insight. *The Journal of Physical Chemistry C*, 117 (44):23090–23107, 2013. ISSN 1932-7447. doi: 10.1021/jp3123709. URL https://doi.org/10.1021/jp3123709https://pubs.acs.org/doi/pdfplus/10.1021/jp3123709.

[156] Fung Suong Ou, Min Hu, Ivan Naumov, Ansoon Kim, Wei Wu, Alexander M. Bratkovsky, Xuema Li, R. Stanley Williams, and Zhiyong Li. Hot-spot engineering in polygonal nanofinger assemblies for surface enhanced raman spectroscopy. *Nano Letters*, 11(6):2538–2542, 2011. ISSN 1530-6984. doi: 10.1021/

nl201212n. URL https://doi.org/10.1021/nl201212nhttps://pubs.acs.org/doi/pdfplus/10.1021/nl201212n.

[157] Kristin L. Wustholz, Anne-Isabelle Henry, Jeffrey M. McMahon, R. Griffith Freeman, Nicholas Valley, Marcelo E. Piotti, Michael J. Natan, George C. Schatz, and Richard P. Van Duyne. Structure?activity relationships in gold nanoparticle dimers and trimers for surface-enhanced raman spectroscopy. *Journal of the American Chemical Society*, 132(31):10903–10910, 2010. ISSN 0002-7863. doi: 10.1021/ja104174m. URL https://doi.org/10.1021/ja104174m.

[158] Xiaohua Huang and Mostafa A. El-Sayed. Gold nanoparticles: Optical properties and implementations in cancer diagnosis and photothermal therapy. *Journal of Advanced Research*, 1(1):13–28, 2010. ISSN 20901232. doi: 10.1016/j.jare.2010.02.002.

[159] Yue Weisheng, Wang Zhihong, Yang Yang, Chen Longqing, Syed Ahad, Wong Kimchong, and Wang Xianbin. Electron-beam lithography of gold nanostructures for surface-enhanced raman scattering. *Journal of Micromechanics and Microengineering*, 22(12):125007, 2012. ISSN 0960-1317. URL http://stacks.iop.org/0960-1317/22/i=12/a=125007.

[160] A. R. M. Radzol, Khuan Y. Lee, W. Mansor, and S. R. Yahaya. Nano-scale characterization of surface enhanced raman spectroscopic substrates. *Procedia Engineering*, 41:867–873, 2012. ISSN 1877-7058. doi: https://doi.org/10.1016/j.proeng.2012.07.256.

[161] Troy A. Alexander. Applications of surface-enhanced raman spectroscopy (sers) for biosensing: an analysis of reproducible commercially available substrates. In *Optics East 2005*, volume 6007, page 8. SPIE, 2005.

[162] Long Liu, Qian Zhang, Yuanshen Lu, Wei Du, Bin Li, Yushuang Cui, Changsheng Yuan, Peng Zhan, Haixiong Ge, Zhenling Wang, and Yanfeng Chen. A high-performance and low cost sers substrate of plasmonic nanopillars on plastic film fabricated by nanoimprint lithography with aao template. *AIP Advances*, 7(6):065205, 2017. doi: 10.1063/1.4985270. URL

https://aip.scitation.org/doi/abs/10.1063/1.4985270https://aip.scitation.org/doi/pdf/10.1063/1.4985270.

[163] Pamela A. Mosier-Boss. Review of sers substrates for chemical sensing. *Nanomaterials*, 7(6):142, 2017. ISSN 2079-4991. doi: 10.3390/nano7060142. URL http://www.ncbi.nlm.nih.gov/pmc/articles/PMC5485789/http://www.mdpi.com/2079-4991/7/6/142/pdf.

[164] Katrin Kneipp, Yang Wang, Harald Kneipp, Lev T. Perelman, Irving Itzkan, Ramachandra R. Dasari, and Michael S. Feld. Single molecule detection using surface-enhanced raman scattering (sers). *Physical Review Letters*, 78(9):1667–1670, 1997. URL https://link.aps.org/doi/10.1103/PhysRevLett.78.1667.

[165] Loan Le Thi Ngoc, Tao Yuan, Naoto Oonishi, Jan van Nieuwkasteele, Albert van den Berg, Hjalmar Permentier, Rainer Bischoff, and Edwin T. Carlen. Suppression of surface-enhanced raman scattering on gold nanostructures by metal adhesion layers. *The Journal of Physical Chemistry C*, 120(33):18756–18762, 2016. ISSN 1932-7447. doi: 10.1021/acs.jpcc.6b05375. URL https://doi.org/10.1021/acs.jpcc.6b05375https://pubs.acs.org/doi/pdfplus/10.1021/acs.jpcc.6b05375.

[166] Sujin Seo, Te-Wei Chang, and Gang Logan Liu. 3d plasmon coupling assisted sers on nanoparticle-nanocup array hybrids. *Scientific Reports*, 8(1):3002, 2018. ISSN 2045-2322. doi: 10.1038/s41598-018-19256-7. URL https://doi.org/10.1038/s41598-018-19256-7.

[167] Dmitry Kurouski, Nicolas Large, Naihao Chiang, Nathan Greeneltch, Keith T. Carron, Tamar Seideman, George C. Schatz, and Richard P. Van Duyne. Unraveling near-field and far-field relationships for 3d sers substrates - a combined experimental and theoretical analysis. *Analyst*, 141(5):1779–1788, 2016. ISSN 0003-2654. doi: 10.1039/C5AN01921D. URL http://dx.doi.org/10.1039/C5AN01921Dhttp://pubs.rsc.org/en/content/articlepdf/2016/an/c5an01921d.

[168] Flavius Cristian Pascut, Kevin Francis Webb, Gregory Madejski, and James McGrath. Nanostructured materials, October 1 2015. URL https://patentscope.wipo.int/search/en/detail.jsf?-docId=WO2017055863. PTC Application No. 62/235,929, Filed 08/01/15. US Patent Publication Number: WO / 2017/055863.

[169] Yuan Ni, Caixia Kan, Juan Xu, Yang Liu, Haiying Xu, and Changshun Wang. Dependence of plasmon coupling on curved interfaces. *Applied Optics*, 56(29):8240–8245, 2017. doi: 10.1364/AO.56.008240.

[170] Changwon Lee, Christopher S. Robertson, An H. Nguyen, Mehmet Kahraman, and Sebastian Wachsmann-Hogiu. Thickness of a metallic film, in addition to its roughness, plays a significant role in sers activity. *Scientific Reports*, 5:11644, 2015. doi: 10.1038/srep11644https://www.nature.com/articles/srep11644#supplementary-information. URL http://dx.doi.org/10.1038/srep11644.

[171] Daniel R. Ward, Nathaniel K. Grady, Carly S. Levin, Naomi J. Halas, Yanpeng Wu, Peter Nordlander, and Douglas Natelson. Electromigrated nanoscale gaps for surface-enhanced raman spectroscopy. *Nano Letters*, 7(5):1396–1400, 2007. ISSN 1530-6984. doi: 10.1021/nl070625w. URL https://doi.org/10.1021/nl070625whttps://pubs.acs.org/doi/pdfplus/10.1021/nl070625w.

[172] M. Adamov, B. Perovi, and T. Nenadovi. Electrical and structural properties of thin gold films obtained by vacuum evaporation and sputtering. *Thin Solid Films*, 24(1):89–100, 1974. ISSN 0040-6090. doi: https://doi.org/10.1016/0040-6090(74)90254-5. URL http://www.sciencedirect.com/science/article/pii/0040609074902545.

[173] J. A. Venables, G. D. T. Spiller, and M. Hanbucken. Nucleation and growth of thin films. *Reports on Progress in Physics*, 47(4):399, 1984. ISSN 0034-4885. URL http://stacks.iop.org/0034-4885/47/i=4/a=002.